



SAPIENZA
UNIVERSITÀ DI ROMA

Tesi di Dottorato

**ULTRA-HIGH Q-FACTOR
SILICON RESONATOR FOR
HIGH FREQUENCY OSCILLATORS**

ENRICO LIA

Dottorato di Ricerca in Elettromagnetismo
XXX Ciclo: Novembre 2014 - Ottobre 2017

Dipartimento di Ingegneria Dell'Informazione
Elettronica e Telecomunicazione (DIET)

Università degli Studi di Roma "La Sapienza"

Coordinatore del Corso
Prof. Daniele Andreucci
Prof. Angela Pistoia
Prof. Paola Loreti

Docente Guida
Prof. Fabrizio Frezza

TABLE OF CONTENTS

1. ACKNOWLEDGEMENTS	3
2. ABSTRACT	4
3. INTRODUCTION	5
3.1. OBJECTIVES	5
3.2. MOTIVATION.....	6
4. RESONATOR DESIGN	10
4.1. ELECTROMAGNETIC BAND-GAP STRUCTURE THEORY	10
4.2. HIGH RESISTIVITY SILICON MATERIAL.....	16
4.3. HIGH Q-FACTOR RESONATOR DESIGN.....	18
4.4. FULL (3D) ELECTROMAGNETIC SIMULATION AND OPTIMIZATION.....	27
4.5. PROTOTYPE FABRICATION AND MEASUREMENTS	41
4.6. INTRODUCTION OF ETCHING EFFECTS	44
4.7. CORRELATION OF RESULTS (MEASUREMENT VERSUS SIMULATION)	44
5. OSCILLATOR CIRCUIT DESIGN	55
5.1. OSCILLATOR THEORY	55
5.2. OSCILLATOR CONFIGURATIONS	66
5.3. PROCESS DESIGN KIT (MMIC).....	68
5.4. TRANSISTOR NOISE MODELLING	71
5.5. CIRCUIT SIMULATION AND OPTIMIZATION	74
5.6. LAYOUT (MMIC) AND ELECTROMAGNETIC ANALYSIS.....	91
5.7. WAVEGUIDE PROBE AND BAND-PASS FILTER	92
6. OSCILLATOR PERFORMANCE	99
6.1. INTRODUCTION.....	99
6.2. PHASE NOISE PERFORMANCE.....	100
6.3. OUTPUT POWER PERFORMANCE	101
6.4. SPURIOUS PERFORMANCE	102
7. CONCLUSIONS	103
7.1. ACHIEVED RESULTS	103
7.2. FUTURE DEVELOPMENTS	105
8. ABBREVIATIONS	107
9. REFERENCES	112

1. ACKNOWLEDGEMENTS

Firstly, I would like to express my sincere gratitude to my advisor Prof. Fabrizio Frezza for the continuous support of my Ph.D. study and related research.

Besides my advisor, I would like to thank the European Space Agency (ESA/ESTEC) for providing me support with regards to the simulation tools and fabrication of the prototype.

I also would like to thank the colleagues Dr. Rüdiger Follmann, Ulrich Lewark, O. Kersten and Dr. Mirna F. de Oliveira for their insightful comments and encouragements, also for the hard question which helped me to widen my research from various perspectives.

Last but not the least, I would like to thank my family: my mother, sister and wife as well my brethren for supporting me spiritually throughout writing this thesis and my life in general.

2. ABSTRACT

The thesis is divided into five main chapters as follows.

The first and introductory chapter review the objectives and motivations which led the work performed in the thesis. It highlights the use of electromagnetic band-gap structures in high frequency oscillators operating directly in fundamental mode with great benefits in obtaining ultra-high Q-factor and therefore low phase noise. Additionally, it underlines the importance and benefits of the novel oscillator concept compared to limitations of conventional quartz oscillators as well the motivation behind the reviewed scenarios and respective choice of the operating frequency.

The second chapter describes the resonator theory using a theoretical approach to explain the mechanisms of photonic and electronic band-gap structures; the design approach; simulation and optimisation of the proposed electronic band-gap resonator; the fabrication process and finally the correlation obtained between the simulated and measured results.

The third chapter covers the oscillator theory and the proposed configurations, the process design kit employed for the simulation of monolithic microwave integrated circuits; the noise modelling that affects the phase noise as well the oscillator design and optimization through a circuit simulator. The chapter also covers the layout and respective electromagnetic analysis of the oscillator circuits used in the next chapter to determine the real performance of the oscillators operating in the millimetre-wave band. The mechanical structures comprehending part of the oscillator network in the waveguide domain such as waveguide filters, E-probes, transmission lines and transitions are assessed, quantifying the losses and performance in the oscillator loop.

The fourth chapter of the thesis summarises the oscillator performance starting with an introduction, phase noise and output power performance as well spurious. This chapter is dedicated to the obtained results within the whole experiment of oscillators based on electronic band-gap resonators using the 0.13 μm Silicon-Germanium semiconductor process.

Finally, the fifth chapter concludes the challenges, findings, limitations and achieved results within this work. A benchmark analysis reporting the state-of-art oscillators and the one developed within this work is presented. A number of aspects for future developments and improvements are suggested, thus concluding the thesis.

3. INTRODUCTION

3.1. OBJECTIVES

Electromagnetic band-gap (EBG) structures possessing high quality (Q) factor represent an important technology for the realisation of several components for future communication systems operating in the millimetre-wave and terahertz regions of the electromagnetic spectrum. More specifically two-dimension (2D) electromagnetic band-gap structures with a planar form factor are investigated.

The thesis focuses on the investigation and characterisation of ultra-high Q-factor low loss Silicon resonators with transverse electric (TE)-like electromagnetic band-gap determined by two-dimensional periodic structure made of a Silicon slab having a triangular lattice of air cylinders. A band-gap is observed where no energy is propagated through the slab, however engineering defects are created and optimised within the lattice producing resonant cavities and waveguides. The structure being excited with the fundamental TE_{10} mode can be coupled to external circuits via waveguides and its respective transitions in co-planar waveguide transmission line used to convey the millimetre-wave frequency signals.

The ultimate goal is to investigate and characterise the promising low loss and high frequency Silicon resonators suitable for millimetre-wave communications such as used in low phase noise oscillator application and band pass filters.

Oscillators play a very important role in any communication device for example, in mobile phones, satellite systems or instrumentation systems. For instance, in the receiver chain of a communication system, after the signal is amplified with the help of a low noise amplifier, it is down converted with a mixer and a local oscillator to produce an intermediate frequency which is then used for modulation and demodulation. If the phase noise of this oscillator is large, it might actually randomly bias the modulated signal which is then a problem during digital processing. Similarly, in the case of a radar system, the oscillator performance is very critical for the phase noise close to the carrier that can partially or completely mask the target signal being measured.

By definition, phase noise is the frequency domain representation of rapid, short-term, random fluctuations in the phase of a waveform, caused by time domain instabilities. The fluctuations manifest themselves as sidebands which appear as a noise spectrum spreading out either side of the signal. It is a key parameter in radio communication systems as it can significantly affect the performance of systems. Phase noise on the local oscillators within the system can affect specifications such as reciprocal mixing and the noise floor. For transmitters it can affect the wideband noise levels that are transmitted. Additionally, it can affect the bit error rate on systems using phase modulation as the phase shift may just cause individual bits of data represented by the phase at the time to be misread.

The results clearly show that electromagnetic band-gap structures or photonic crystals (PC) can be utilized for application in high frequency oscillators directly in fundamental mode with great benefits in obtaining ultra-high Q-factor and therefore low phase noise; and with better performance than alternative state-of-art technologies such as crystal oscillators in combination with frequency multiplication or frequency synthesis causing an increase in the overall phase noise by 20 log rule.

By successfully demonstrating the experiment of using electromagnetic band-gap structures with oscillators, it is a great contribution towards the solution of the problem of high phase noise affecting high frequency oscillators operating at millimetre-wave band.

3.2. MOTIVATION

Today, the reference oscillators based on quartz resonators are limited in the frequency of operation to a maximum of 100 MHz's. Deriving GHz's range signals from this reference requires frequency multiplication or frequency synthesis. However, the multiplication increases the phase noise of the output signal according the 20 log of multiplication factor and it also increases the complexity of the circuits. Obviously, it would be very desirable if the reference signal could be generated readily at a higher frequency. This would require, however, a high-Q resonator operating preferably at several GHz. Additionally, oscillators operating directly at fundamental mode in high frequency based on ceramic resonators offer poor phase noise close to carrier, poor stability and normally not available above 15 GHz.

Research papers and laboratory demonstrations have shown that dielectric resonators made from low-loss materials such as photonic crystal resonators [1] may become an interesting alternative to conventional room-temperature passive millimetre-wave resonators used in reference and high frequency oscillators, and important components for future millimetre-wave and terahertz communication and radar systems. Resonators based on this technology have recently been demonstrated with Q-factor values greater than 8.000.

The frequencies of interest investigated for the design of the high Q-factor resonator were identified assessing potential scenarios of application. The design parameters are scalable in frequency, and in principle EBG resonators can be designed to operate in any range of the millimetre-wave and terahertz regions of the electromagnetic spectrum. The limitations and impracticability are in terms of realisation ranges from the accuracy used in the fabrication process (due to etching effects affecting its performance) to the size of the structure that must fit into the silicon wafer.

Each scenario and respective frequency band investigated are based on the study where disruptive technologies were introduced for the space and ground segments with 2020 year as time horizon [2] to meet users need for higher throughput data rate in digital communication systems while achieving a dramatic reduction of unit cost in satellite fixed broadband capacity as well a scenario used in scientific experiments for space research. The main idea is to establish the design of the resonator operating directly in fundamental mode instead of using multiplication or frequency synthesis, as usually adopted in industrial designs.

The two last decades have seen a dramatic change in the development of the telecommunication services moving from low data rate to tens of Mbps thanks to the development of advanced technology (e.g. asymmetrical digital subscriber lines, cable, etc.). This caused a revolution since it enabled the development of a globalised and information-based society.

In this context, the Europe 2020 strategy has underlined the importance of broadband access deployment to promote social inclusion and boost competitiveness in the EU. The objectives is to provide basic broadband access to all Europeans by 2013 and to ensure that by 2020 all Europeans have access to much higher internet speed above 30 Mbps and 50% or more European households subscribe to internet connections above 100 Mbps. This translates into adopting

highly efficient modulation schemes such as M-PSK and M-QAM where the phase noise affects the symbol representation in the constellation diagram. The higher is the modulation cardinality, the more sensitive the system is to imperfections in the radio transport. The technology roadmap derived in the course of the study [2] clearly shows that a high degree of innovation would be required by the European and Canadian industry to develop Terabit/satellite in 2020 timeframe. The Figure 3.2-1 provides the capacity that can be reached by each investigated scenario and associated costs per Gbps.

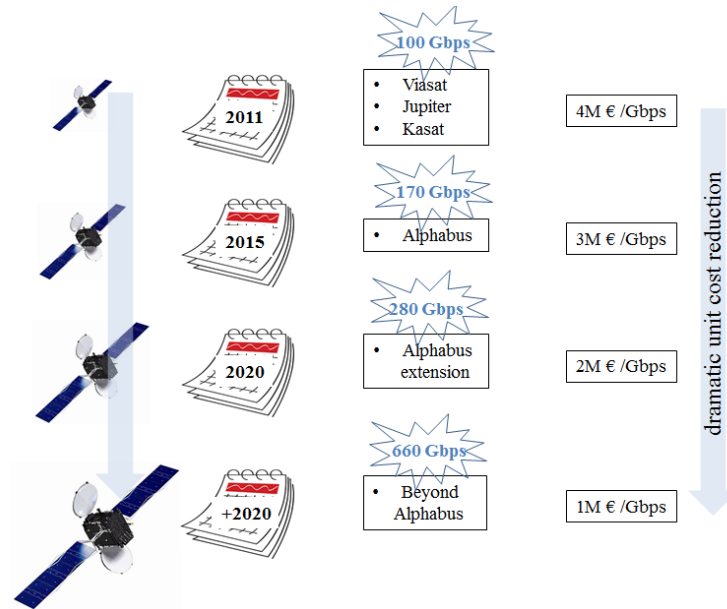


Figure 3.2-1 Capacity reached by each investigated scenario and associated costs [2].

Once the user needs have been fixed, the design objectives have been to maximise the capacity for each investigated system architecture. For each scenario different architectures have been evaluated at system and sub-system level. Some scenarios were derived as can be seen in Figure 3.2-2.

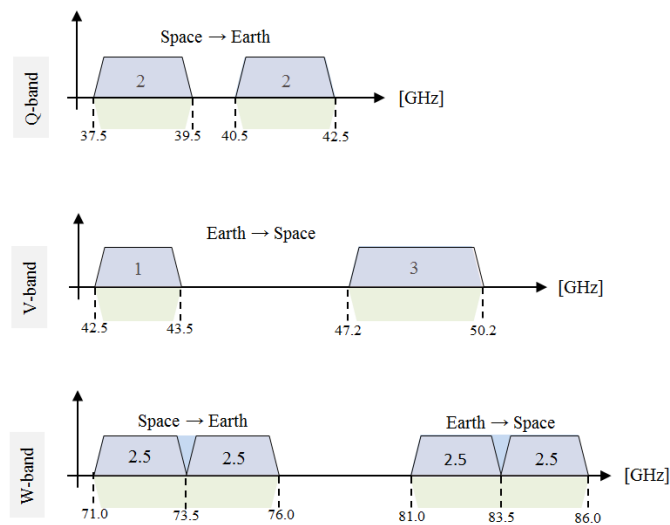


Figure 3.2-2 Scenarios retracting the frequency plan for space and ground segments in the bands Q, V and W to meet users' needs for high throughput satellite and scientific experiments for space research.

Based on the scenarios of Figure 3.2-2, the Q-band is mainly used for satellite communications, terrestrial microwave communications and for radio astronomy studies such as millimetre and submillimetre astronomy radio telescopes. It tends to be a concurrent subset of both the IEEE designated Ka-band and V band. The V-band is not heavily used, except for millimetre wave radar research and other kinds of scientific research. The W-band is characterized by an atmospheric window at 94 GHz and used for imaging millimetre-wave radar applications in astronomy, defence and security applications.

However, the choice for the resonator design shall be based in scenarios encompassing frequency conversion between two bands as can be seen in Figure 3.2-3. The scenarios are derived from studies conducted by the European Space Agency (ESA) reports for Terabit satellite system study emphasizing disruptive technologies roadmaps crossed with the study [2] done in the Europe 2020 Flagship Initiation, Innovative Union from the European Commission.

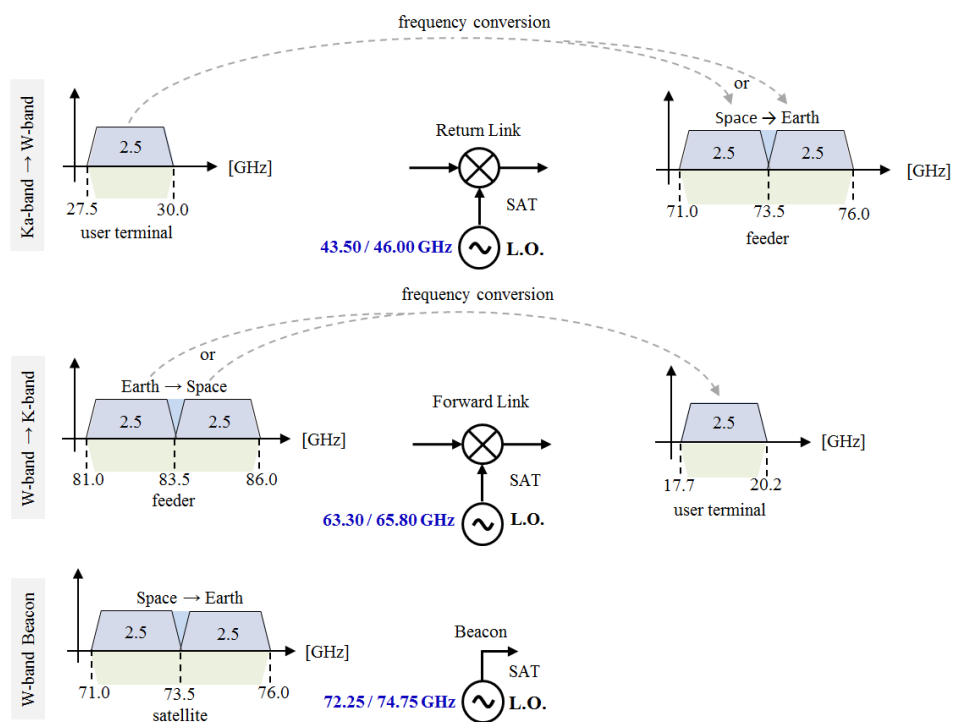


Figure 3.2-3 Scenarios retracting the frequency plan for space and ground segments between several bands and the respective local oscillator (L.O.) frequency used in the up and down-converters.

The first choice for the resonator targets the scenario where a frequency converter has a local oscillator operating at 46 GHz, therefore enabling up-conversion of a received signal in the Ka-band into a segment of the W-band. Analogically, other frequency bands and segments could have been chosen for the resonator design.

It is important to highlight once more the key aspect behind the high throughput data scenarios retracted in Figure 3.2-3, which are justified by the necessity of local oscillators possessing extremely low phase noise that can cope with the minimum requirements for phase noise versus frequency offset, therefore attending complex modulation schemes with data rates as function of the channel bandwidth for a fixed signal-to-noise ratio.

This is achieved by carefully choosing a resonator with characteristics covered in this thesis study. The primary and qualitative aspects of the resonator are basically its unloaded-Q and associated intrinsic dielectric losses.

In conclusion, the investigation of ultra-high Q-factor photonic resonators will enable high frequency oscillator application to operate directly at fundamental mode with low phase noise.

4. RESONATOR DESIGN

4.1. ELECTROMAGNETIC BAND-GAP STRUCTURE THEORY

The scientific community have been fascinated by the existence of periodic structures in nature. Once these structures interact with electromagnetic waves many unique properties can occur. Such properties are mainly characterised by frequency stop-bands, pass-bands, and band-gaps as well as waveguides. Many terminologies are currently being used to classify the structures depending on the domain of application and frequency range of operation.

Within the millimetre-wave region of the electromagnetic spectrum these structures are classified under the terminology of “Electronic Band-Gap (EBG)”. They are also known as “Photonic Crystals (PC)”, however this terminology is often applicable to structures operating in the range of optical frequencies.

Electromagnetic band-gap crystals are dielectric materials that contains a periodicity in structure generating a range of forbidden frequencies called band-gap. The electromagnetic modes with energy lying within a band-gap cannot propagate through the crystal and therefore obey the forbidden regions in frequency. The band-gaps must exist in all wave vector values in the Brillouin zone for the crystal under analysis.

The dielectric periodicity creates a band-gap in the electromagnetic dispersion curves for those electromagnetic waves that propagate perpendicular to the layers. The one-dimensional electromagnetic band-gap is similar to ideal reflective mirrors. This motivated the creation of two-dimensional and three-dimensional crystals in which there is a band-gap, allowing unprecedented control and manipulation of the electromagnetic waves.

A two-dimensional structure is periodic along two of its axes and homogeneous along the third. Two types of two-dimensional structures are considered. The first one is a structure formed by a square lattice of dielectric columns of dielectric constant ϵ_1 in a different background material of dielectric constant ϵ_2 . The second type is a structure made by arranging the dielectric columns in a triangular lattice.

The Figure 4.1-1 illustrates the first type of two-dimensional periodic structure, denominated square and triangular lattices of columns of high dielectric constant ϵ_1 in a background of low dielectric constant ϵ_2 . The lattice structures consist of a periodic array of parallel dielectric columns of circular cross section and dielectric constant ϵ_1 whose intersections with a perpendicular plane forms a square lattice. The dielectric columns are embedded in a dielectric material whose dielectric constant is ϵ_2 .

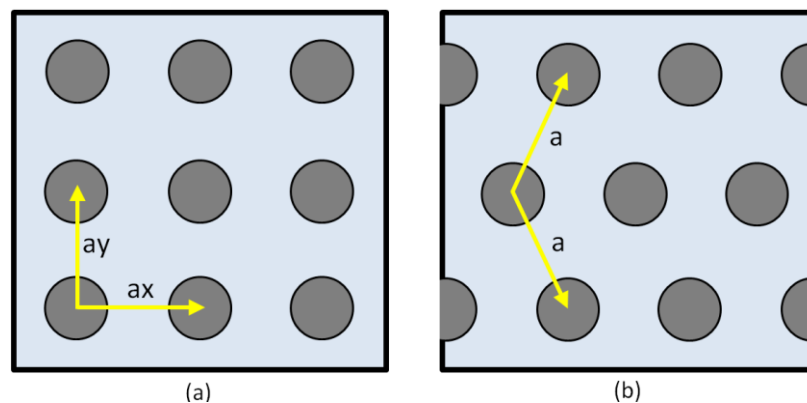


Figure 4.1-1: (a) The two-dimensional square lattice of columns of high dielectric ϵ_1 (shown in blue) in an background of low dielectric constant ϵ_2 (b) The two-dimensional triangular lattice of columns of high dielectric constant ϵ_1 (shown in blue) in a background of low dielectric constant ϵ_2 .

The electromagnetic waves in electronic band-gap structures encompass the solution of the Maxwell's equation. One fundamental aspect of the Maxwell's equation is that they can be solved exactly and the other aspect is that there is no fundamental length scale.

Classical phenomena in electromagnetics are governed by the Maxwell's equation according to,

$$\nabla \cdot \mathbf{D} = 4\pi\rho \quad (4.1)$$

$$\nabla \cdot \mathbf{B} = 0 \quad (4.2)$$

$$\nabla \times \mathbf{E} = -\frac{1}{c} \frac{\partial \mathbf{B}}{\partial t} \quad (4.3)$$

$$\nabla \times \mathbf{H} = \frac{1}{c} \frac{\partial \mathbf{B}}{\partial t} + \frac{4\pi}{c} \mathbf{J} \quad (4.4)$$

The displacement (\mathbf{D}) and electric (\mathbf{E}) fields are associated to each other through the following constitutive relation:

$$D_i = \sum_j \epsilon_{ij} E_j + \sum_k \chi_{ijk} E_j E_k + O(E^3) \quad (4.5)$$

A certain number of assumptions are made for the equation 4.5. First, for simplicity, it is assumed the field strengths so the response of materials to electric field is linear and therefore only linear terms in equation 4.5 are considered. Secondly, the dielectric material is isotropic, therefore \mathbf{E} and \mathbf{D} fields are related by a scalar dielectric constant ϵ_r . The third assumption considers the dispersion of dielectric materials is ignored, therefore ϵ_r can be assumed as a real part.

Encompassing all assumptions, the following relation between \mathbf{E} and \mathbf{D} fields is obtained,

$$\mathbf{D} = \epsilon_r \mathbf{E} \quad (4.6)$$

\mathbf{B} and \mathbf{H} are related to one another through the following constitutive relation,

$$\mathbf{B} = \mu \mathbf{H} \quad (4.7)$$

For the majority of dielectric materials, the magnetic permeability μ is equal to unity, therefore $\mathbf{B} = \mathbf{H}$.

Assuming there is no free electric charge ρ ($\rho_{\text{free}}=0$) or current \mathbf{J} ($\mathbf{J}_{\text{free}}=0$), the Maxwell's equation 4.1-4.4 can be reduced to,

$$\nabla \cdot \mathbf{D} = 0 \quad (4.8)$$

$$\nabla \cdot \mathbf{B} = 0 \quad (4.9)$$

$$\nabla \times \mathbf{E} = -\frac{1}{c} \frac{\partial \mathbf{B}}{\partial t} \quad (4.10)$$

$$\nabla \times \mathbf{H} = \frac{1}{c} \frac{\partial \mathbf{D}}{\partial t} \quad (4.11)$$

From equations 4.6 and 4.11, the following equation is obtained,

$$\nabla \times \mathbf{H}(\mathbf{r}) - \frac{1}{c} \frac{\partial}{\partial t} (\epsilon(\mathbf{r})\mathbf{E}) = 0 \quad (4.12)$$

In the frequency domain, the Maxwell's equation are harmonic functions of time t of a given angular frequency ω . The electric and magnetic fields can be decomposed as follows,

$$\mathbf{H}(\mathbf{r}, t) = \mathbf{H}(\mathbf{r})e^{i\omega t} \quad (4.13)$$

$$\mathbf{E}(\mathbf{r}, t) = \mathbf{E}(\mathbf{r})e^{i\omega t} \quad (4.14)$$

Rearranging and substituting the equations 4.13 and 4.14 into equations 4.10 and 4.12 results,

$$\nabla \times \mathbf{E}(\mathbf{r}) + i\left(\frac{\omega}{c}\right)\mathbf{H}(\mathbf{r}) = 0 \quad (4.15)$$

$$\nabla \times \mathbf{H}(\mathbf{r}) - i\left(\frac{\omega}{c}\right)\epsilon(\mathbf{r})\mathbf{E}(\mathbf{r}) = 0 \quad (4.16)$$

Dividing by $\epsilon(\mathbf{r})$ on both sides of the equation 4.16 and taking the curl, the following equation is obtained,

$$\nabla \times \frac{1}{\epsilon(\mathbf{r})} \nabla \times \mathbf{H}(\mathbf{r}) - i\left(\frac{\omega}{c}\right) \nabla \times \mathbf{E}(\mathbf{r}) = 0 \quad (4.17)$$

Using the equation 4.12, the following equation is obtained,

$$\nabla \times \frac{1}{\epsilon(\mathbf{r})} \nabla \times \mathbf{H}(\mathbf{r}) - \left(\frac{\omega}{c}\right)^2 \mathbf{H}(\mathbf{r}) = 0 \quad (4.18)$$

Rearranging the equation, a main equation for the EBG structure can be obtained. In the absence of external currents and sources, the Maxwell's equation can be re-written in the following form which is similar denoted in the Schrödinger equation,

$$\nabla \times \frac{1}{\epsilon(\mathbf{r})} \nabla \times \mathbf{H}(\mathbf{r}) = \left(\frac{\omega}{c}\right)^2 \mathbf{H}(\mathbf{r}) \quad (4.19)$$

This can be translated into an electromagnetic eigenvalue problem, so the left term of the equation 4.19 can be treated as an operator Θ , operating on $\mathbf{H}(\mathbf{r})$. The simple change in notation

makes the rearranged equation look like an eigenvalue problem, with $c=1/\sqrt{\epsilon_0\mu_0}$ the speed of light in vacuum.

$$\Theta H(r) = \left(\frac{\omega}{c}\right)^2 H(r) \quad (4.20)$$

The master equation so-called eigenvalue equation, with the application of the Hermitian operator (Θ) to the magnetic field H yields a scalar term multiplying it times the magnetic field H .

The $H(r)$ and $E(r)$ fields from equations 4.13 and 4.14 are amplitudes of the electric and magnetic fields respectively as a function of the position r , and $e^{i\omega t}$ describes the harmonic time dependence of the fields. In terms of plane-wave expansion method, it is convenient to solve for $H(r)$ and determine $E(r)$ via equation 4.15. The master equation 4.19 has orthogonal solutions each having real eigenvalues $\left(\frac{\omega}{c}\right)^2$. Because of the periodicity of the dielectric constant for the EBG structure, Bloch's theorem can be applied. It states that for any kind of periodic dielectric constant variations of the solution to the master equation are of the form $H(r) = e^{ik \cdot r} u_{n,k}(r)$ with eigenvalues $\omega_n(k)$. $u_{n,k}(r)$ is an envelope function with the periodicity of the EBG lattice satisfying:

$$(\nabla + ik) \times \frac{1}{\epsilon_r(r)} (\nabla + ik) \times u_{n,k}(r) = \left(\frac{\omega_n(k)}{c}\right)^2 u_{n,k}(r) \quad (4.21)$$

Where k is the Bloch wave vector and $n=1,2,\dots$ is an index that labels the discrete eigenvalues. These eigenvalues $\omega_n(k)$ are continuous functions of k , forming discrete bands in the dispersion diagram. In the plane-wave expansion (PWE) method the solutions of equation 4.19 are expanded in a truncated basis of plane waves. These plane waves can easily be expressed as a Fourier expansion series in k -space (reciprocal space), which facilitates the computation.

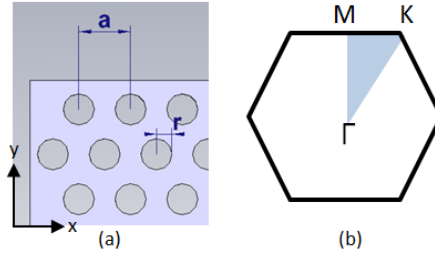


Figure 4.1-2 (a) The two-dimensional triangular lattice or air holes in a high dielectric material along the primitive periodicity and radius. (b) The First Brillouin Zone (FBZ), with high symmetry points.

Figure 4.1-2 depicts the particular case of EBG's with a triangular lattice forming an hexagonal shape; the First Brillouin Zone (FBZ) is the locus of points in reciprocal space that are closer to the origin of the reciprocal lattice than they are to any other reciprocal lattice points, by all of symmetries in the point group of the lattice. Another definition is the set of points in k -space that can be reached from the origin without crossing any Bragg plane. The Bragg plane is a plane in reciprocal space which bisects a reciprocal lattice vector, k , at right angles.

The dispersion diagram of periodic structures such as electromagnetic band-gap structures can be modelled using a single cell with periodic boundaries in XY -direction. An eigenmode solver can deliver the results for the so-called Brillouin zone, by sweeping both angles phase X and phase Y

between periodic side walls. Sweeping the phase will mimic sweeping the wavelength and frequency of an incoming wave respectively.

A wavenumber (k) is key parameter to describe the propagation property of the electromagnetic waves in EBG's structures. In a lossless case, the phase constant is $\beta=k$. Being the phase constant (β) in function of angular frequency (ω), once the phase constant is obtained, the phase velocity (v_p) and group velocity (v_g) can be derived as follows,

$$v_p = \frac{\omega}{\beta} \quad \text{and} \quad v_g = \frac{d\omega}{d\beta} \quad 4.22$$

The field distribution of a surface wave is determined such as field variation in a transverse direction. For plane waves in free space, the relationship between β and ω is a linear function:

$$\beta(\omega) = K = \omega\sqrt{\mu_0\epsilon_0} \quad 4.23$$

For propagating waves in EBG's surface, the exact expression for the wavenumber K has not a trivial solution and either a full wave or eigenmode simulation is necessary in order to determine it. The relation between β and ω is plotted and referred to a dispersion diagram.

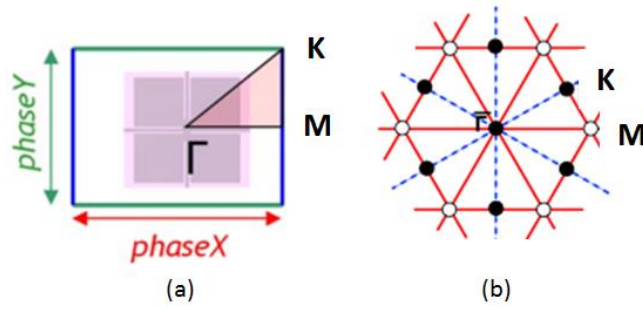


Figure 4.1-3 (a) Brillouin zone diagram showing sweeping angles phase X and Y. (b) Diagram showing the first Irreducible Brillouin Zone (IBZ) for EBG's with triangular lattice.

For EBG's periodic structure, the field distribution of a surface wave is also periodic with phase delay determined by the wavenumber k (or β) and periodicity p . Therefore each surface wave mode can be decomposed into an infinite series of space harmonic waves as follows,

$$\vec{E}(x, y, z) = \sum_{+\infty}^{+\infty} \vec{E}_n(y, z) \cdot e^{-j\beta_{xn}x}, \beta_{xn}(\omega) = \beta_x(\omega) + n \quad 4.24$$

In equation 4.24, it is assumed the periodic and propagation direction in the x direction. Although these space harmonics have different phase velocities, they share the same group velocity and cannot exist individually because each single harmonic does not satisfy the boundary conditions of the periodic structure. Only their sum satisfies the boundary conditions, and therefore considered the same mode.

The dispersion curve $\beta_x(\omega)$ is periodic along β axis with periodicity of $2\pi/p_x$, therefore the single period $0 \leq \beta_{xn} \leq 2\pi/p_x$, the Brillouin zone. Extending it to two-dimensional periodic structures, where the Brillouin zone becomes two-dimensional square are, the following expression is obtained:

$$0 \leq \beta_{xn} \leq 2\pi/p_x, 0 \leq \beta_{yn} \leq 2\pi/p_y \quad 4.25$$

In a two-dimensional triangular lattice structure, the primitive lattice vectors (\vec{t}_n) are the smallest vectors that describe the arrangement. The reciprocal lattice vectors (\vec{T}_n) are the smallest vectors that describe the arrangement in the reciprocal space, and are calculated according:

$$\vec{T}_1 = \frac{2\pi(\vec{t}_2 \times \vec{t}_3)}{\vec{t}_1(\vec{t}_2 \times \vec{t}_3)} \quad 4.26$$

$$\vec{T}_2 = \frac{2\pi(\vec{t}_3 \times \vec{t}_1)}{\vec{t}_1(\vec{t}_2 \times \vec{t}_3)} \quad 4.27$$

$$\vec{T}_3 = \frac{2\pi(\vec{t}_1 \times \vec{t}_2)}{\vec{t}_1(\vec{t}_2 \times \vec{t}_3)} \quad 4.28$$

Figure 4.1-4 shows an hexagonal Bravais lattice in two dimensions, with periodicity, a , and angle $\varphi = 120^\circ$ being $|t_1| = |t_2|$. The primitive vectors are known as,

$$t_1 = (a, 0) \quad 4.29$$

$$t_2 = \left(-\frac{1}{2}a, \frac{a\sqrt{3}}{2}\right) \quad 4.30$$

Calculating the vectors in reciprocal space, the relations are :

$$T_1 = \left(\frac{2\pi}{a}, \frac{2\pi}{a\sqrt{3}}\right) \quad 4.31$$

$$T_2 = \left(0, \frac{4\pi}{a\sqrt{3}}\right) \quad 4.32$$

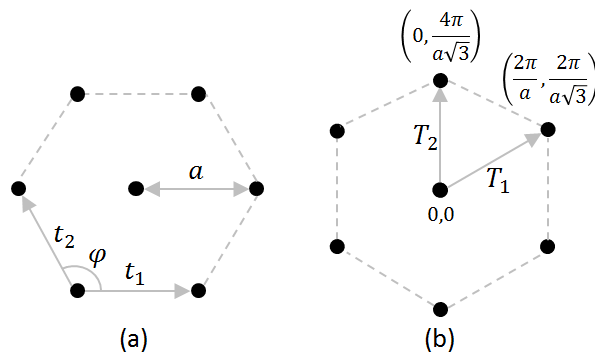


Figure 4.1-4: (a) The primitive lattice vectors and (b) the reciprocal lattice vectors of the Brillouin zone.

The irreducible zone is not unique and can be rotated by $n \cdot 60^\circ$. In the eigenmode solver a unitary cell with square boundaries is deployed in order to calculate the vectors of interest (Γ, M, K) according the table below. With those results, the sweep of interest is obtained in the following order $\Gamma \rightarrow M \rightarrow K \rightarrow \Gamma$.

	Γ	M	K
φ_x	0	0	120
φ_y	0	360	360

Table 4.1-1 Table showing the vectors of interest (Γ, M, K) in function of φ_x and φ_y for the Brillouin zone.

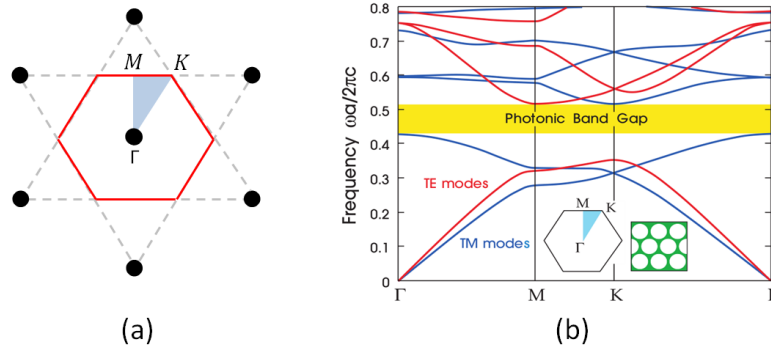


Figure 4.1-5: (a) Reciprocal space showing the irreducible part of the first Brillouin zone, so called Irreducible Brillouin Zone (IBZ) in blue color. (b) The dispersion diagram showing the band-gap of a two-dimensional triangular lattice with vacuum columns radius (r) equals $0.48a$ and $\epsilon_r = 13$. The blue lines represent TM bands and red lines represent TE bands.

4.2. HIGH RESISTIVITY SILICON MATERIAL

Traditional passive resonators employing metal cavities have their Q-factor limited by the resistive losses in the metal, therefore dielectric resonators made of low-loss and high resistivity material are an interesting alternative to overcome the problem with the limited Q-factor. Low-loss and high performance dielectric materials are crucial parts employed in oscillators for high performance telecommunication systems.

The dielectric material chosen for the investigation and characterisation of the resonator is the HiRes™ (High Resistivity) silicon for GHz and THz applications from TopSil Global Wafers A/S company in Denmark. Topsil is the world leading supplier of high resistivity silicon materials for a number of applications focusing the R&D in products with the highest resistivities ever measured on silicon wafers RF MEMS switches, high Q-factor inductors and capacitors, GHz transmitter and receiver circuits, GHz mixers and amplifiers, low-loss transmission lines as well micro-machined thin film bulk acoustic resonators. The main characteristics offered by the HiRes™ silicon substrate material are displayed below in Table 4.2-1. The information given in the table when not intrinsic from the bulk material are approximated to 50 GHz range. High resistivity silicon is defined as monocrystalline silicon having a bulk resistivity larger than $1 \text{ k}\Omega\text{cm}$. Although Czochralski grown monocrystalline silicon is often specified up to $1.5 \text{ k}\Omega\text{cm}$, Float Zone grown monocrystalline silicon is the only

growth technology that is able to have bulk resistivities above 1 kΩcm with good tolerance control of the resistivity along the ingot from where the silicon wafers is sliced. Topsil manufactures and sells Float Zone grown high resistivity silicon (HiRes™) with bulk resistivities approaching 70 kΩcm.

Growth Method	HiRes™ Float Zone Silicon
Orientation	1-0-0
Bulk Resistivity	> 103 Ωcm
Thermal Conductivity	1.5 W/cm-K
Dielectric Constant	11.66
Loss Tangent	2.3 x 10 ⁻⁵
Electrophoretic Deposition (EPD)	< 100 cm ³
Bandgap (300K)	Indirect 1.14 eV
Epitaxial System	SiGe-Si, GaP-GaN
Schottky Barrier	0.65 eV (n-type)
Thickness	1000 ± 15 μm

Table 4.2-1 Main characteristics of the HiRes™ silicon substrate material

High resistivity silicon (HiRes) has several applications in different areas of physics and is one of the most transparent solid materials for electromagnetic waves at frequencies below 2.5 THz [3, 4].

The dielectric properties of silicon have been measured at a broad electromagnetic wave spectrum for microwave to infra-red frequencies and they are specified by complex relative permittivity ϵ_r or by complex refractive index n being equal to the square root of the complex relative permittivity. The complex permittivity is defined as:

$$\epsilon_r = \epsilon'_r - j\epsilon''_r - j\frac{\sigma}{\omega\epsilon_0} \quad 4.33$$

Where ϵ_0 is the permittivity of vacuum, ϵ_r is the relative complex permittivity, ϵ'_r is the real part of the relative complex permittivity, ϵ''_r is the imaginary part of the relative complex permittivity, ω is the angular frequency, and σ is the material conductivity. The imaginary part contains two terms and the first one is associated with dielectric losses and the second one with the material conductivity. The total dielectric loss tangent is given by,

$$\tan \delta = \frac{\text{Im}(\epsilon_r)}{\text{Re}(\epsilon_r)} = \tan \delta_d + \frac{\sigma}{\omega\epsilon_0\epsilon'_r} \quad 4.34$$

in which $\tan \delta_d = \epsilon''_r/\epsilon'_r$ denotes dielectric loss tangent associated with pure dielectric losses such as electronic and ionic polarization. The following values can be obtained for the dielectric constant ϵ_r and the loss tangent $\tan \delta$ [3, 4]:

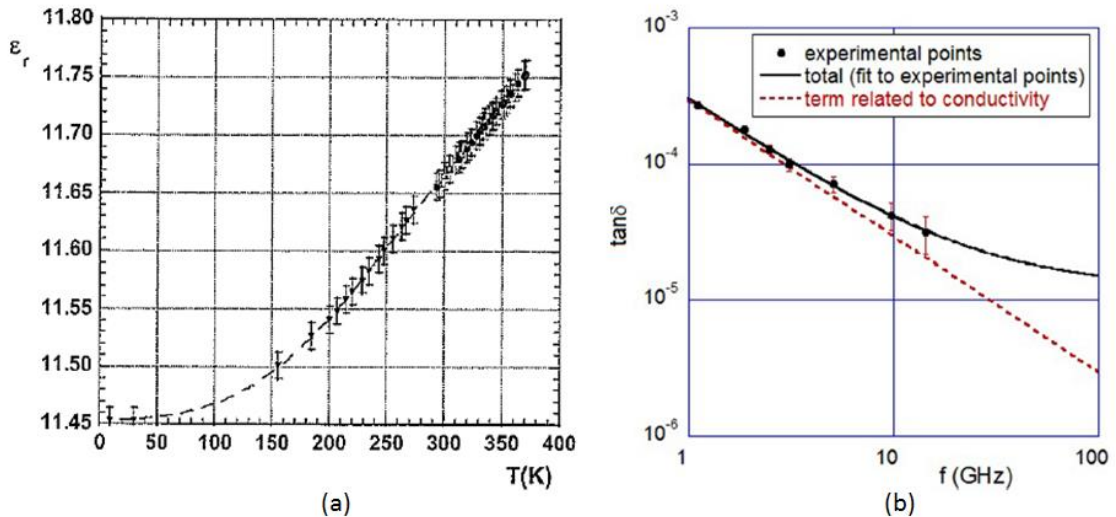


Figure 4.2-1 (a) The permittivity versus temperature for a sample with $d=15.455$ mm. Experimental data points include result extracted from measurements employing quasi- TEM_{011} mode in two cavities (6.62 GHz and 6.69 GHz) and the third TE_{10} mode (11.5 GHz) in the second cavity. (b) The total dielectric loss tangent versus frequency for high-purity silicon with semi-insulating properties.

The input data of permittivity and tangent loss parameters of the substrate for the simulation tool were taken from the Figure 4.2-1 and also through the article on materials for millimetre and submillimetre optics [6] on high-resistivity Silicon material from J. W. Lamb.

In Figure 4.2-1, the total dielectric constant for the HiRes™ material at room temperature (293 K°) taken from (a) is 11.66, while for the total dielectric loss tangent is about 2.3×10^{-5} taken from the log graphic in (b). Those input data were considered valid to 45 GHz range into the simulation, which in fact will show good correlation of results obtained between measurement and simulation covered in sub-chapter 4.5. A cassette with twenty-five double side polished silicon wafers (HiRes™) of 1 mm thickness and 100 mm diameter each was acquired from TopSil company for the prototypes fabrication.

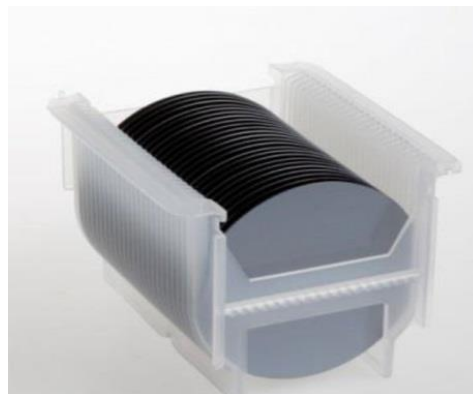


Figure 4.2-2 The cassette box of HiRes™ material from TopSil company containing 25 individual silicon wafers of 100 mm diameter and 1 mm thickness each, acquired for the fabrication of prototypes.

4.3. HIGH Q-FACTOR RESONATOR DESIGN

Silicon resonators based on electronic band-gap are artificial materials whose dielectric properties exhibit spatial periodicity in one, two or three dimensions. In this work, two dimensional periodic structures with finite extension into the third dimension are proposed.

The Silicon wafer material (HiRes™) properties are then used in the design of the resonator structure, which is formed by a rectangular slab composed of a periodic arrangement of air holes and where electromagnetic waves can be guided through or reflected due to the total internal reflection.

The range of frequencies which are not propagated (forbidden zone) within the slab is called band-gap. An electromagnetic band-gap is created by the triangular periodic arrangement of two dielectric materials with contrasting permittivities where no propagation mode is observed at constant frequency within the slab.

On the contrary, a defect feed waveguide designed at input and output of the slab allows the energy to propagate. The energy is coupled via two triangular shape tapers located at the input and output of the rectangular slab designed to ensure a smooth transition from the WR-19 waveguides.

A number of guided modes described by their field distribution are orthogonal to the propagation direction and by the in-plane wave number along the propagation direction. The condition which satisfies the total internal reflection is determined by the modes with an in-plane wave number $k_{\parallel} > \omega/c$, where c constitutes the speed of light in the vacuum and ω is the angular frequency. To the contrary, modes which infringe this condition, $k_{\parallel} < \omega/c$, remain in the Brillouin zone with the irreducible region, known as light cone, where the respective modes can leak into free space.

The resonator, also known by defect cavity, is designed to be weakly coupled with the defect feeds. It consists either of a point defect or a line defect, normally in the symmetry area of the rectangular slab. The point defect is described when a single hole is omitted. As a result, the symmetry of the structure is broken and therefore localized modes arise with fields decaying exponentially. Since there are no propagation modes inside of the band-gap, the energy stored inside a localized mode cannot be transported along the slab, thus they are laterally confined.

The disadvantage of using this mode is that it implies in having strong lateral confinement and therefore wide spectrum of wave vectors. In this way, the part of the k-vector spectrum leaks to free space translating in part of the stored energy radiated and wasted. A line defect can be translated into an extension of the point defect by omitting few holes and behaves as standing waves inside a waveguide.

Because the large volume compared to point defect cavities, theoretically it can store more energy, accounting higher Q-factors. However in practice this is not necessarily observed [23], as the line defect cavity has to be carefully designed. To a successful design, the in-plane k-vector has to fit outside the light cone, $\omega < ck_{\parallel}$. It is expected that modes supported by the line defect cavity possess higher eigen-frequencies compared to a point defect cavity adopting the same lattice constant.

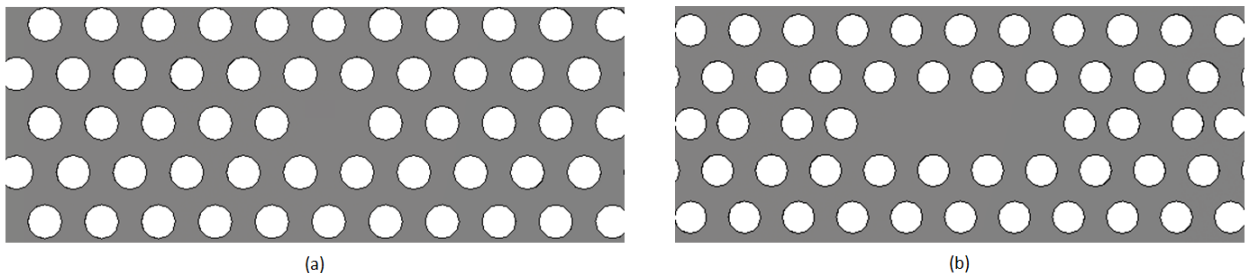


Figure 4.3-1 a) Lattice constant showing a point defect cavity where a single hole was omitted b) Lattice constant showing a line defect cavity where three holes were omitted.

The adjustment of the hole positions at the cavity edge make it possible to confine the energy fields. Due to the fact the in-plane mode are finite, the cavity mode contains energy inside of the light cone which can vertically leak out to free space. If the lateral dimensions of the slab are also finite, the defect mode can leak out in the horizontal direction and this decay of energy can be described by the Q-factor. The Q-factor is a figure of merit and is a parameter that describes how the under-damped of a resonator is, and characterises a resonator bandwidth relative to its center frequency. It is the ratio of power stored to power dissipated per radian of the oscillation. The total Q-factor of the cavity is given by:

$$\frac{1}{Q_{total}} = \frac{1}{Q_{vertical}} + \frac{1}{Q_{horizontal}} \quad 4.35$$

Where $Q_{vertical}$ and $Q_{horizontal}$ are determined by the out-of-plane radiation loss in the vertical and horizontal directions, respectively. In an analogous way, the Q-factor of a resonator circuit can be defined in terms of its stored energy and energy loss at the resonance angular frequency (ω_r) as shown below in (4.36) and (4.37).

$$Q = 2\pi \frac{\text{Energy Stored}}{\text{Energy Dissipated}} = \omega_r \frac{\text{Energy Stored}}{\text{Average Power Loss}} \quad 4.36$$

$$Q = \frac{F_{res}}{BW_{3\text{ dB}}} \quad 4.37$$

There are actually three Q-factors that can be defined, depending upon which loss is being considered as illustrated below in (4.38), (4.39), and (4.40).

$$Q_u = \omega_r \frac{\text{Energy Stored in the Resonator}}{\text{Energy Dissipated in the Resonator}} \quad 4.38$$

$$Q_e = \omega_r \frac{\text{Energy Stored in the Resonant Circuit}}{\text{Energy Dissipated in the External Circuit}} \quad 4.39$$

$$Q_L = \omega_r \frac{\text{Energy Stored in the Resonant Circuit}}{\text{Total Energy Dissipated}} \quad 4.40$$

The unloaded Q (Q_u) is a measure of quality of the resonant circuit itself. Infinite Q_u means that the resonant circuit is lossless. External Q (Q_e) is a measure of the degree to which the resonator circuit is coupled to the external circuitry. A relationship among the three Q factors is named loaded Q (Q_L) and can be derived from (4.41).

$$\frac{1}{Q_L} = \frac{1}{Q_e} + \frac{1}{Q_u} \quad 4.41$$

The loaded Q of the resonator, considering the external losses such as the waveguides and respective transition to coaxial, can be calculated using 4.37 and therefore establishing a

relationship with the unloaded Q derived as following in 4.41, the $|S_{21}|$ is the peak voltage transmission coefficient in linear scale at the resonance. The specific type of resonator designed within this work has been engineered to work with transverse electric (TE)-like electromagnetic band-gap since the electric field has only in-plane components.

A better estimation of the unloaded Q-factor, due to the weak coupling within the complete structure and on which it can be obtained directly from the simulated or measured full S-parameters is given by:

$$Q_u = \frac{Q_L}{1 - |S_{21}|} \quad 4.42$$

Where Q_L is the loaded Q-factor and S_{21} is the module of the forward transmission coefficient in linear scale at the peak of the resonance frequency (F_{res}), the coupling factor.

As previously mentioned, the range of frequencies which are not propagated within the slab is called band-gap. The first step in the design of the high Q-factor resonator is the determination of the band structure by calculating the eigenmodes of a single lattice cell. The eigenmodes of a single lattice cell are illustrated in Figure 4.3-3. Boundary conditions are applied in the single lattice cell to meet the symmetry conditions of the expected modes.

Numerical simulation techniques were initially employed using CST Studio Suite™ software to uphold and characterise the TE-like band-gap. The structure is periodic and no propagation mode (also called band gap) exists inside the band gap, the energy stored inside a localised mode cannot be transported through the slab. The band gap of this structure was calculated using the eigenmode solver from CST Studio Suite™.

The band-gap for the surface wave is determined by plotting the dispersion diagram over the irreducible Brillouin zone order $\Gamma \rightarrow M \rightarrow K \rightarrow \Gamma$. Periodic boundary conditions and a parameter sweep is used with the eigenmode solver.

The design of the silicon resonator, relies on a structure formed by a triangular lattice of air holes in a planar substrate. It assumes the characteristics of the high resistivity silicon material (HiRes™) having permittivity ϵ_r (45 GHz) ≈ 11.66 and loss tangent δ_t (45 GHz) $\approx 2.3 \times 10^{-5}$, which have been taken from Figure 4.2-1 and table 4.2-1.

The working frequency chosen for the oscillator which is fundamentally the same for the resonant frequency of the high Q-factor resonator is based in the first scenario (Ka-band to W-band) depicted in the top of the Figure 4.1-10. In order to up-convert the Ka-band segment from 27.5 to 30 GHz to the second segment in the W-band from 73.5 to 76 GHz, the required frequency for the local oscillator is 46 GHz.

In order to determine the propagation speed (c) of the electromagnetic waves in the dielectric media of the slab, the following equation is used:

$$c \approx \frac{c_0}{\sqrt{\epsilon_r}} \quad 4.43$$

Where c_0 represents the speed of light in the vacuum and ϵ_r is the dielectric constant (permittivity) of the slab. As the speed of light in the vacuum is 299,792.458 m/s and the

dielectric constant of the HiRes™ silicon wafer at 46 GHz is around 11.66, the propagation speed of the electromagnetic waves in the media is 87,795.332 m/s.

The calculation of the lattice constant, periodicity (a) of the slab, will determine the band-gap observed and is determined according its center frequency, $F_c = 46$ GHz. Therefore, (a) is determined according the equation below.

$$a \approx \frac{c_0}{\sqrt{\epsilon_r} \cdot F_{\text{res}}} \quad 4.44$$

A lattice constant (a) of 1908 μm is then obtained. The ratios h/a and r/a are found optimum respectively as 0.673 and 0.301 [7], fundamentally scalable to any frequency, where the parameters h and r represent the wafer thickness and radius of the air holes respectively.

The key parameter affecting the band-gap size is the slab thickness. However, a constrain is imposed to the wafer thickness, since it is determined by the quotient h/a equals to 1284 μm .

Unfortunately, the TopSil supplier does not provide any high-resistivity low loss wafer material ticker than 1000 μm . This implies that for maintaining about the same characteristics of gap bandwidth and respective frequency range while keeping a thickness of 1000 μm , a new lattice constant is needed. The concept used for the resonator design [7, 8] uses a planar form factor high resistivity silicon wafer substrate, named HiRes™, from TopSil company.

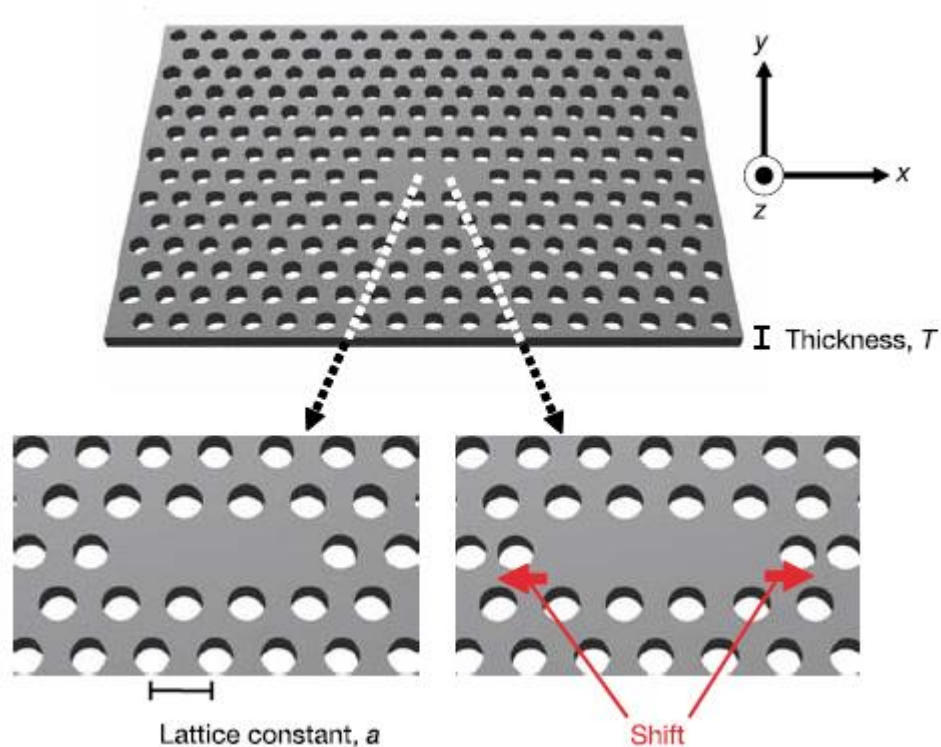


Figure 4.3-2 Illustration of the periodic EBG structure and defective cavity in the middle of a slab.

The geometrical dimensions of the complete structure are shown below in Figure 4.3-3.

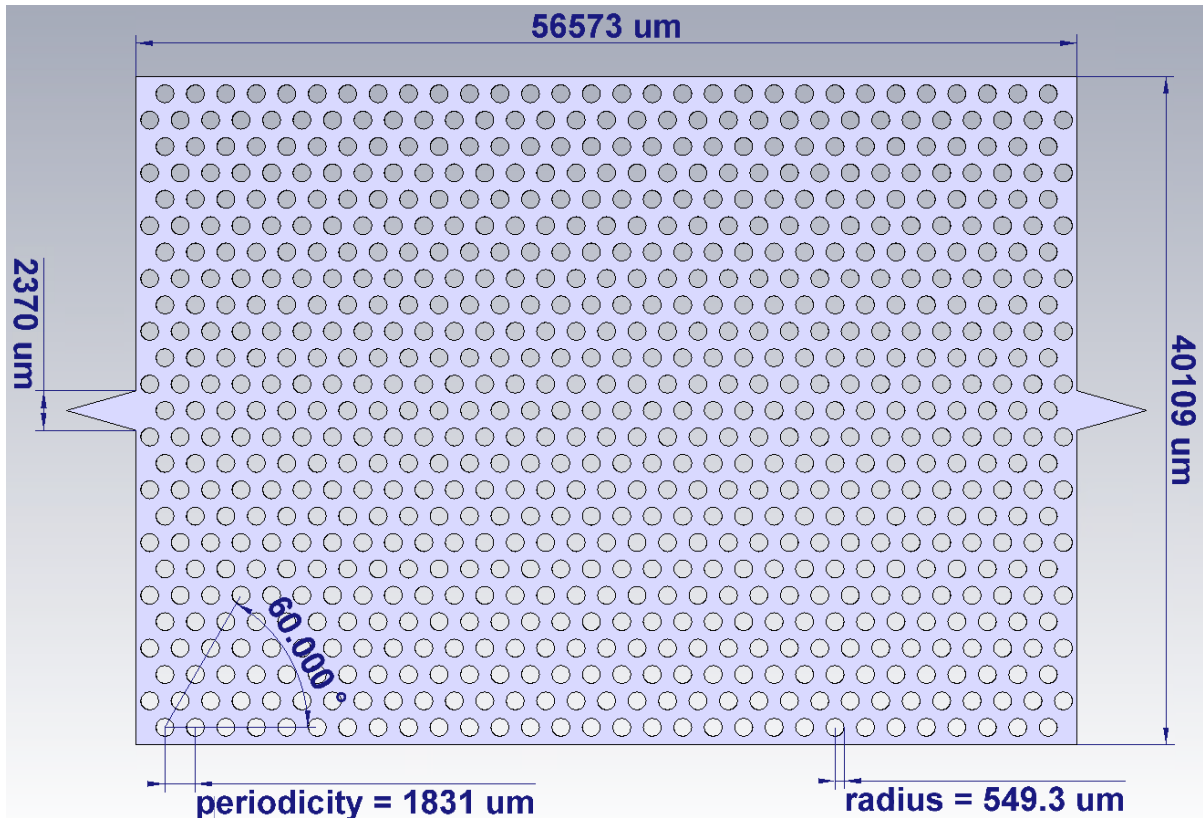


Figure 4.3-3 Illustration showing the EBG structure with its respective geometrical dimensions and smooth triangular tapers for the feed of WR-19 waveguides connection (TE-like).

At this point the eigenmode solver from CST Studio Suite™ is used to plot a dispersion diagram in order to cope with the new wafer thickness. A unit cell with chosen dimensions of $a = 1831 \mu\text{m}$, $r = 549.30 \mu\text{m}$ and $h = 1000 \mu\text{m}$ is deployed and the results are displayed below in the Figure 4.3-3.

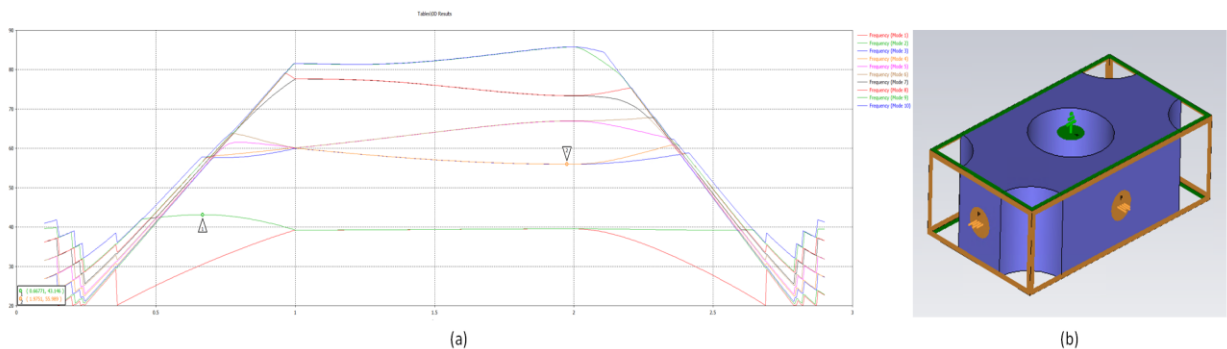


Fig. 4.3-4 a) Simulated dispersion diagram displaying 10 modes, band-gap showed from 43.14 GHz to 55.98 GHz b) Simulated unit cell of the EBG structure, eigenmode solver.

Similarly, a time-domain simulation of the complete structure is performed. A band-gap of approximately 13 GHz is observed, equivalent to a fractional bandwidth of 26%. The simulation results of the complete rectangular structure are shown below in Figure 4.3-5.

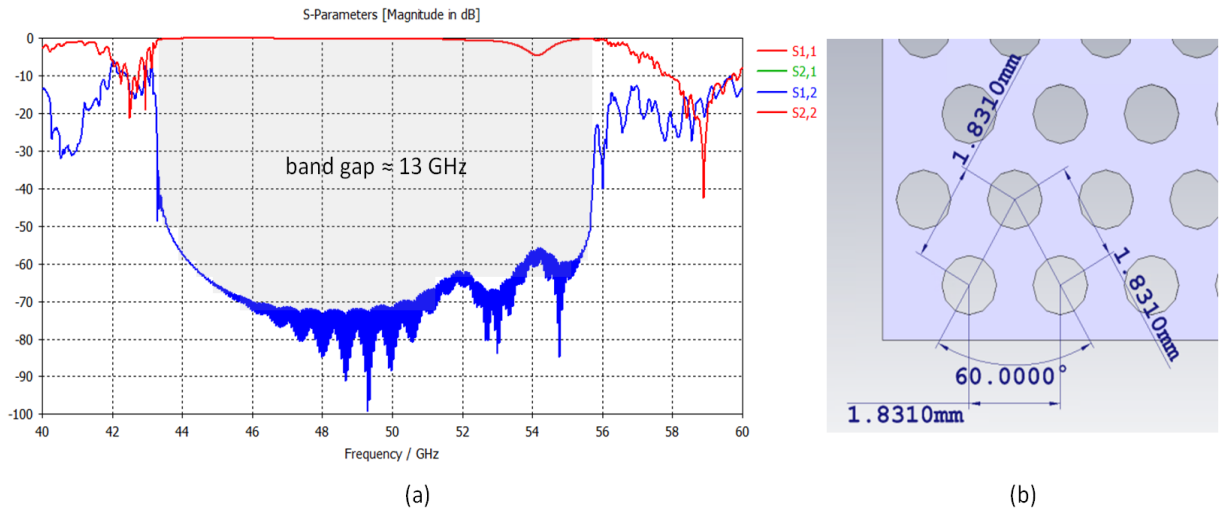


Figure 4.3-5 a) Simulated full two-port S-parameters from the EBG structure showing a band-gap of about 13 GHz b) Simulated periodicity of EBG lattice.

In addition to the dispersion diagram, the structure from Figure 4.3-4 is simulated using the time-domain solver of CST Studio Suite™. It is composed by a lattice of 30 horizontal and 25 vertical air holes, using the lossy substrate (HighRes) characteristics in order to observe the expected effects of the band-gap. The open boundary condition with free space surrounding the structure was used in the simulator. The structure is then excited with the fundamental TE₁₀ mode of the WR-19 waveguide and respective flange.

The table 4.3-1 below shows the main parameters used in the simulation of the EGB resonator:

Main Parameters	Value	Unit
Length of structure	56,573.00	μm
Width of structure	40,109.00	μm
Periodicity (a)	1,831.00	μm
Hole Radius (r)	549.30	μm
Thickness (h)	1,000.00	μm
Dielectric Constant (ϵ_r)	11.66	-
Loss Tangent (δ_d)	2.3×10^{-5}	-

The TE-like band-gap can be obtained through a full two-port S-parameters simulation. Scattering parameters or S-parameters describe the electrical behaviour of linear networks under steady-state stimulus by electrical signals, used primarily at microwave frequencies where it becomes difficult to measure voltages and currents directly. It is the response of an n-port network to signal(s) incident to any or all of the ports. The first number in the subscript refers to the responding port, while the second number refers to the incident port.

Equation 4.45 shows the S-parameter matrix for the two-port network. By definition, the S-parameter is a relationship between the reflected, incident power waves and is given by:

$$\begin{bmatrix} b_1 \\ b_2 \end{bmatrix} = \begin{bmatrix} S_{11} & S_{12} \\ S_{21} & S_{22} \end{bmatrix} \cdot \begin{bmatrix} a_1 \\ a_2 \end{bmatrix} \quad 4.45$$

The associated S-parameters definition is in terms of incident and reflected power waves at port n are the terms a_n and b_n respectively.

Expanding the matrix into equations gives:

$$b_1 = S_{11} \cdot a_1 + S_{12} \cdot a_2 \quad 4.46$$

$$b_2 = S_{21} \cdot a_1 + S_{22} \cdot a_2 \quad 4.47$$

The equation 4.46 and 4.47 establish a relationship between the reflected and incident power waves at each of the network ports, 1 and 2, in terms of the individual S-parameters, S_{11} , S_{12} , S_{21} and S_{22} . Considering an incident power wave at port 1 (a_1), it may result in waves exiting from either port 1 itself (b_1) or port 2 (b_2).

If port 2 is terminated in a load equal to the system impedance (Z_0), then the term b_2 will be totally absorbed making a_2 equal zero. Consequently, defining the incident voltage waves as $a_1 = V_1^+$ and $a_2 = V_2^+$ with reflected waves $b_1 = V_1^-$ and $b_2 = V_2^-$. Therefore, the following relationships can be established:

$$S_{11} = \frac{b_1}{a_1} = \frac{V_1^-}{V_1^+} \quad 4.48$$

$$S_{12} = \frac{b_1}{a_2} = \frac{V_1^-}{V_2^+} \quad 4.49$$

$$S_{21} = \frac{b_2}{a_1} = \frac{V_2^-}{V_1^+} \quad 4.50$$

$$S_{22} = \frac{b_2}{a_2} = \frac{V_2^-}{V_2^+} \quad 4.51$$

In overall terms, the two-port S-parameters have the following description:

- S_{11} is the input voltage reflection coefficient
- S_{12} is the reverse voltage gain
- S_{21} is the forward voltage gain
- S_{22} is the output voltage reflection coefficient

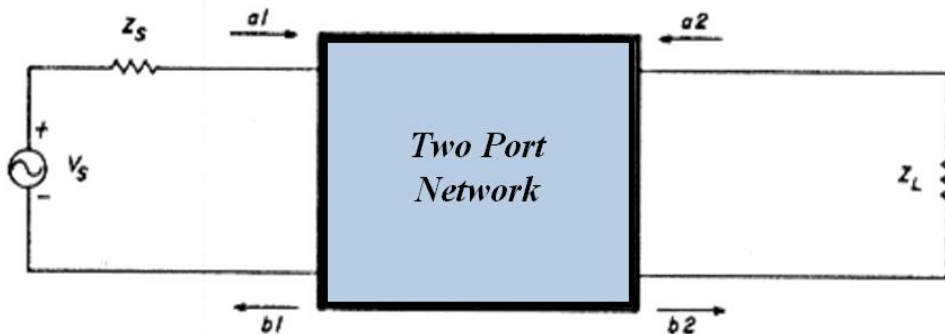


Figure 4.3-6 Generalized two-port network, characteristic impedance Z_0 .

For reciprocal networks $S_{21} = S_{12}$ and for symmetrical networks $S_{11} = S_{22}$. For anti-metrical networks $S_{11} = -S_{22}$. S-parameter magnitudes can be expressed in one of the two forms, linear magnitude or logarithmic based decibels (dB). Since S-parameter are complex voltage ratios, the

formula in decibels is $S_{ij} \text{ (dB)} = 20 \text{ Log } [S_{ij} \text{ (magnitude)}]$. The angle or phase of a complex S-parameter is almost always presented in degrees.

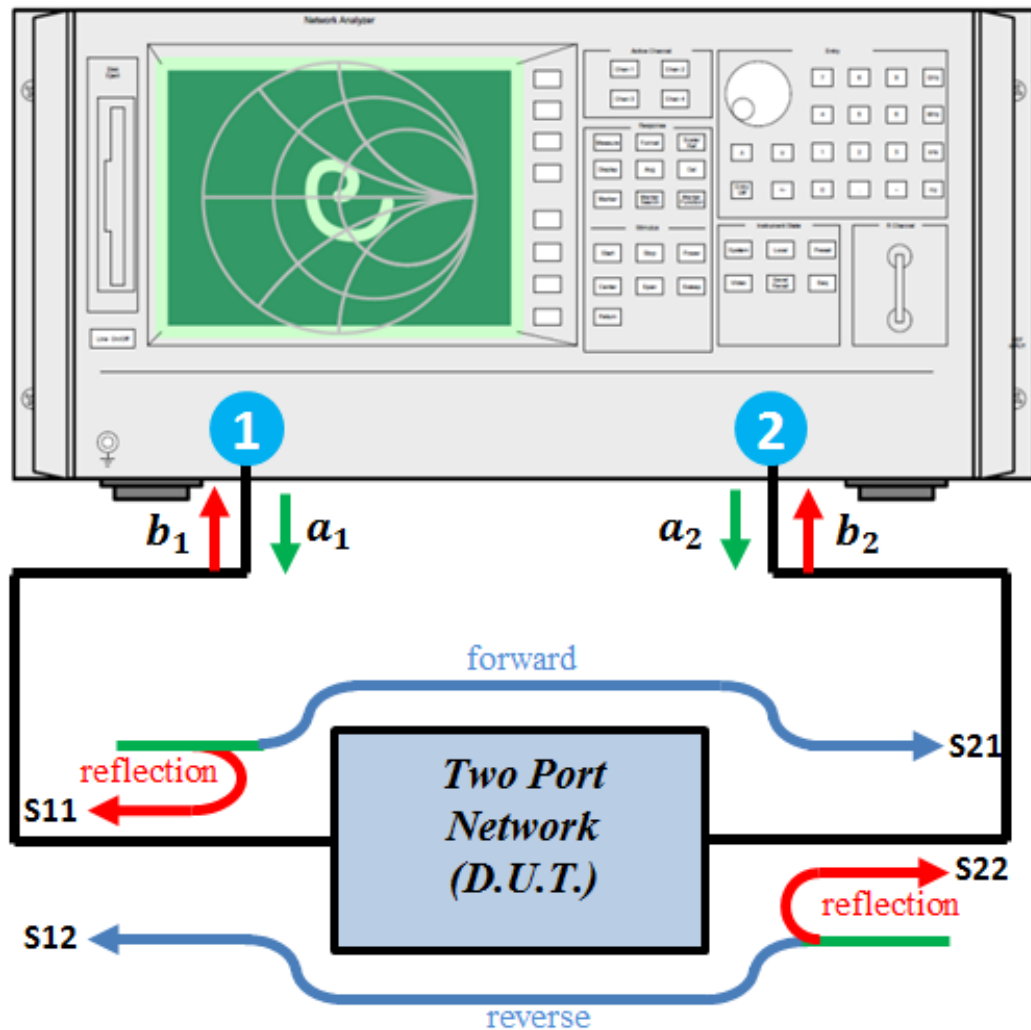


Figure 4.3-7 Illustration of the Vector Network Analyzer (VNA) instrument connected to the device under test (D.U.T). S-Parameters measurements (linear and complex) are obtained.

To measure the full two-port S-parameters of the resonator structure, a Vector Network Analyser (VNA) is employed. Its primary use, illustrated in Figure 4.3-6, is to determine the S-parameters measurement of electrical networks as well to measure its impedance.

The simulation of the TE-like band-gap is confirmed by plotting the electric field magnitude (absolute components) of the forward transmission coefficient (S_{21}) seen in the Figure 4.3-8.

It shows that energy is propagated outside the band-gap in all directions through the lattice, and within the band-gap no energy is propagated.

The band-gap observed between 43 and 56 GHz in the dispersion diagram in Figure 4.3-4 shows good agreement with the full S-parameters and the respective electric field results below.

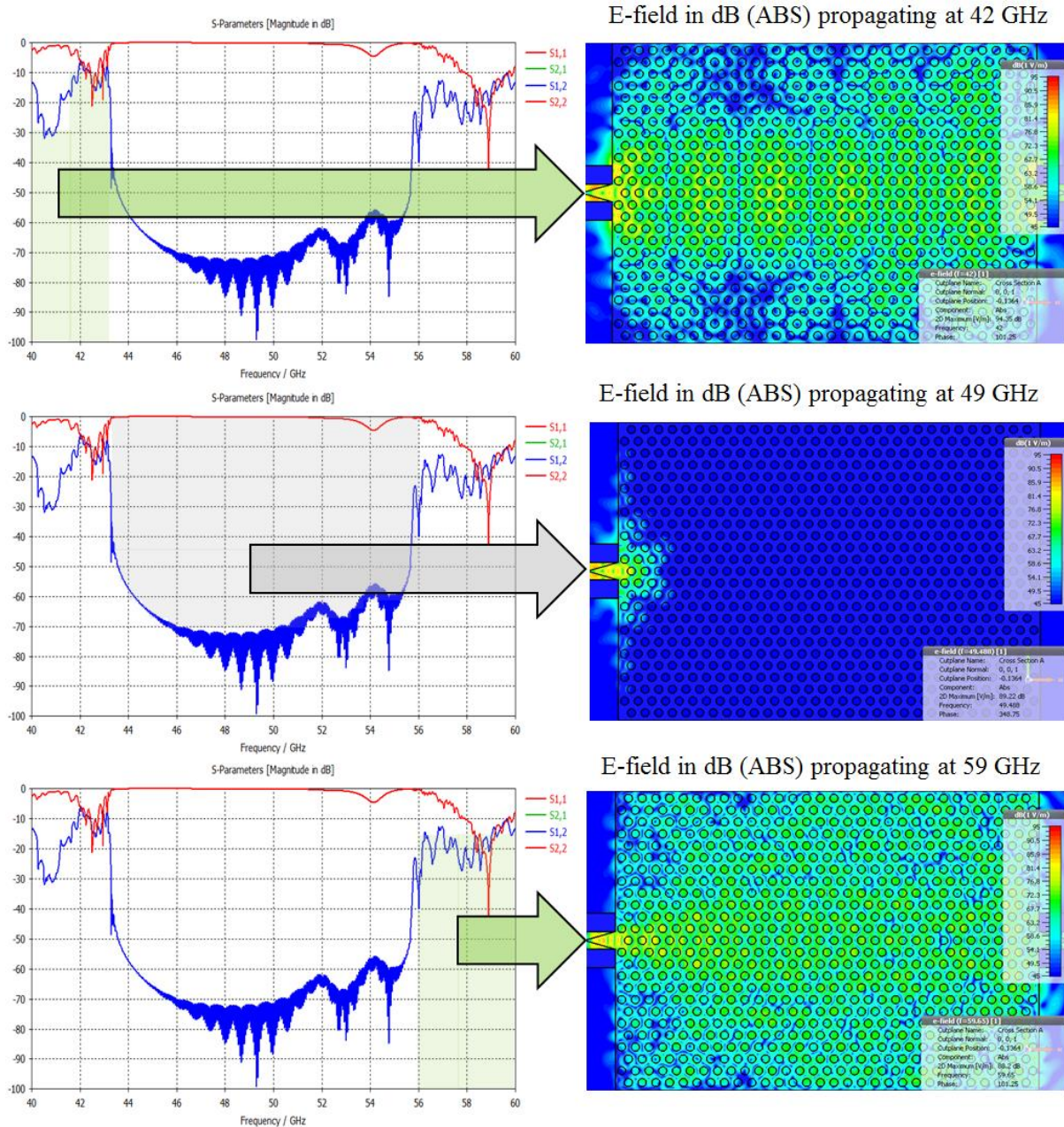


Figure 4.3-8. Simulated full two-port S-parameters from the EBG structure and respective electric-field (absolute component) demonstrating the effect of the band-gap.

4.4. FULL (3D) ELECTROMAGNETIC SIMULATION AND OPTIMIZATION

Photonic crystals are an attracting subject because it has photonic band-gaps (PBG) properties where no propagating electromagnetic mode exists, and when a defect mode is introduced in a photonic crystal, local electromagnetic modes (defect modes) arise within the forbidden band-gap, which acts as a high-Q cavity for such local modes. Since the equations employed in the PBG's are scalable in frequency, the same is applicable to electronic band-gap (EBG) structures working in the microwave and millimetre wave range.

In order to complete the design of the resonator in a two-port configuration, a resonant cavity (line defect) was created in middle of the lattice by omitting three holes. In addition, the three adjacent holes were shifted away from the original lattice positions in order to provide critical

coupling in the cavity therefore maximizing the resonator Q-factor. By introducing the defect in the original lattice, a sharp and narrow bump in the forward transmission coefficient (S_{21}) is observed in the middle of the band-gap. The Q-factor of the cavity is determined by the energy loss per cycle versus energy stored. With no absorption by the metal cavity, the Q-factor is determined by the reflection loss at the interface between the interior and exterior of the cavity.

Two tapers in triangular shape were created in the centre side edges of the silicon resonator to couple TE-like mode to the WR-19 waveguides. Additionally, two defect lines were created from the tapers to guide and couple the energy to and from the resonator cavity. The coupling of energy into the resonant cavity is determined by the offset configuration in each of the three adjacent holes next to the defect as shown in Fig. 4.4-4, therefore confining the energy into the cavity and reducing the out-of-plane radiation losses. The offset position of the adjacent holes were parameterized and after optimised by a template post processing using the frequency domain solver of CST Studio Suite™ simulator in order to maximise the loaded-Q. The taper geometry and its respective length were intentionally dimensioned to match and obtain input and output return loss values aimed at not over couple with the oscillator circuitry. With a relatively weak coupling the Q-factor of the EBG structure is not much disturbed by an external circuit.

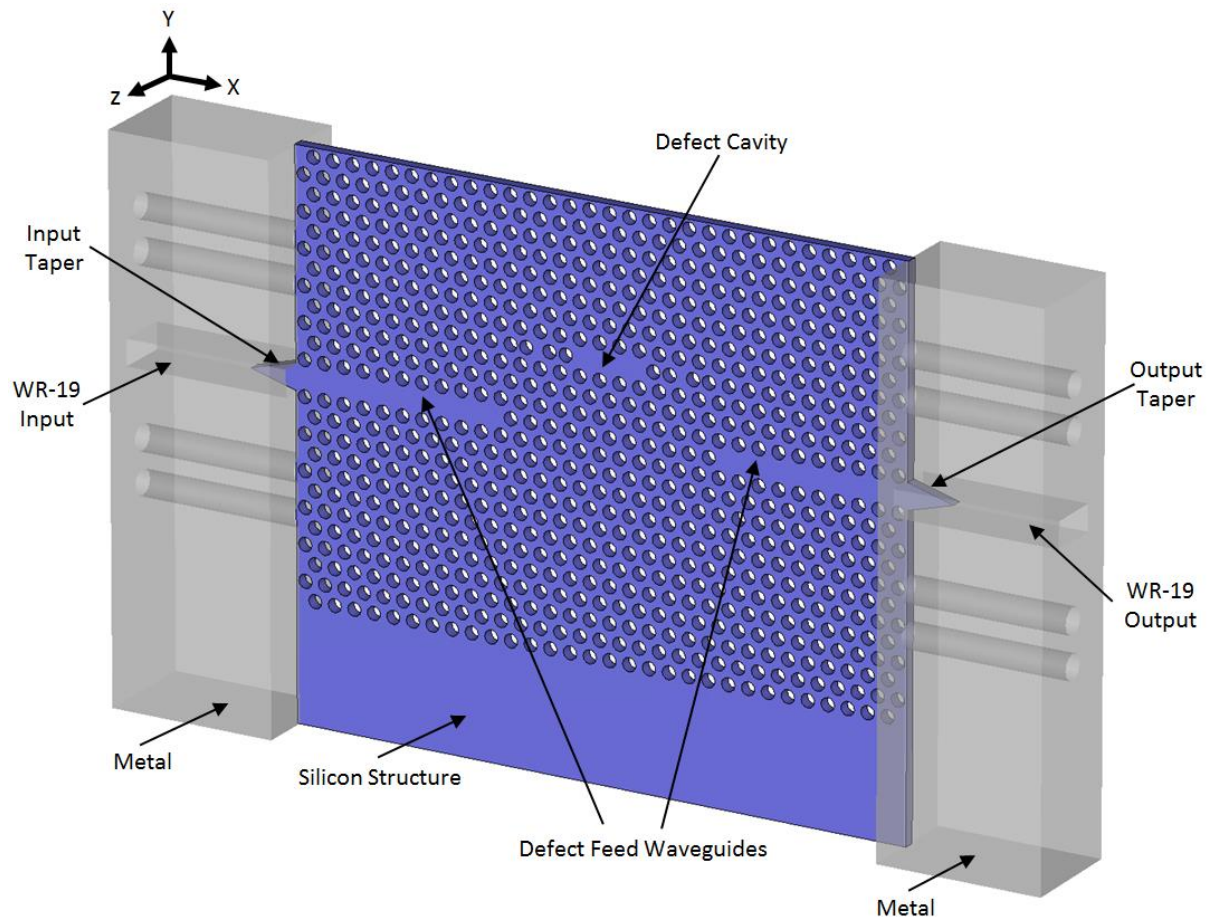


Figure 4.4-1 Aspect of the finished Silicon resonator and its main characteristics mounted in a test-fixture.

The optimisation of the EBG resonator encompasses all parameters calculated previously (see Table 4.3-1) in addition to the design of the defect cavity which is described next.

The number of holes in the X-Y plane should be large enough to suppress the in-plane leakage since the periodicity in the resonator structure produces a band reject effect also known as band-gap where no energy is propagated. The number of necessary lattice constants depends on the bulk crystal properties. The success for the design of the EBG resonator relies on the confinement of the mode inside of the defect cavity by Bragg reflections and reduction of the radiation losses by total internal reflection (TIR) at the substrate-air interface. The key aspects for the realization of the defect cavity are the high-quality factor (Q) and small modal volume (V). The ratio Q/V determines the strength of interactions inside of the cavity. Within this aspect, the space and positioning of the holes next to the cavity are critical to achieve a high Q/V ratio.

The resonant cavity is designed by introducing a defect in the lattice omitting three adjacent holes, so the energy can be confined in-plane within this space. In addition, by gently shifting away the holes surrounding the cavity helps to maximize the Q/V ratio [8]. The displacement of the holes next to the cavity corresponds to a narrowing in the spatial spectral domain. According to Y. Akahane et al. in [8], the electric field inside of the defect cavity can be described as a product of a fundamental sinusoidal wave through a resonant wavelength λ , and an envelope function $F(x)$ determined by the cavity structure.

The intensity of the vertical (z-direction) confinement by the TIR can be established analysing the electric field inside the cavity in plane wave components with several k-vectors by a spatial Fourier transformation. The fundamental wave has a spectrum with peaks at $k=\pm 2\pi/\lambda$ and the envelope modifies the spectrum.

A simplified analysis of the cavity model and the respective electric field profiles distribution and respective Fourier transformation indicating the leaky regions are shown in Figure 4.4-2.

A energy leak from the Silicon structure to the air interface ensues the tangential component of the k-vector ($|k_{\parallel}|$ or $|k_x|$) of each plane wave is confined within the range 0 to $2\pi/\lambda_o$ (where λ_o is the wavelength of the electromagnetic field in the air media. A weak vertical confinement exists in the interface between the cavity and air media). The k-vector $|k_{\parallel}|$ in the air media can assume values ranging from 0 to $2\pi/\lambda$, while in the cavity it can assume a variety of values. When the tangential component $|k_{\parallel}|$ is larger than $2\pi/\lambda_o$, the energy remains strongly confined inside the defect cavity.

Figure 4.4-2 (a) shows a simplified model of the defect cavity with thickness T and length L . The boundaries of adjacent holes represent a perfect mirror in the x-direction confining the energy inside of the cavity.

Figure 4.4-2 (b) shows the electric field inside the defect cavity with a short length 2.5λ , where λ is the resonant wavelength of the signal propagated from the input waveguide in the cavity. Here the envelope function $F(x) = 1$ (for $x = -L/2$ to $+L/2$) and $F(x) = 0$ (for any other value of x).

Figure 4.4-2 (c) shows the spatial Fourier transformation spectra of the electric field seen in Figure 4.4-2 (b) and where the leaky region $|k_{\parallel}|$ is smaller than $2\pi/\lambda_o$. The peaks of the spectrum are located outside of the leaky region in the edge of the cavity which represents large losses.

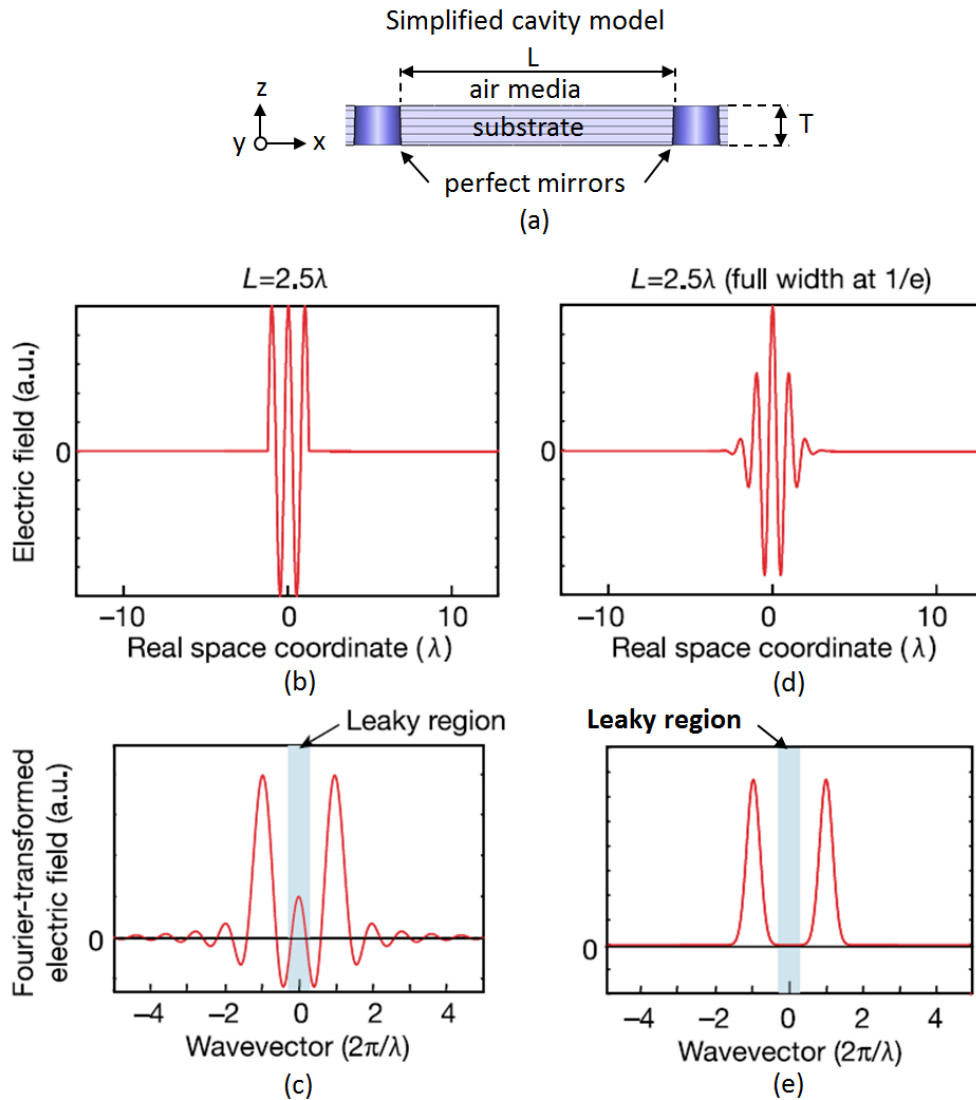


Figure 4.4-2 (a) The simplified cavity model with thickness T and length L , in (b) the electric field distribution inside the cavity and (c) its respective spatial Fourier transformer spectra with short length of 2.5λ . In (d) the electric field distribution with a gentle envelope function and its spatial Fourier transformer spectra in (e). The leaky region is shown in blue color.

In order to confine a large amount of energy inside of the cavity, the spatial variation of the envelope function at the cavity edges shall be gently accommodated, so that its Fourier transformation spectrum does not have peaks in the leaky region as shown in Figure 4.4.-2 (d) and (e).

Once the behaviour over the distribution of electric field in the cavity and air interface media are known, the strategy is to configure the simulation tool to gently displace the holes adjacent to the cavity in order to obtain a spectra result with peaks outside the leaky region and close as possible to the spectra seen in Figure 4.4.-2 (e). This can be achieved indirectly through an optimization process targeting to obtain the highest Q-factor as possible.

The optimisation process of the EBG resonator is performed through the frequency domain solver of CST Studio Suite™.

First, a set of parameters in the geometry of the resonator and respective test-fixture were created. Each parameter obeys a specific range of values that are aimed to be swept individually

or in combination. The purpose is to parameterise one or more parameters by a sweep analysis in order to obtain the desired results. This aims to minimise the amount of parameters to be set in the optimisation process otherwise a huge computational effort will be needed with a risk of not obtaining convergence. The degree of freedom given to each parameter is also used to escalate the properties of the resonator, in this case the band-gap and resonant frequency as well the losses.

Once the parameterisation is completed, the optimisation process can be carried out. The objective is to work on a reduced set of parameters responsible for achieving the target specified for the goal, in this case the unloaded Q-factor.

Table 4.4-1 below retracts all parameters investigated in the parameterisation and optimisation processes.

Name	Expression	Value	Description	Type
clearanceX	= 0.45	0.45	Clearance distance (in X direction) from substrate wall	Length
clearanceY	= .4	.4	Clearance distance (in Y direction) from substrate wall	Length
delta1	= 0.38394782946312	0.38394782946312	Displacement (C1), tuning	Length
delta2	= 0.047267682109558	0.047267682109558	Displacement (C2), tuning	Length
delta3	= delta1	0.38394782946312	Displacement (C3=C1), tuning	Length
DeltaF	= 50	50	Delta frequency	Frequency
F0	= 44.74	44.74	Resonant frequency	Frequency
Fmax	= 50	50	Maximum stop frequency	Frequency
Fmin	= 40	40	Minimum start frequency	Frequency
freeSpaceImpedance	= 376.73031346177	376.73031346177	Free space impedance (Zo)	None
lattice	= 1.831	1.831	Substrate lattice constant (a)	Length
Lx	= 4.6	4.6	Substrate taper length	Length
Ly	= 2.37	2.37	Substrate taper width	Length
Nx	= 31	31	Number of holes (in X direction)	None
Ny	= 12	12	Number of holes (in Y direction)	None
radius	= .3*lattice	0.5493	Hole radius (r)	Length
spaceZ	= 1	1	Test-fixture excess dimension (in Z direction)	Length
spaceY	= 2	2	Test-fixture excess dimension (in Y direction)	Length
thickness	= 1	1	Substrate tickness (h)	Length
WGa	= 4.775	4.775	Test-fixture waveguide dimension (a)	Length
WGb	= 2.388	2.388	Test-fixture waveguide dimension (b)	Length
WGL	= 10	10	Test-fixture waveguide dimension (l)	Length

Table. 4.4-1 Parameter list of all variables included in the parameterization and optimization processes.

The adjustable parameters displayed in Table 4.4-1 and Figure 4.4-2 used in the parameterization and optimization processes are described as follows:

1) clearanceX

The clearance distance from the edge of the holes to the walls of the substrate in the X-axis direction. The optimum value found is 0.45 mm. This parameter contributes to minimize the reflections at the interface substrate-metal.

2) clearanceY

The clearance distance from the edge of the holes to the walls of the substrate in the Y-axis direction. The optimum value found is 0.40 mm. This parameter also contributes to minimize the reflections at the interface substrate-metal.

3) delta1

The displacement of the first two holes in the X-axis direction next to the defect cavity responsible to confine the in-plane energy into its physical space. Together with delta2, both are the only parameters to be optimized in order to obtain the goal Q-factor as set in the target (>10,000). The best value found is 0.383 mm away from its original position in the lattice.

4) delta2

The displacement of the second two holes in the X-axis direction next to the defect cavity responsible to confine the in-plane energy into its physical space. Together with delta1, both are the only parameters to be optimized in order to obtain the goal Q-factor as set in the target (>10,000). The best value found is 0.047 mm away from its original position in the lattice.

5) delta3

Same as delta1.

6) DeltaF

It is the frequency range determined in the frequency domain solver. Parameter fixed to 50 during the optimisation process. There is a dependency related to the center frequency (F0), meaning the range is in fact is determined by the lower (F0-DeltaF/2) and upper (F0+DeltaF/2) frequencies, otherwise, the frequency range can be determined by the parameters Fmax and Fmin which overrides DeltaF.

7) F0

It is the intended center frequency (resonance peak) determined in the frequency domain solver. Parameter fixed to 44.74 GHz during the optimisation process. There is a dependency related to the delta frequency (DeltaF).

8) Fmax

It is the maximum stop frequency established in the simulation environment. Parameter fixed to 50 GHz during the optimization process, otherwise, the frequency range can be determined by the parameter Delta F which overrides Fmax.

9) Fmin

It is the minimum start frequency established in the simulation environment. This parameter is adjustable and it was fixed to 40 GHz during the optimization process, otherwise, the frequency range can be determined by the parameter Delta F which overrides Fmin.

10) freeSpaceImpedance

A physical constant relating to the magnitudes of the electric and magnetic fields of the electromagnetic wave travelling through free space. It has an exactly define value as 376.7303134617 Ω . A thin sheet tabulated impedance of free impedance material is defined to guarantee stability within the frequency domain solver.

11) lattice

The lattice constant of holes within the substrate structure. This parameter is mainly responsible to produce the band reject effect also known as band-gap where no energy is propagated. Previously calculated as 1.831 mm, it remains fixed during the optimization process.

12) L_x

The substrate taper length. During the parameterization, this parameter was found optimum as 4.6 mm in order to create a good compromise with the input and output return loss. This parameter remains fixed during the optimisation process.

13) L_y

The substrate taper width. This parameter was set and fixed 2.37 mm in order to fit in the test-fixture waveguide cross section (a) dimension. This parameter remains fixed during the optimisation process.

14) N_x

The total number of holes within the lattice in the X-axis direction. The number of holes should be large enough to suppress the in-plane leakage since the periodicity in the resonator structure produces a band reject effect also known as band-gap where no energy is propagated. This parameter was set to 31 during the optimisation process.

15) N_y

The total number of holes within the lattice in the Y-axis direction. The number of holes shall be large enough to suppress the in-plane leakage since the periodicity in the resonator structure produces a band reject effect also known as band-gap where no energy is propagated. This parameter remains fixed as 12 during the optimisation process.

16) radius

It is the radius dimension of the holes in the lattice. This value was calculated previously as being 0.3 times the lattice constant for optimum value and must remain fixed as 0.5493 mm during the optimization process

17) spaceZ

It is the excess height of the test-fixture structure in the Z-axis direction fixed to 1. This parameter is responsible to keep an open space distance from the substrate slab to the boundary conditions in the Z-axis direction.

18) spaceY

It is the excess length of the test-fixture in the Y-axis direction fixed to 2. This parameter is adjustable and was set to intercept the same end coordinates of the clearanceY parameter. This parameter also determines the boundary conditions in Y-axis in the simulation environment.

19) thickness

It is the thickness of the Silicon substrate. This parameter remains fixed to 1 mm during the optimization process.

20) WGa

The internal wall dimension of the waveguide (cross section a), of the waveguide compatible with the WR-19 (EIA standard) to guarantee the operation of signal between 40 and 60 GHz. This dimension shall be large enough to fit one complete wavelength of the signal. This parameter remains fixed to 4.775 mm during the optimization process.

21) WGb

The internal wall dimension (b) of the waveguide cross section compatible with the WR-19 (EIA standard) to guarantee the operation of the signal between 40 and 60 GHz. This parameter remains fixed to 2.388 mm during the optimization process.

22) WGL

The width of the test-fixture structure in the X-axis direction. This parameter is adjustable and was set to keep a minimum length of the waveguide as it shall be greater than the cut-off wavelength of the dominant mode. It also determinates the boundary conditions in X-axis in the simulation environment. This parameter remains fixed to 10 mm during the optimization process.

A template based post-processing was created with the necessary result expressions used to derive the goal, unloaded Q-factor. The results name and respective description are depicted in Table 4.4-2 as well described as follows:

- 1) S_{21} is the maximum value of S_{21} at the resonance (in magnitude)
- 2) F_0 is the frequency at resonance (in GHz)
- 3) B_{3dB} is the bandwidth at the -3 dB points from the resonance (in GHz)
- 4) Q_L is the loaded Q-factor (unit less)
- 5) Q_0 is the unloaded Q-factor (unit less)
- 6) S-Parameter $S_{1,1}$ is the input voltage reflection coefficient (in magnitude)
- 7) S-Parameters $S_{2,1}$ is the forward voltage gain (in magnitude)

The parameters above were defined in the template based post-processing in order to calculate the unloaded Q-factor of the resonator structure.

Result name	Type	Template name	Value
1 So	0D	0D or 1D Result from 1D Result (Rescale, Derivation, etc)	0.369152471
2 Fo	0D	0D or 1D Result from 1D Result (Rescale, Derivation, etc)	44.74665
3 B3dB	0D	0D or 1D Result from 1D Result (Rescale, Derivation, etc)	0.009050928494
4 QL	0D	Mix Template Results	4943.873994
5 Go	0D	Mix Template Results	7836.876212
6 S-Parameters-S1,1	1DC	Load 1D Data File (project and external)	
7 S-Parameters-S2,1	1DC	Load 1D Data File (project and external)	

Table 4.4-2 Template based post-processing containing the expressions to derive the Q-factor.

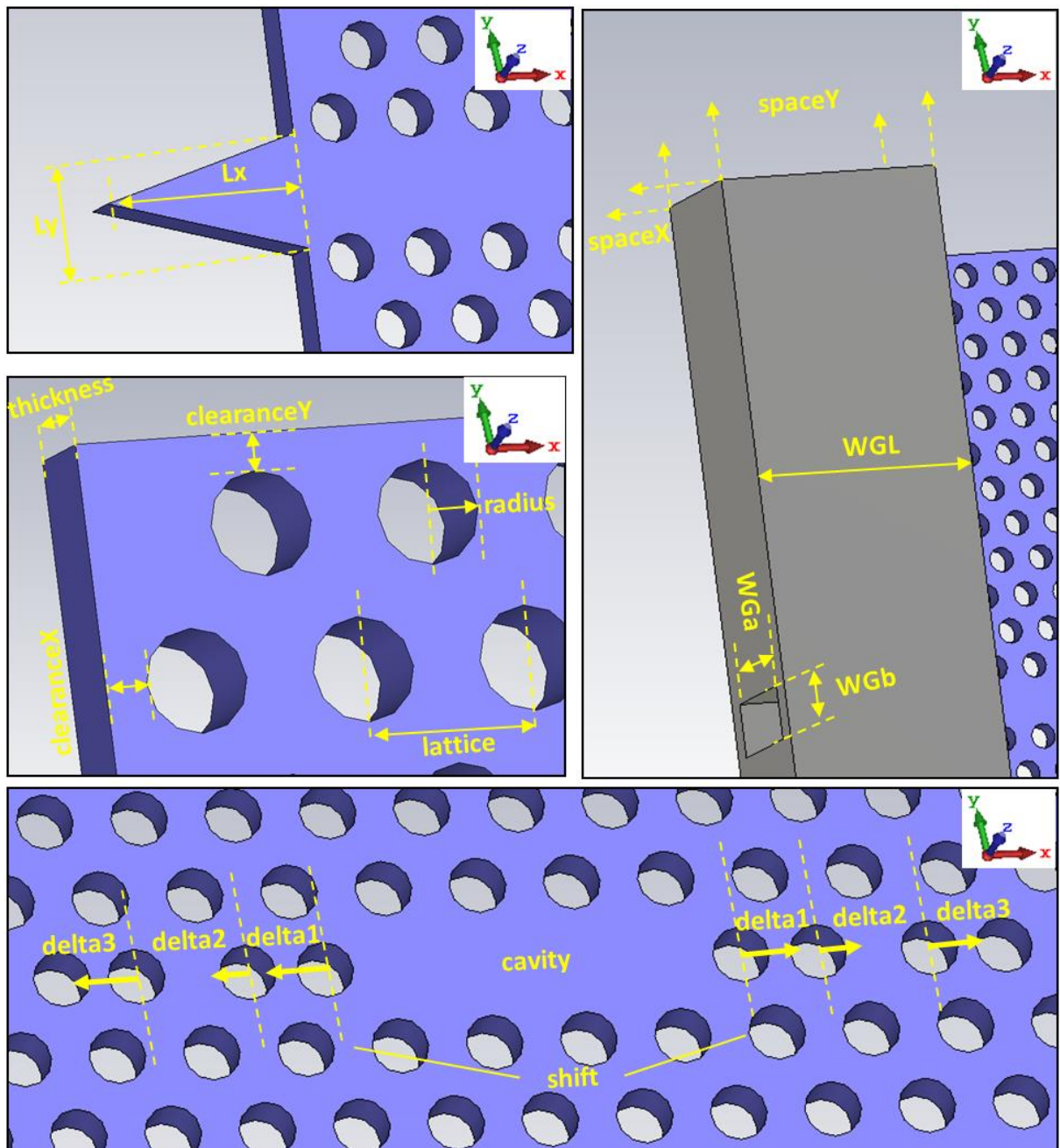


Figure 4.4-3. All adjustable parameters used in the parameterization and optimization processes

Table 4.4-3 shows the Goal tab in the optimizer window of the frequency domain solver, CST Studio Suite™. The Q_0 derived from the template post-processing parameters is then set with target higher than 10,000. By choosing the Trust Region Framework algorithm, the simulator will give the best combination results for the maximum achievable unloaded Q-factor.

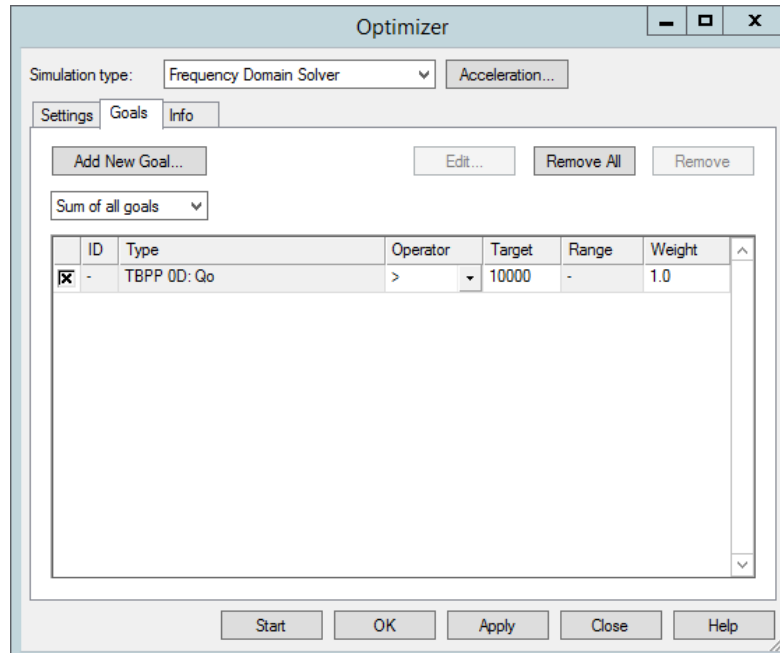


Table 4.4-3 The Goal tab in the optimizer of the frequency domain solver showing the unloaded Q-factor set with a target higher than 10,000.

As result, in a total of 10 evaluations runs, the run ID (identity) number 6 achieved the best parameter for the maximum achievable unloaded Q-factor, therefore the parameters delta1 and delta2 were found best as 0.3839 and 0.0472 respectively.

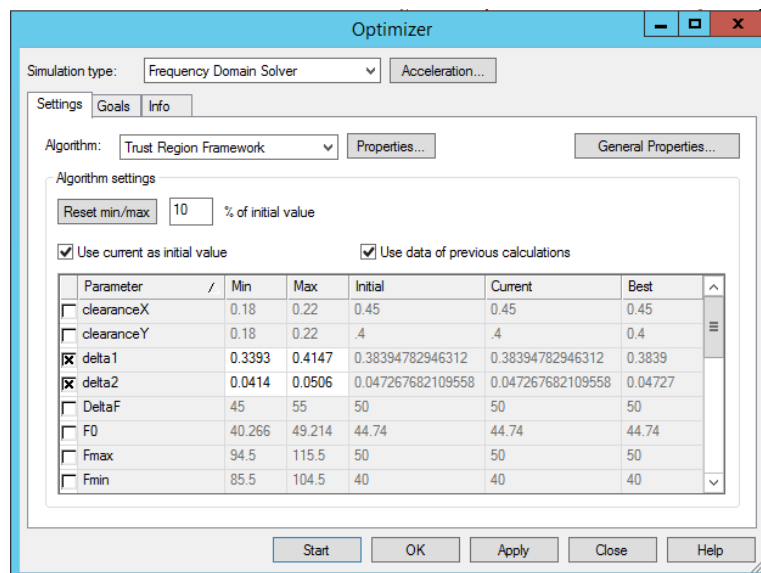


Table 4.4-4 The Info tab in the optimizer of the frequency domain solver showing the best values of delta1 and delta 2 parameters for the best achieved unloaded Q-factor.

The Figure 4.4-4 shows the displacement of the three first holes from its original positions next to the cavity in the x-direction and the respective best achieved results in millimetre for the parameters delta1 and delta2. Once the optimization process has finished a time and frequency domain simulations were run in order to compare the results. Within this configuration, Figure 4.4-5 shows the achieved loaded Q-factors of the resonator structure as 5579 using the frequency domain solver and 4478 using the time domain solver.

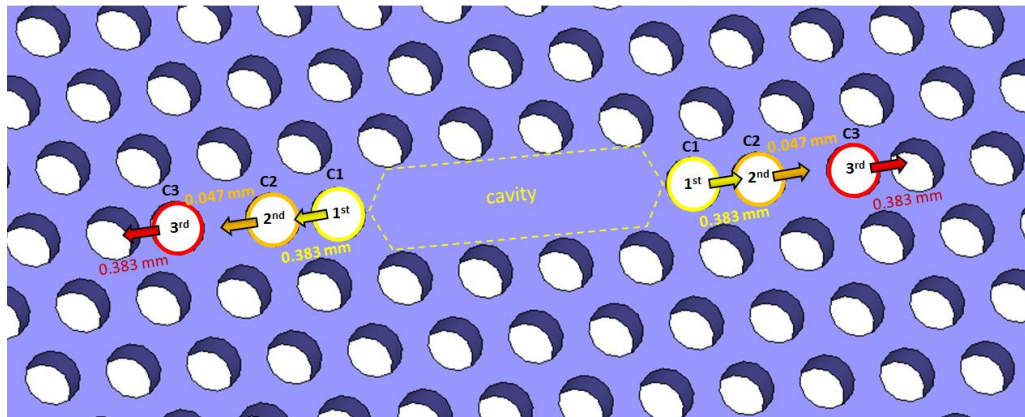


Figure 4.4-4 The detail of the defect cavity and adjacent holes and their respective displacement (in tandem) for the best achieved unloaded Q-factor.

The values are comparable, however for this type of structure possessing very high Q-factor, the frequency domains is more efficient if compared to time domain solver as the energy within the structure takes a very long time to decay, which means the simulation has to be run for a very long time to get reliable results with a low threshold of accuracy, usually from -50 to -60 dB and increased number of pulses, higher than 100. A truncation error in the simulation results may be observed in case the energy decay criteria is not satisfied; either because the energy level was not set sufficient low in face of this type of structure possessing high Q-factor or the number of pulses had been completed before the energy decays to the desired set level.

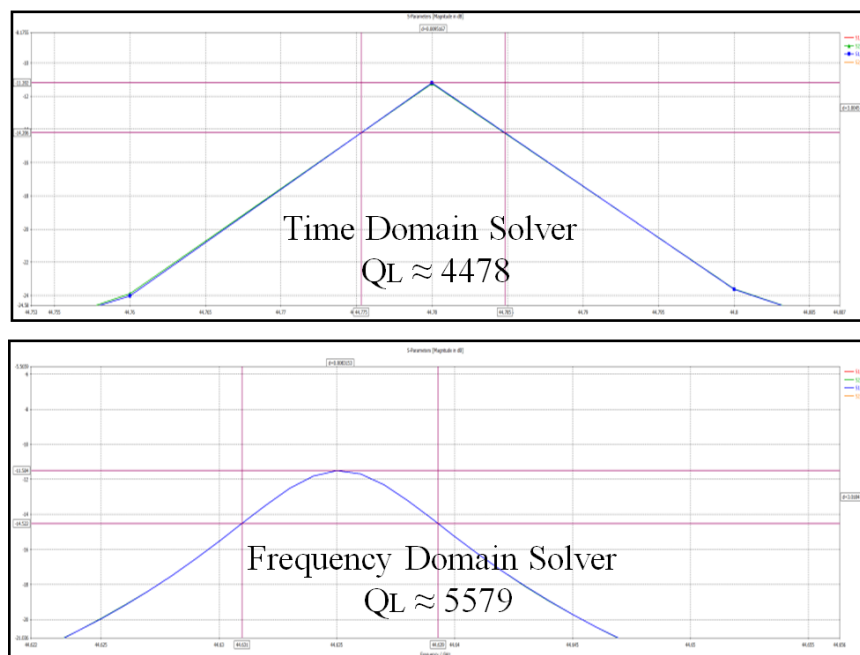


Figure 4.4-5 The obtained loaded Q-factors through the time and frequency solvers of the simulation tool.

After an initial assessment of transmission coefficient (S_{21}) through a full two port S-parameter analysis of the resonator structure connected via waveguide; a parameterisation and optimisation of the adjacent holes were performed aiming to maximise the loaded Q-factor of the resonant circuit. The full two port S-parameter results are shown in Figure 4.4-5 using the time domain solver of CST Studio Suite™. The results were checked also with the frequency domain solver and are comparable.

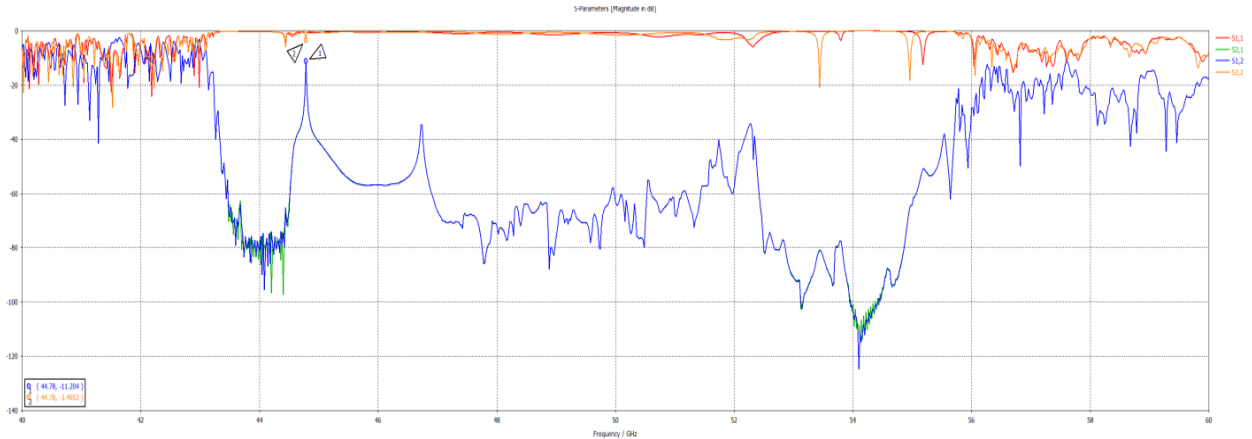


Figure 4.4-5 Full two-port S-parameter simulation from the resonator structure and its test-fixture, time domain solver.

The electric field magnitude (ABS component) in the resonator structure when the defect cavity is at resonance is shown in the Figure 4.4-6. It clearly depicts how the energy is coupled through the cavity from the input to the output waveguides. The concentration of electric field is noted in the area of the defect cavity achieving a peak value of 101.4 dB (V/m). In Figure 4.4-6, the test-fixture layer is hidden to facilitate the view.

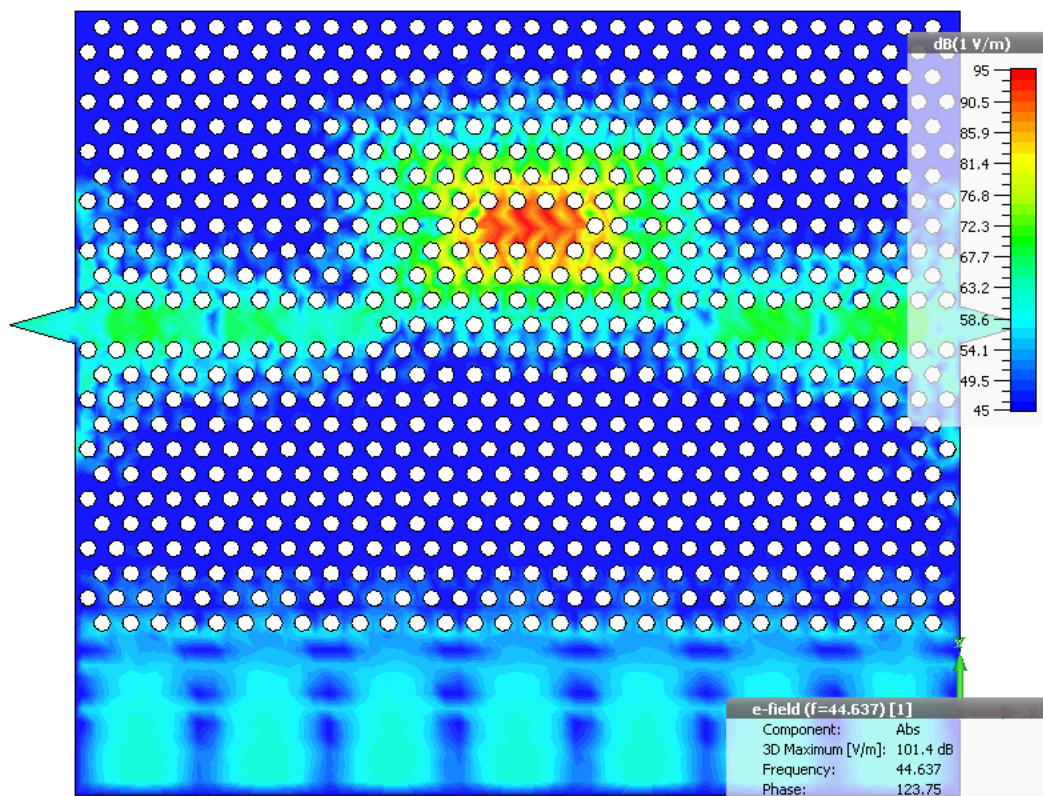


Figure 4.4-6 E-field magnitude (ABS component) plot showing the defect cavity at resonance.

The 3D view in perspective of the resonator structure is shown in Figure 4.4-7. The E-field on plane in the electromagnetic simulator was activated in order to display the propagation of the energy also in the z-axis direction. A strong vertical confinement of the E-field can be seen in the area above the cavity. Also a leaky region is seen in the center of the cavity where radiation loss occurs. In Figure 4.4-7, the test-fixturing layer is hidden to facilitate the view.

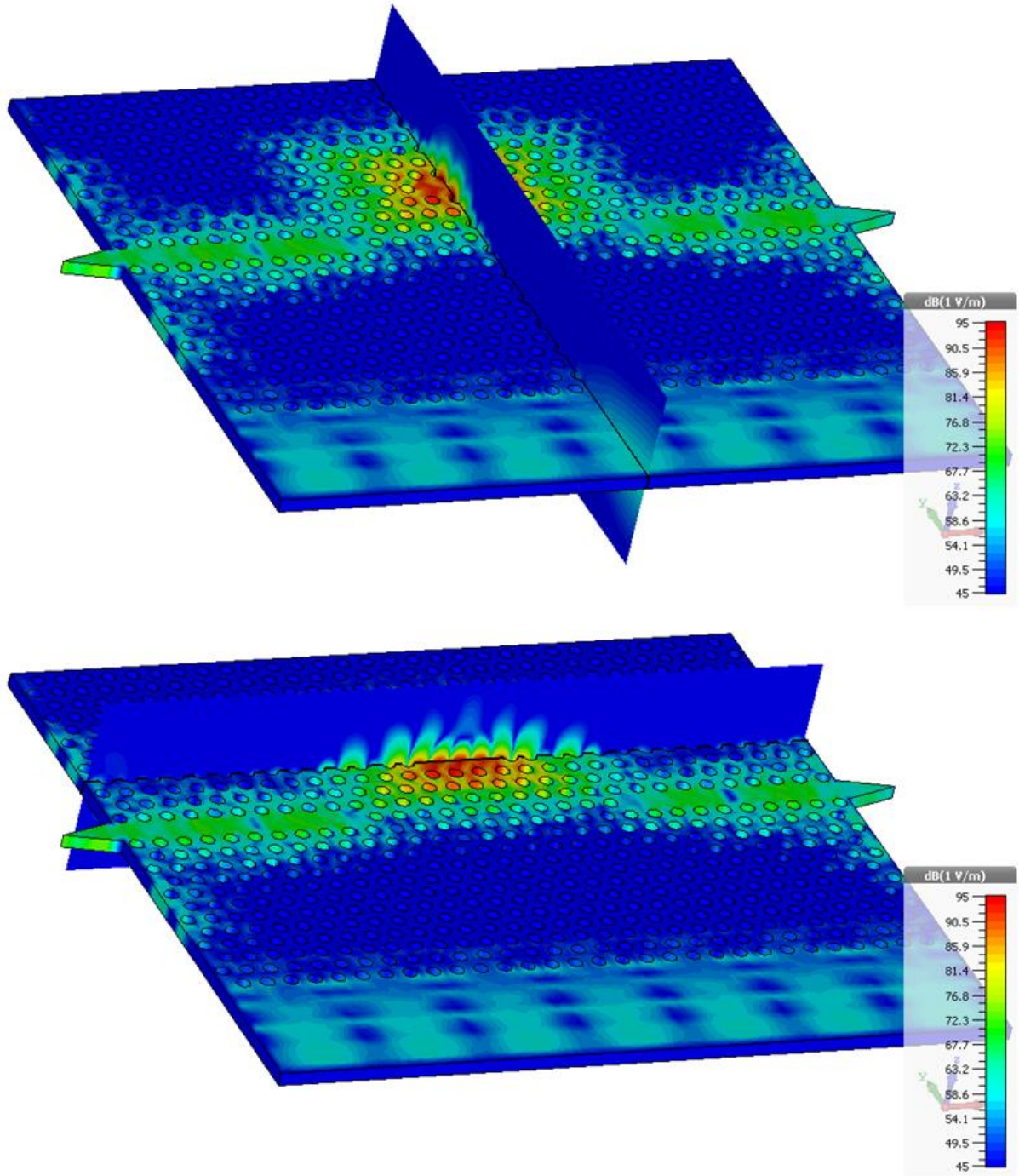


Figure 4.4-7 E-field magnitude (ABS component) plot in 3D view at cross section planes showing the defect cavity at resonance.

The 3D view in perspective of the resonator structure is shown in Figure 4.4-8. The H-field on plane in the electromagnetic simulator was activated in order to display the propagation of the energy also in the z-axis direction. In Figure 4.4-8, the test-fixture layer is hidden to facilitate the view.

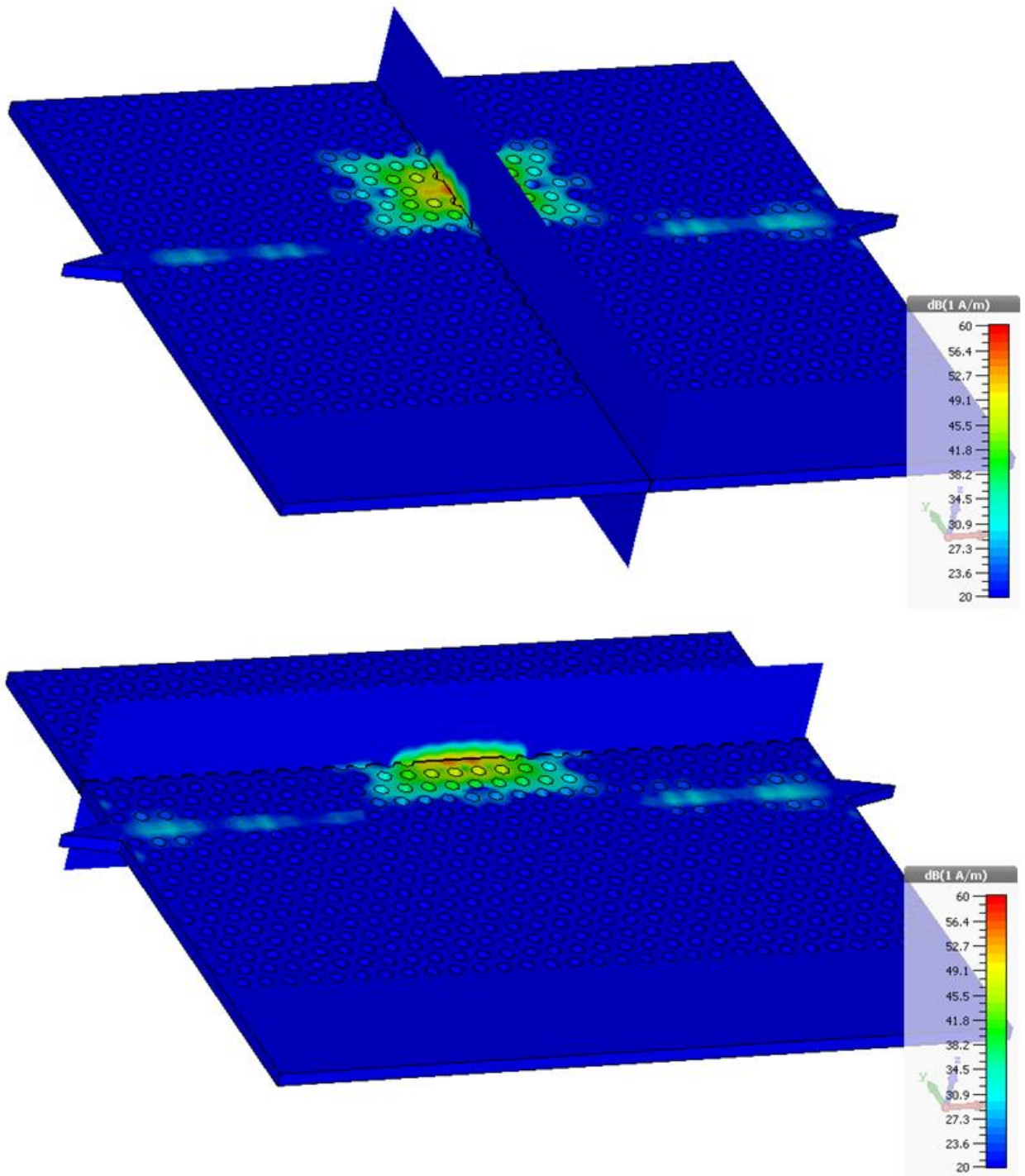


Figure 4.4-8 H-field magnitude (ABS component) plot in 3D view at cross section planes showing the defect cavity at resonance.

4.5. PROTOTYPE FABRICATION AND MEASUREMENTS

The resonator has been manufactured at the Public University of Navarra (UPNA) Clean Room facilities. A high resistivity ($>10.000 \Omega\text{cm}$), $\langle 1-0-0 \rangle$ plane oriented, 1mm thick, 4" silicon wafer has been dry etched through using a standard three-step Deep reactive-ion etching (DRIE) Bosch Process.

Deep reactive-ion etching (DRIE) is a process used to create deep penetration, steep-sided holes and ditches in wafers/substrates, typically with high aspect ratios. It was developed for microelectromechanical systems (MEMS), which require these features, but is also used to excavate ditches in silicon wafers for creating through-silicon via-holes (TSV) in advanced wafer technology.

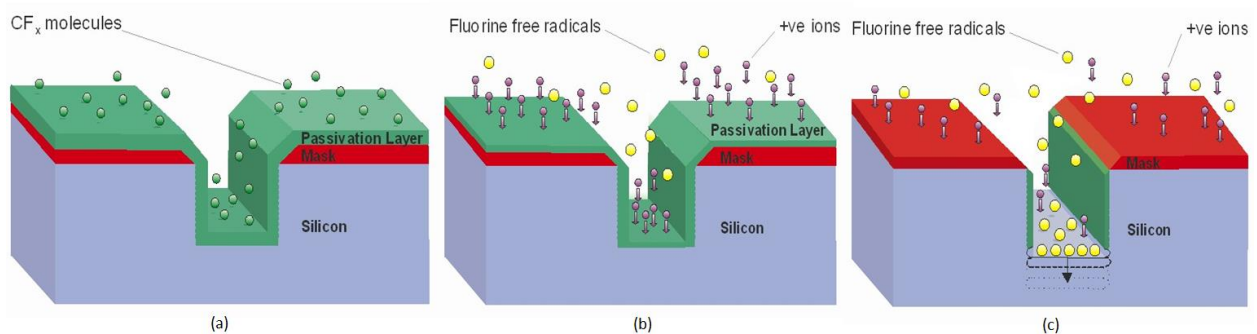


Figure 4.5-1 Schematic of DRIE Process (a) C_4F_8 plasma deposits passivating polymer on all surfaces (b) positive ions in SF_6 plasma bombard horizontal surfaces removing polymer (c) Fluorine free radicals in SF_6 plasma etch exposed silicon at the base of the feature, with the vertical sidewall protected by the polymer. Steps (a) to (c) are repeated on multiple cycles.

Etching a 1mm thick silicon wafer is a challenging process due to the need of a mask that can hold the entire etch, and at the same time the wafer needs to be glued to a dummy carrier that protects the table but ensures enough cooling and no interaction with the process gases. A chromium hard mask has been used since it has much higher selectivity compared to other more commonly used hard masks, such as silicon oxide, or photoresist soft masks.

The authors in [5] reported a chromium selectivity higher than 3000:1 over silicon, whereas the usual value for SiO_2 selectivity is around 150:1, that strongly depends on the tool and process being used. This allowed to etch through the 1mm thick silicon wafer with a mask thickness below 500 nm. The drawback of using such mask is that chromium cannot create volatile compounds in SF_6 plasma, therefore any sputtered atom from the mask could be redeposited on the sample and create a micro-mask that grows a micro pillar in the device wall. Fig 4.5-3 a) shows the wafer with the lift-off patterned Cr mask.

UPNA microwave, millimetre and sub-millimetre-wave counts with laboratories fully equipped with Vector Network Analyser and Spectrometers up to 1 THz, with antenna measurement capabilities in far field and near field ranges. Clean room facilities for fabrication of millimetre-wave and sub-millimetre-wave components, including all necessary equipment for photolithography fabrication and a plasma ICP DRIE etching system for 200-500 GHz waveguide components fabrication.



Figure 4.5-2 DRIE etching system: Oxford Instruments Plasma Pro NGP80ICP65 for Deep Etching.

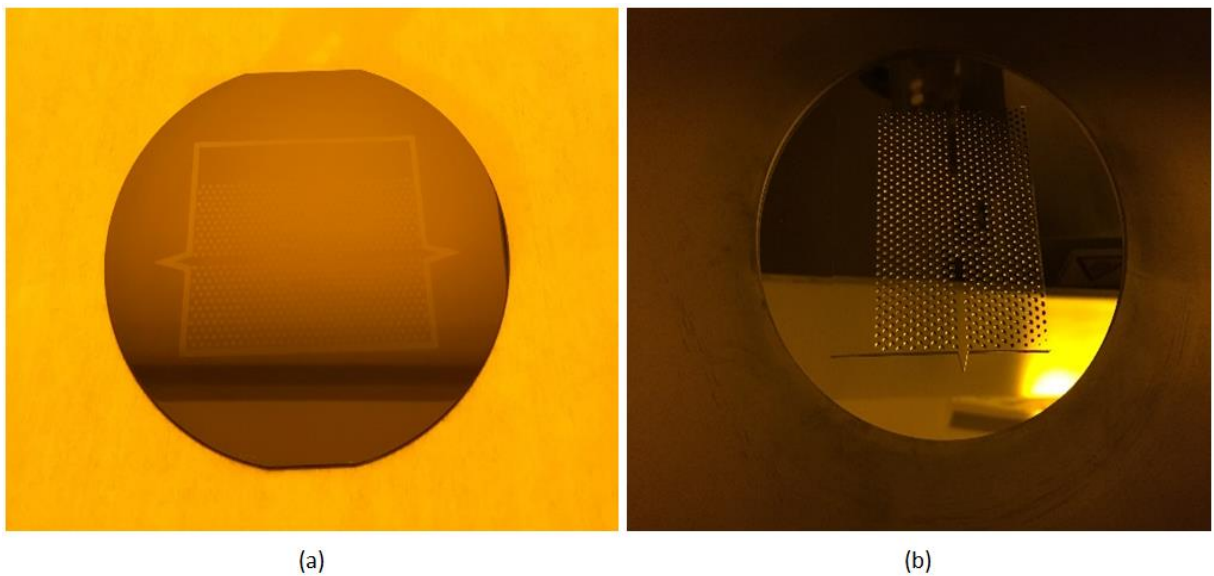


Figure 4.5-3 a) Si wafer with patterned Chromium mask, and b) Si wafer after the etching process.

The wafer was then mounted on a carrier wafer using a thin photoresist layer (around $2\ \mu\text{m}$) that ensures process compatibility and a proper cooling of the wafer during the exothermic silicon etching. After the etching was done, the resonator was detached from the carrier wafer and the remaining Cr mask was wet etched. Fig. 4.5-3 b) shows the device after an O_2 plasma cleaning to remove any residuals from the process.

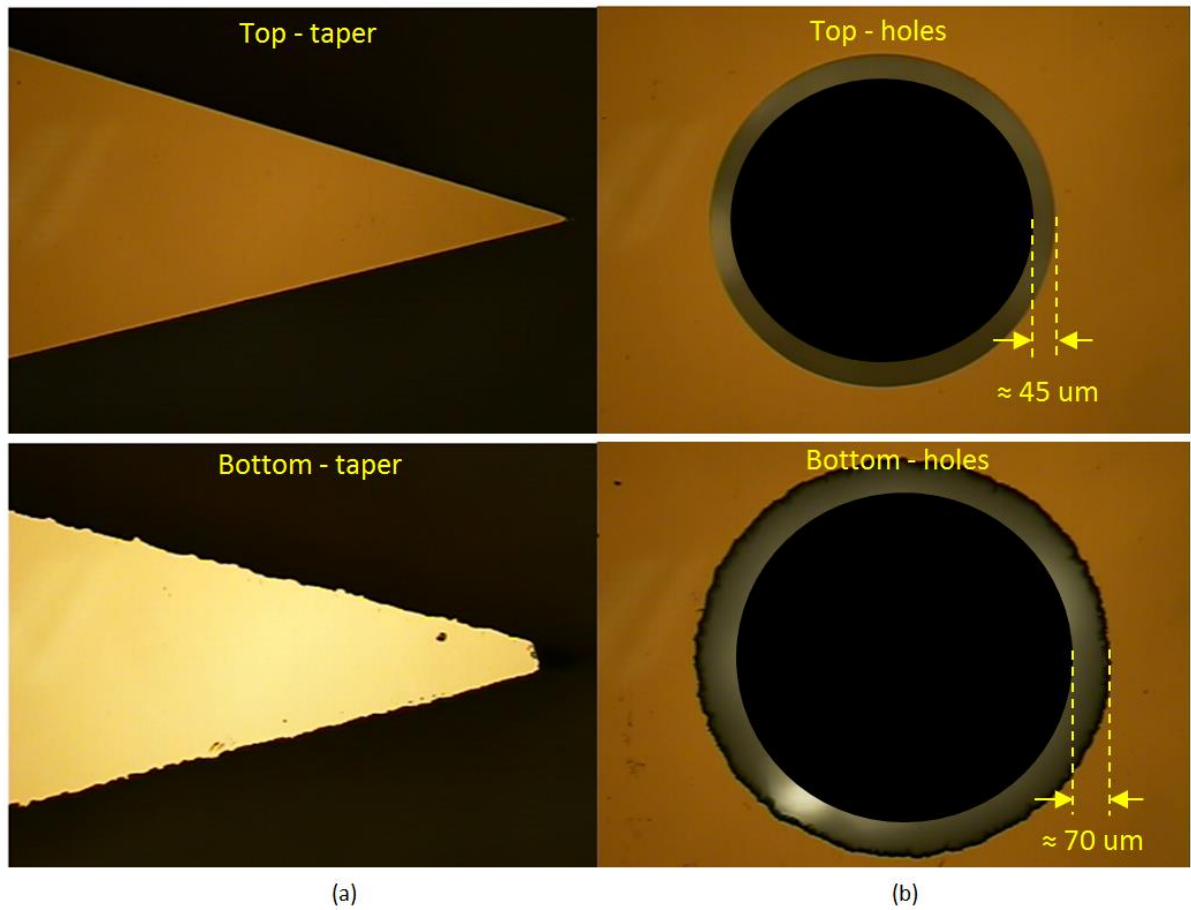


Figure 4.5-4 Effects of the etching in the silicon resonator, a) rounded taper, b) top and bottom holes sizes.

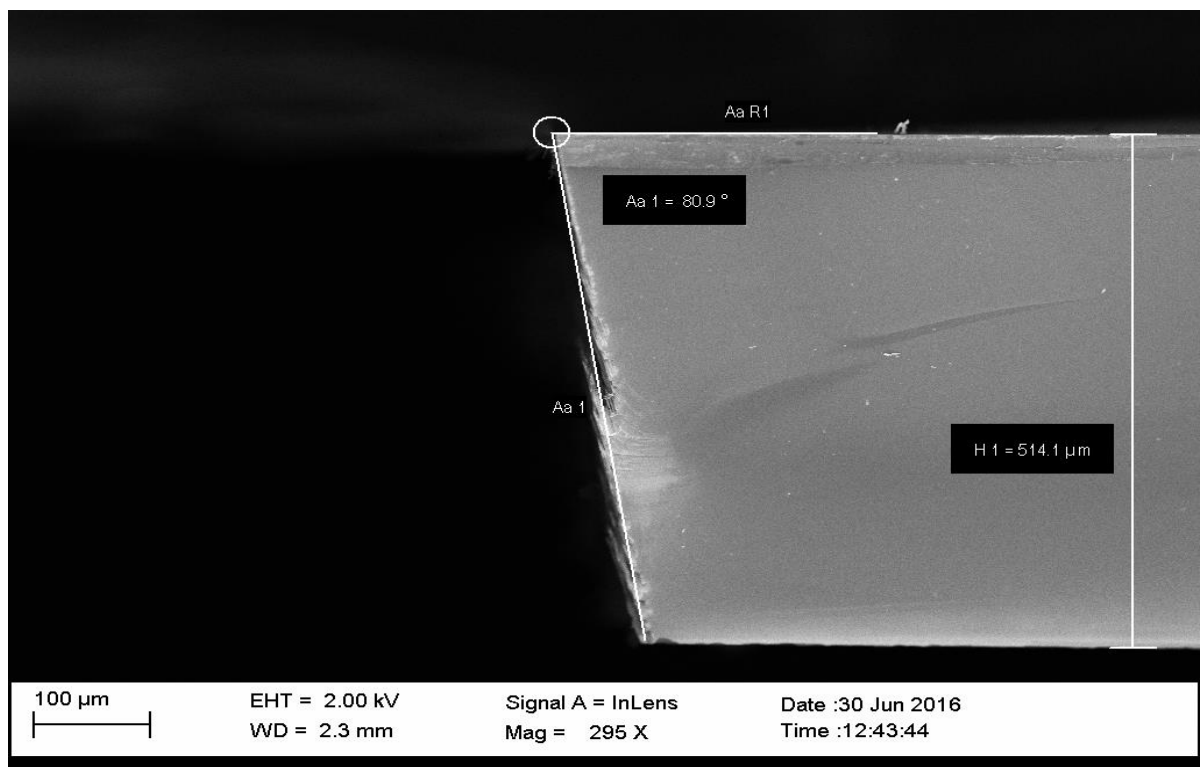


Figure. 4.5-5 Effects of the etching in the silicon resonator, side walls.

The etching process in both top and bottom sides of silicon resonator resulted in the periodical holes with a conical shape. Microscopic images are displayed in Figure 4.5-4 and Figure 4.5-5 showing the effects of the etching process in the Silicon resonator.

The Figure 4.5-4 a) shows the effects of etching process on the rounded taper and b) where the top side diameter increased in 45 μm while the bottom 70 μm in diameter from the original structure. Figure 4.5-5 shows the angle of side wall were also affect and where reduced from 90° to 83.70°.

4.6. INTRODUCTION OF ETCHING EFFECTS

The introduction of the etching effects in the original Silicon structure which has been previously optimised in the simulation environment affected the main targets compromising the expected results. The main parameters such as the resonance peak were shifted upwards in frequency and the quality factor was considerably compromised lowering its value. Those effects are mainly due to the fact the key parameters in the optimisation process rely in the design of the defect cavity, where the defect introduced (displacement between the adjacent holes) is critical in terms of coupling confining in-plane Bragg reflections. A plane-wave of the field components inside of the cavity (displacement of holes c_1 , c_2 and c_3) corresponds to a narrowing in the spatial spectral domain, reducing the components in the in-plane wave-vector k_{\parallel} that do not satisfy the condition for the total internal reflection contributing to the radiation loss in the resonator design.

In order to validate the experiment comparing the measured results of the final prototype with the ones obtained from the simulated structure, it was necessary to re-introduce the etching effects observed into the simulation environment.

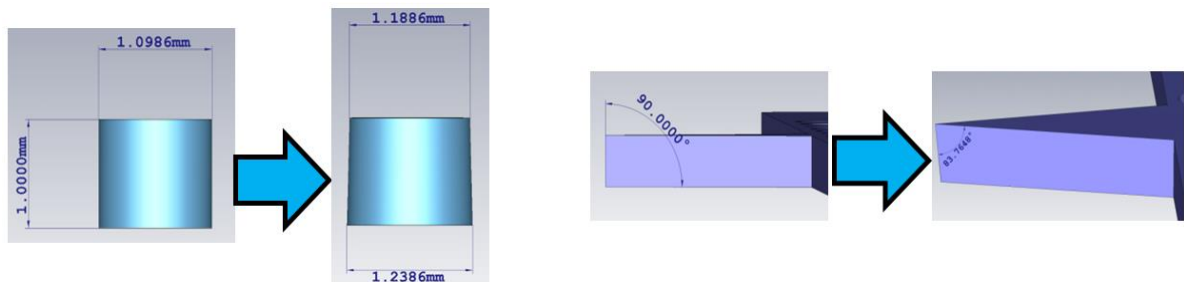


Figure 4.6-1 The effects of etching process re-introduced into the simulation environment.

The observed modifications (side walls, rounded tip tapers, top and bottom holes sizes) were re-introduced under the simulation environment and shown in Figure 4.6-1 and the full two-port S-parameters were obtained again.

The results show a shift of 1.174 GHz upwards in frequency with respect to the original and optimized simulation and a reduction in a factor of 1772 in the loaded Q-factor. In conclusion, the loaded Q-factor previously optimized by parameterizing the offset between the adjacent holes was considerably compromised and degraded due to effects introduced in the etching process. It is worth to comment the etching effects could be minimized if a more accurate and precise method is introduced however at higher manufacturing costs.

4.7. CORRELATION OF RESULTS (MEASUREMENT VERSUS SIMULATION)

The full two-port S-parameters measurements were obtained using a vector network analyser (VNA) configured with a pair of WR-19 waveguide to coaxial adapters. Figure 4.7-1 a) shows

the Silicon resonator inside of the test-fixture and b) with the waveguide-to-coaxial adapters ready for the measurements.

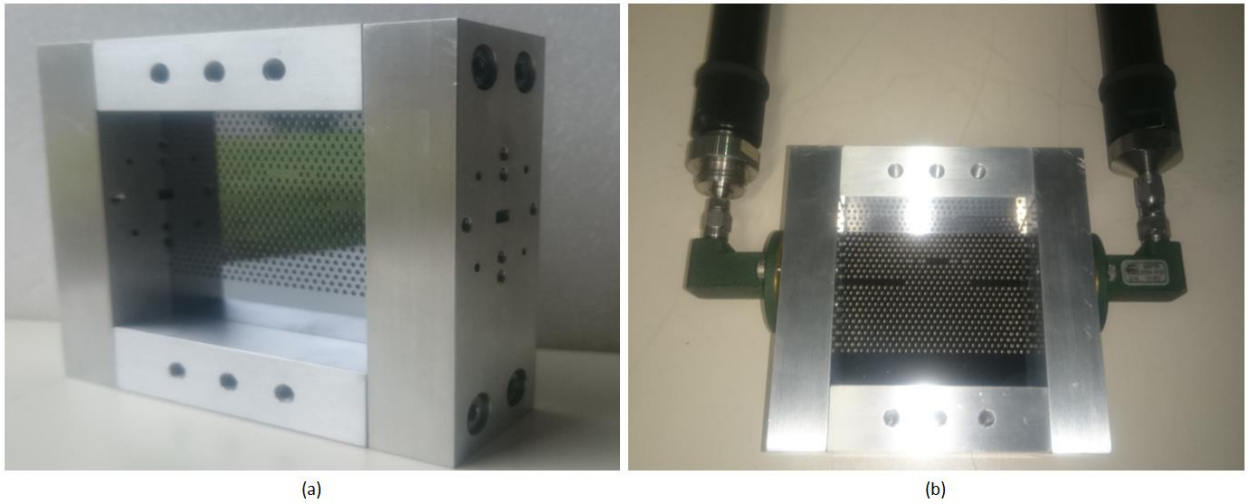


Figure 4.7-1 a) Silicon resonator inside of the test-fixture, b) Close-up view of the Silicon resonator in the test-fixture connected to the waveguide-to-coaxial adapters.

Measurements were undertaken by a thru-reflect-line (TRL) calibration. The calibration kit employed WR-19 waveguide standards composed of a thru connection (a quarter-wave offset), a flush short-circuit and a fixed termination. The vector network analyser was configured having the channel settings to attend linear frequency sweep type, 20,001 points, intermediary frequency (IF) of 1 KHz, power -5 dBm over 50 Ω load. Two types of measurements were performed, broadband (40.00 to 60 GHz) and narrowband (44.00 to 48.00 GHz) as displayed in Figures 4.7-4 and 4.7-5 respectively.



Figure 4.7-2 Silicon resonator inside of the test-fixture connected to the vector network analyzer.

In Figure 4.7-2, the Silicon resonator is inserted properly inside of the metal test-fixture with the tapers aligned with the centre of each waveguide adapter and finally the adapters are then connected to the vector network analyser to perform and extract the full two-port S-parameters.

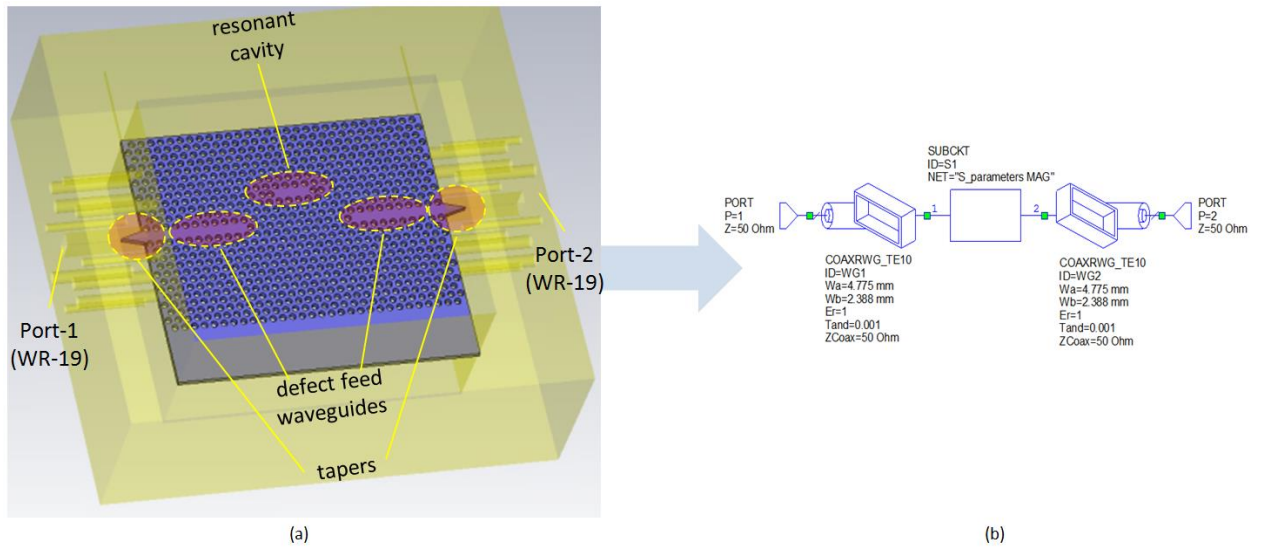


Figure 4.7-3 a) Silicon resonator inside of the text-fixture b) Silicon resonator S-parameters including coaxial-to-waveguide adapters (TE_{10} mode), losses included.

Figure 4.7-3 shows the Silicon resonator inside of the test-fixture in the simulation environment. Lossy metal (Aluminium) was considered for it and afterwards the full two-port S-parameters were exported to Microwave Office™ circuit simulator in order to match the waveguide characteristic impedance to 50 Ω system impedance, so that the results are equally comparable.

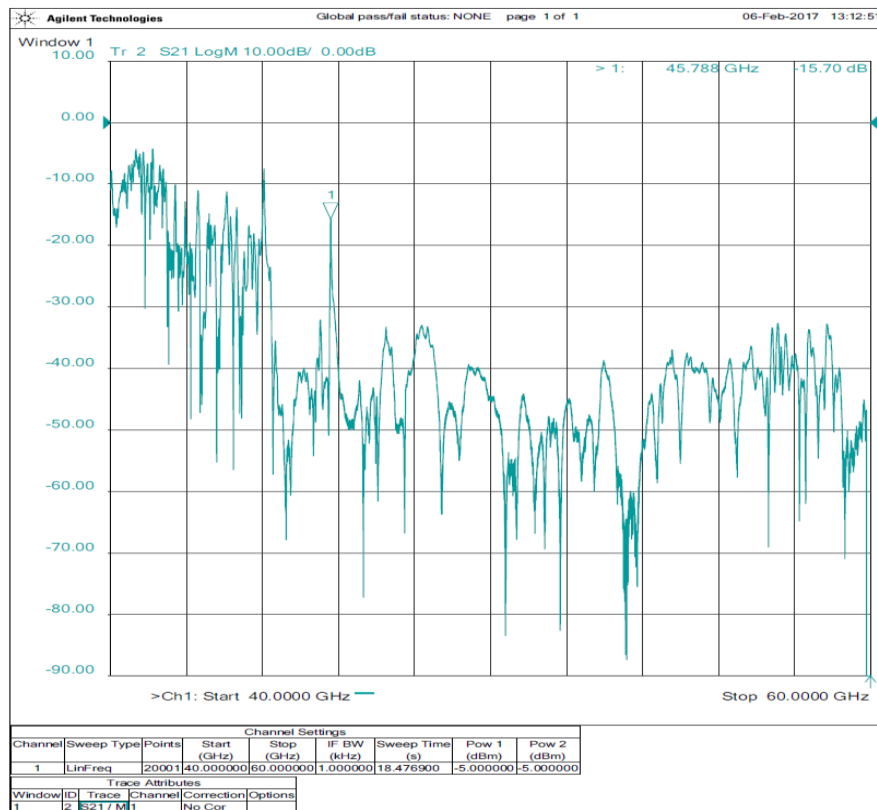


Figure 4.7-4 S-parameter (S_{21}) of the measured resonator structure (wideband version).

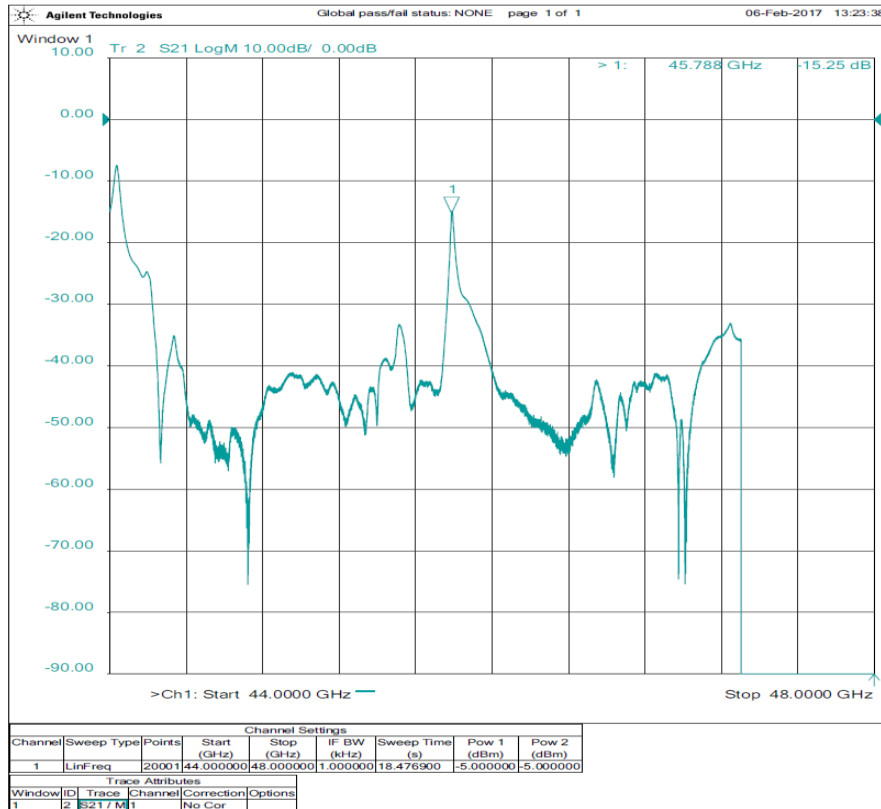


Figure 4.7-5 S-parameter (S_{21}) of the measured resonator structure (narrowband version).

The S-parameter results (S_{21}) of the measured structure set-up are displayed in Figures 4.7-4 and 4.7-5, broadband (40.00 to 60.00 GHz) and narrowband (44.00 to 48.00 GHz) respectively.

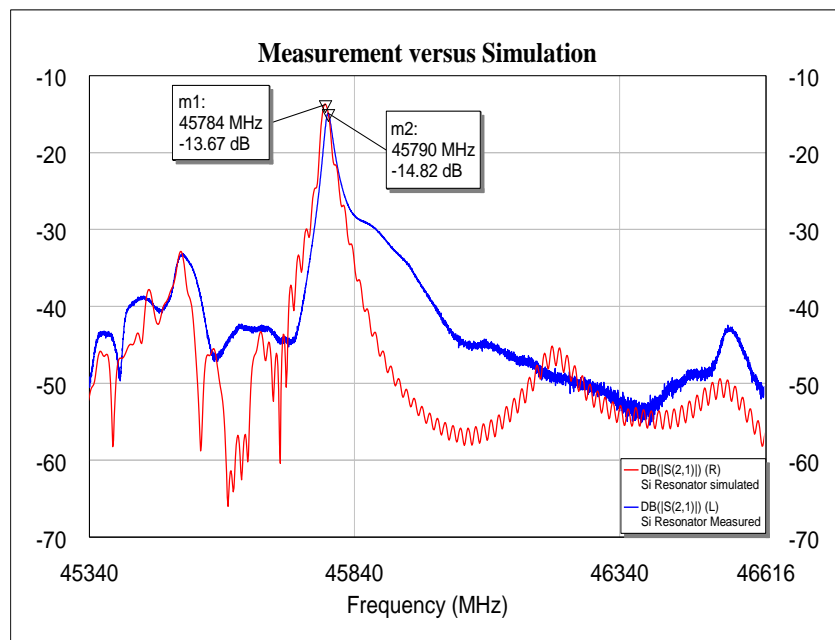


Figure 4.7-6 S-parameter (S_{21}), measured versus simulated of resonator structure.

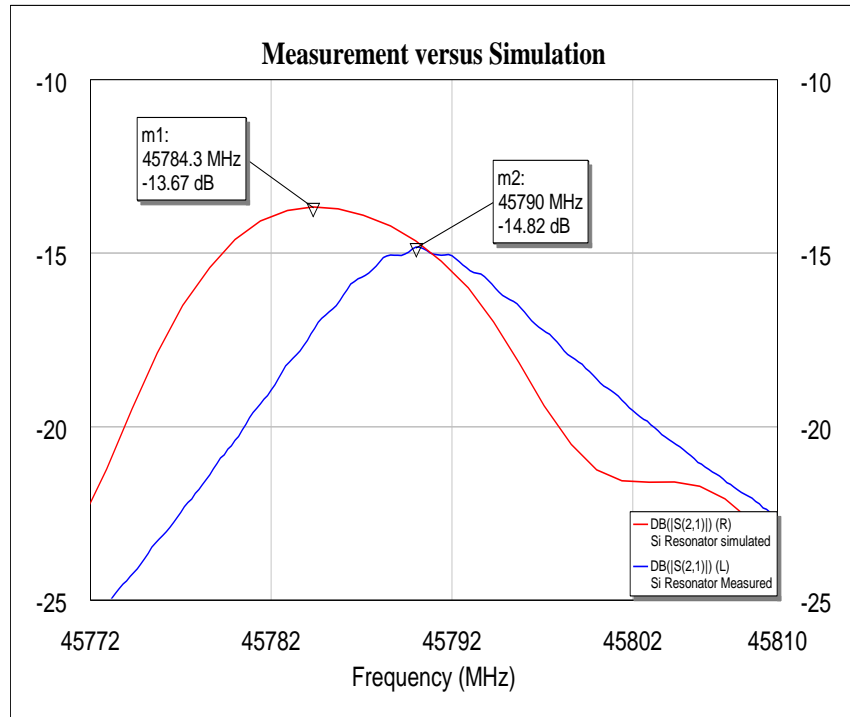


Figure 4.7-7 S-parameter (S_{21}) measured versus simulated of resonator structure (zoom).

Finally, from Figures 4.7-6 and 4.7-7, the following differences in the results between simulation and measurements were computed. These final results are displayed below in Table 4.7-1.

Si Resonator	Peak Amplitude (dB)	Peak Resonance (GHz)	Bandwidth _{-3dB} (MHz)	Loaded-Q	Unloaded-Q
Simulated	-13.67	45.784	16.92	2706	3414
Measured	-14.82	45.790	14.62	3132	3826

Table. 4.7-1 Difference in the results between simulation (including etching effects) and measurements.

Finally, an electrical representation of the measured resonator was reproduced using the lumped elements of the circuit simulator library. The schematic circuit is showed in Figure 4.7-8. The characteristics of the electrical representation of the resonator are valid only near the resonance peak, as the effects of band-gap and high rejection out-of-band are of no interest for the oscillator circuit.

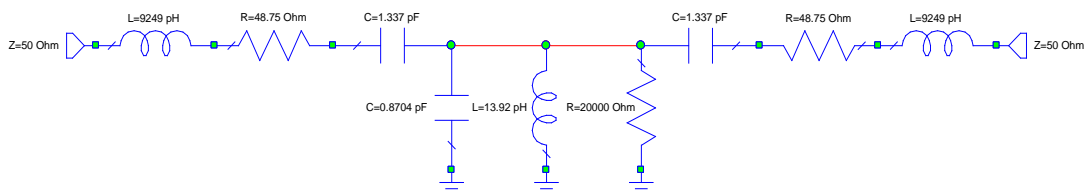


Figure 4.7-8 Equivalent electrical circuit representation of the measured resonator using lumped elements.

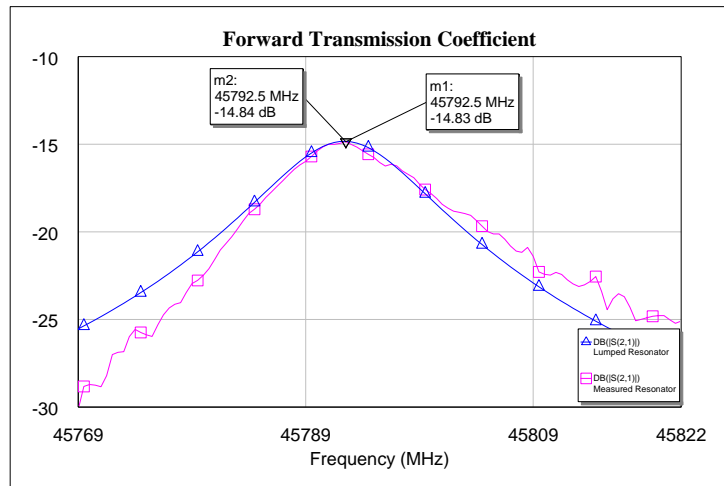


Figure 4.7-9 Forward transmission coefficient (S_{21}) of the measured and lumped resonators.

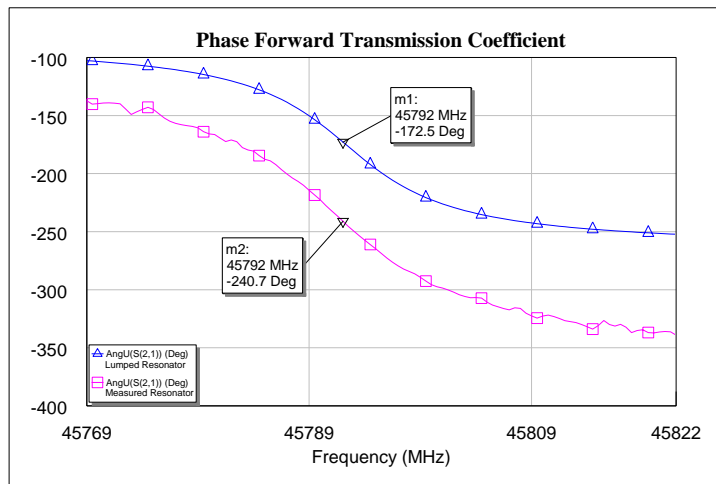


Figure 4.7-10 Unwrapped phase (S_{21}) in degrees of the measured and lumped resonators.

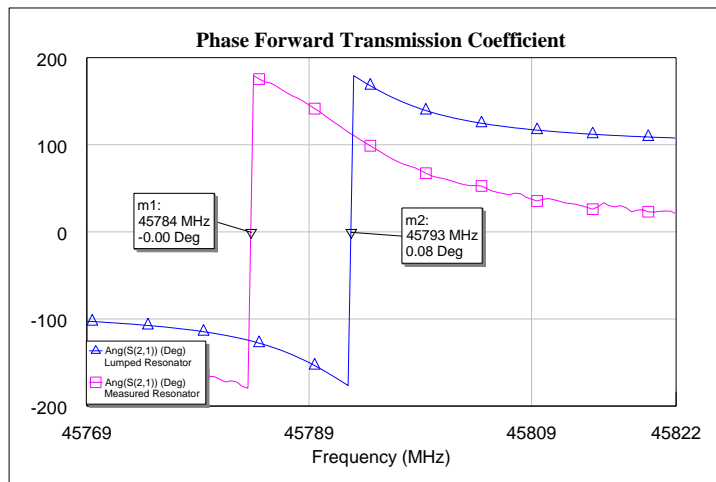


Figure 4.7-11 Wrapped phase (S_{21}) in degrees of the measured and lumped resonators.

In a real scenario, the EBG resonator has to work inside of a closed cavity in order to avoid external perturbations that could cause potential undesired effects such as frequency shift, amplitude attenuation and a reduction in the Q-factor. However, due to the size of the cavity, other mode(s) could also resonate and couple to the input and output waveguide interface ports. The undesired mode(s) were predicted under simulation environment using the time domain solver of CST Studio Suite™. Several resonance peaks appeared next to the desired resonant peak (S_{21}) and cause a reduction in its amplitude.

In order to attenuate any undesired effects, two layers (5.080 mm thick) of RF absorber material (Eccosorb BSRU-2) were placed on the top and bottom of the internal part of the metallic cavity (see Figure 4.7-12) without affecting the fundamental mode. It was found that optimum distance between the EBG resonator and the absorbers is 22.50 mm.

The cavity itself can also act as an oven to be controlled by temperature in order to guarantee good frequency stability over the time. This could be done by cycling the resonator over a temperature range while observing the shift in frequency. Through a graphic of temperature versus delta frequency, it was possible to determine the turn-over point where variation in frequency is minimum, then stabilize the temperature of the cavity to be the same as found in the turn-over point temperature, through heat transistors seated in the outside part of the metal cavity.

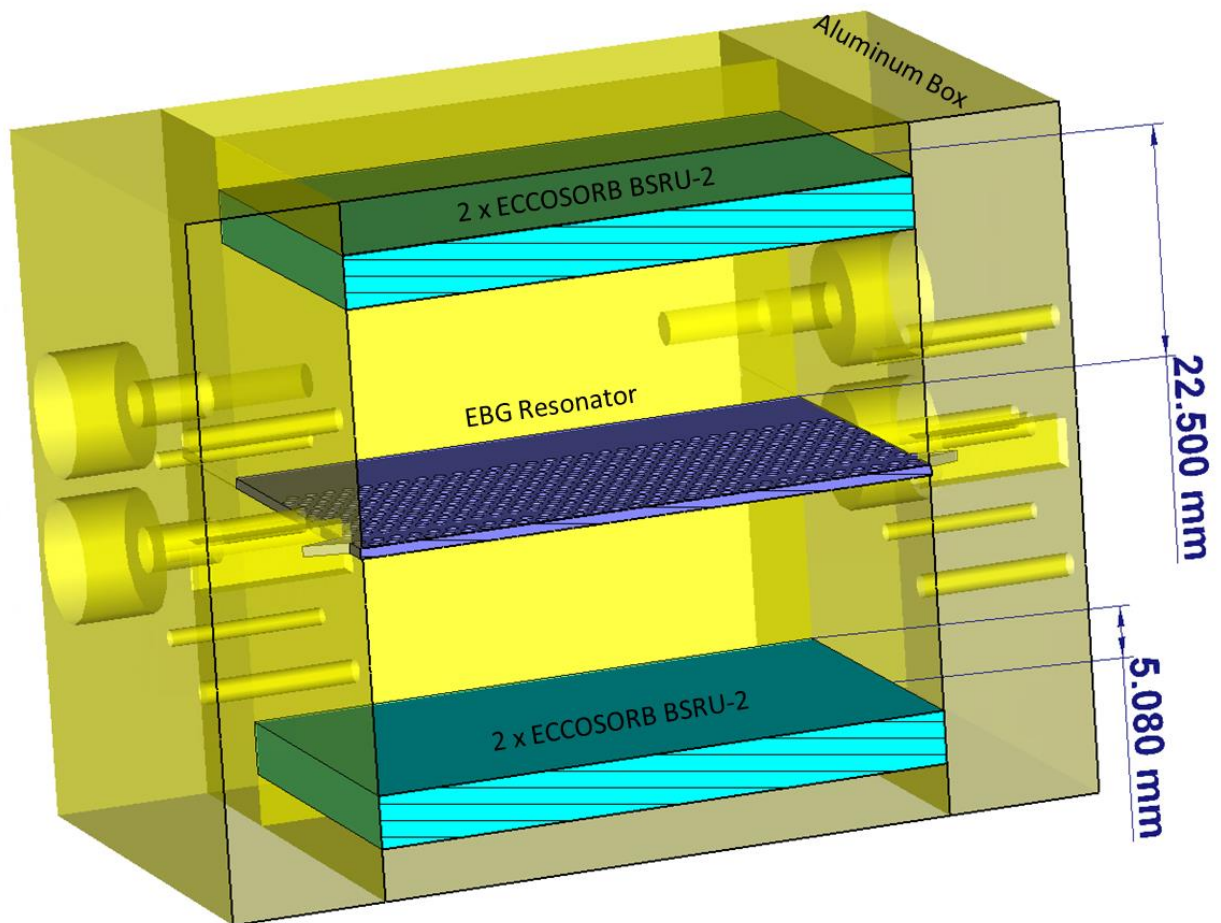


Figure 4.7-12 The EBG resonator inside of a closed metallic (Al) cavity with absorber material (Eccosorb BSRU-2) to avoid undesired effects affecting the desired resonant mode.

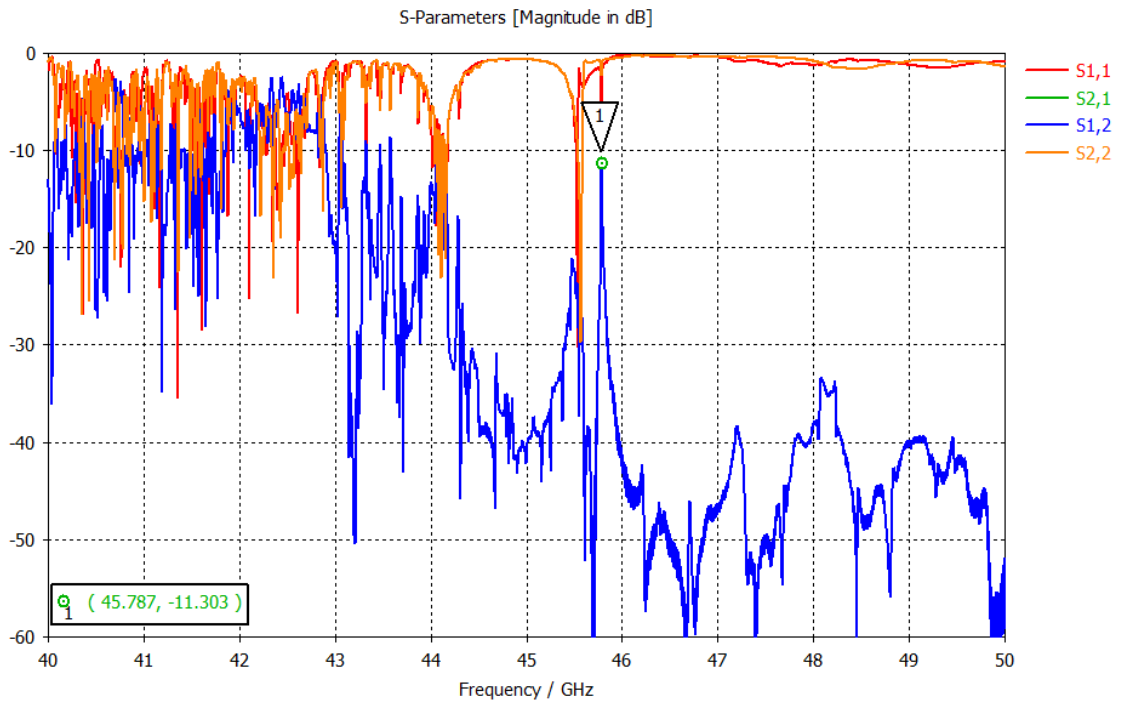


Figure 4.7-13 Full s-parameters response of the EBG resonator inside of a closed metallic cavity.

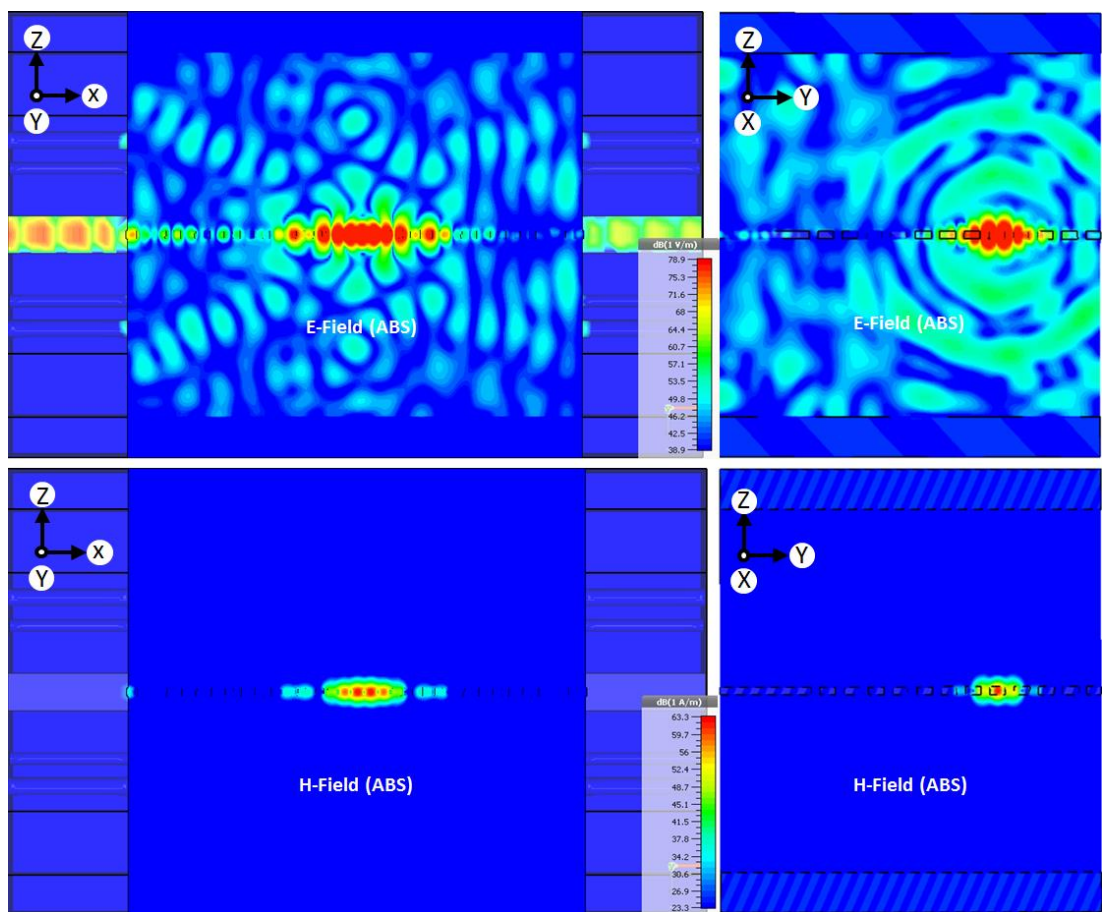


Figure 4.7-14 E-field and H-field (ABS) components distribution inside of a closed metallic (Al) cavity with absorber material (Eccosorb BSRU-2), side views.

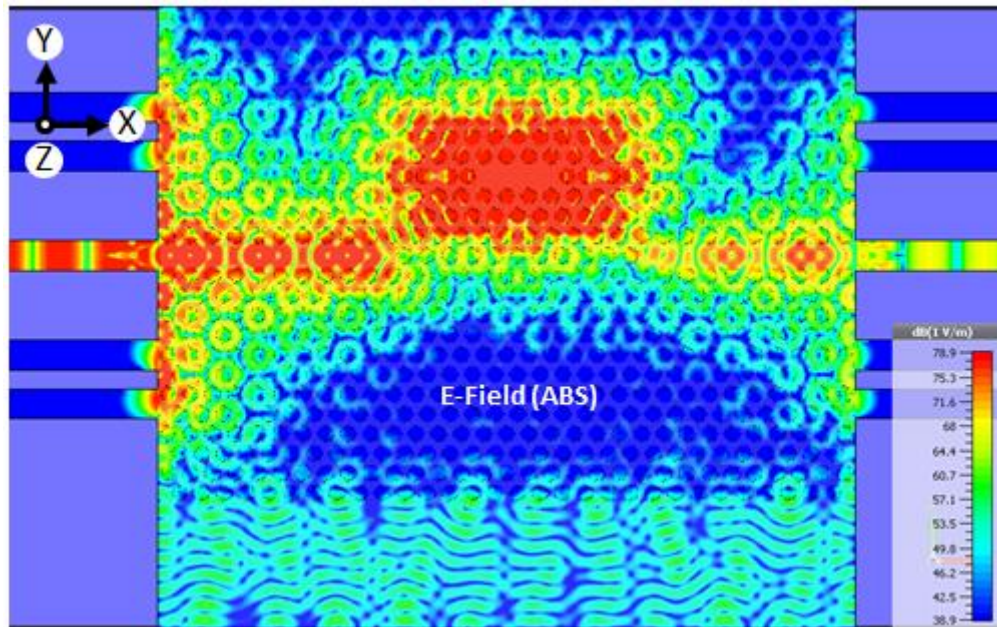


Figure 4.7-15 E-field (ABS) components distribution inside of a closed metallic (Al) cavity with absorber material (Eccosorb BSRU-2), top view.

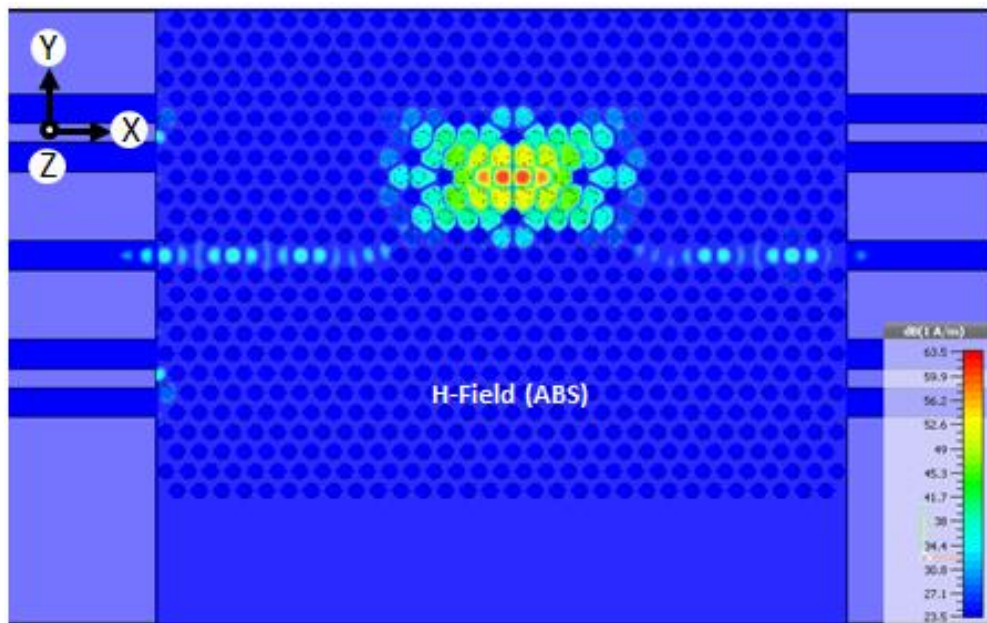


Figure 4.7-16 H-field (ABS) components distribution inside of a closed metallic (Al) cavity with absorber material (Eccosorb BSRU-2), top view.

The resonator can also work as one-port device either terminating the second port with a 50Ω impedance load or be designed and optimised to have a single port as it is described below.

Simulation models are increasingly being used to solve problems and to aid in decision-making by building virtual prototyping. The verification and validation of numerical computer simulation models is used with the ultimate goal of producing an accurate and credible model,

helping the designers to save time and money, thus avoiding the realisation of physical prototypes.

Using a full 3D electromagnetic solver (CST Studio Suite™) it has been demonstrated that an accurate prediction of the real results can be obtained when proper introduction of the electromagnetic problem as well as settings are done.

The results in Figure 4.7-7 definitely show a good correlation between simulation and measurement after the introduction of etching effects, therefore validating this simulation tool for further improvement and progress of the structure itself.

After the accurate results of the simulation tool were demonstrated with the purpose of developing an even better structure with higher Q-factor, an improved version of the resonator structure now with two defect cavities placed symmetrically in the substrate were developed and simulated.

The unloaded Q-factor calculated from the transmission coefficient (S_{21}) shows a significant increase compared with a resonator possessing a single defect cavity, the value of unloaded Q-factor achieved is 5,377. It also shows a lower insertion loss of -7.25 dB. This improvement demonstrates that theoretically lower phase noise can be achieved in the microwave oscillator design.

To obtain a good phase noise performance, the Q-factor of the oscillator network shall be as high as possible; thus, and thus increasing the Q-factor of the resonator will boost the Q-factor of the oscillator network. The simulated results of the improved resonator possessing two defect cavities are shown in Figure 4.7-18.

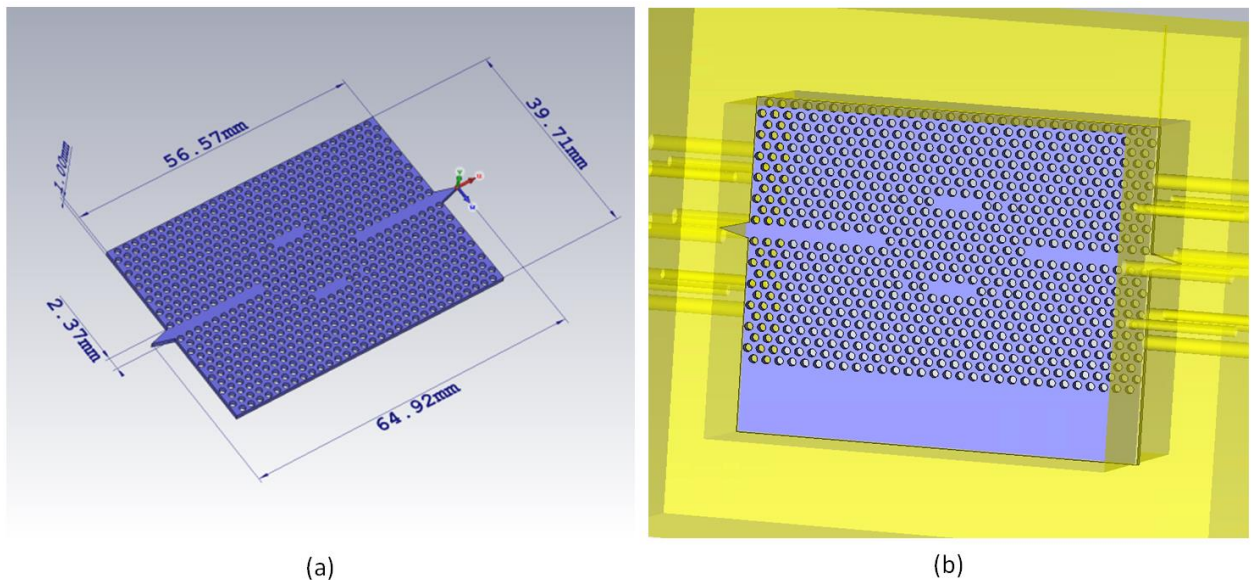


Figure 4.7-17 Simulated improved resonator structure with two defects positioned symmetrically in the substrate (a) inside of the metallic test-fixture (b).

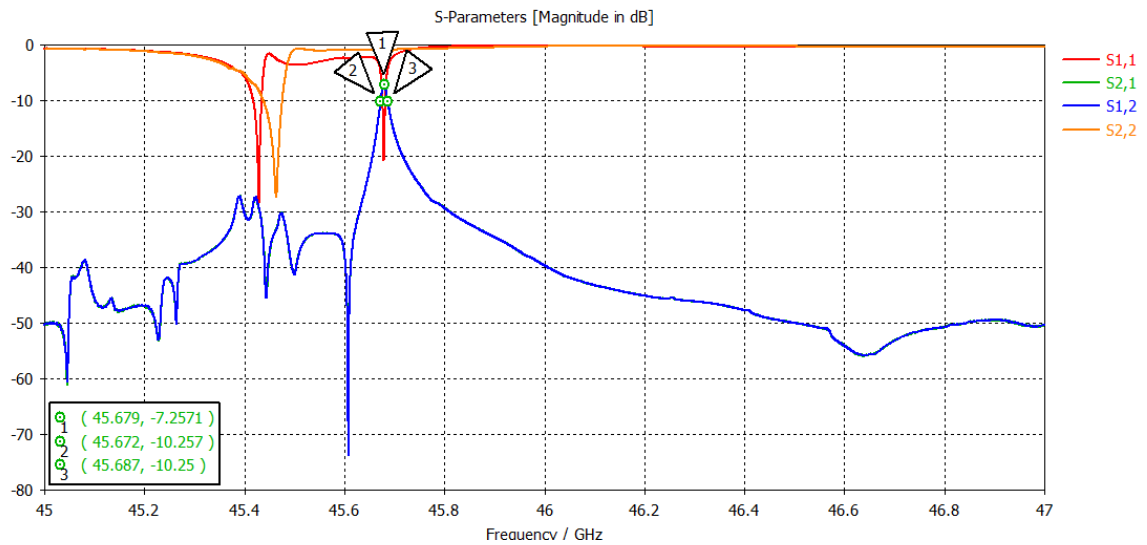


Figure 4.7-18 Simulated full two-port S-parameter of the improved resonator structure with two defects showing better Q -factor (compared to the traditional resonator structure with one defect only).

In this first part of the Thesis, a detailed theory, simulation and optimisation as well the fabrication and measurements of the Silicon resonator were presented. In the second part of the Thesis, the design of the oscillator circuit will be covered including theory, modelling, circuit simulation and optimisation.

5. OSCILLATOR CIRCUIT DESIGN

5.1. OSCILLATOR THEORY

An electronic oscillator is a device that works on the principle of oscillation producing a periodic, oscillating signal often a sine wave by converting DC-power to RF-power. Usually an oscillator behaves as an unstable amplifier in a feedback path to create a desired signal at the frequency of interest. The noise produced by the oscillator passes through a high selective mechanism, a filter, using positive feedback at the desired frequency. The signal is amplified until it reaches saturation. The gain in the closed loop will saturate to unity at steady state and the active device will compensate for the losses in the feedback path.

Oscillators are used to generate signals in almost all RF and microwave communication systems. System applications working at higher frequencies and adopting novel technologies have led to a demand for more efficient oscillator circuits with higher performance, but reduced cost, size and power consumption.

The growing necessity to attend dramatic changes in the development of the telecommunication services moving from low to high data rates employing complex modulation schemes such as m-PSK and m-QAM makes parameters such as phase noise affecting the symbol representation an essential key aspect of performance. The more complex the modulation scheme (the so called High Order Modulation MODCODs of DVB-S2X standard calling for a 256APSK High SNR mode), the more sensitive the system is to imperfections in the radio transport. In radio systems this implies employing oscillators requiring very low phase noise to cope with that problem.

Reference oscillators currently employed in most telecommunication systems are based on traditional quartz resonators which are limited in the frequency of operation to a maximum of 100 MHz. Deriving GHz range signals from this reference requires frequency multiplication or frequency synthesis. However, the multiplication increases the phase noise of the output signal according to the 20 log of multiplication factor and it also increases the complexity of the circuits. Obviously, it would be very desirable if the reference signal could be generated readily at a higher frequency. However, this would need, a high Q-factor resonator preferably operating at several GHz. Additionally, oscillators operating directly at fundamental mode in high frequency based on ceramic resonators offer poor to average phase noise close to carrier, poor stability and are normally not available above 15 GHz.

Therefore, the second part of the Thesis aims at investigating and characterising oscillator circuits operating in the millimetre-wave range, under the simulation environment, suitable to be used with the ultra-high Q-factor resonator successfully demonstrated in the first part of the thesis work. Operating directly in the fundamental mode at the frequency of interest, these oscillators will enable great benefits in obtaining low phase noise, instead of using frequency multiplication or synthesis.

In the millimetre-wave range, an oscillator can be seen either as a positive feedback system or as a reflection (negative resistance) amplifier connected to a resonator.

The thesis will cover feedback and negative resistance oscillator types. In reality, there are other variants of oscillators such as differential cross-coupled, Clapp or differential Colpitts suitable for low phase noise application.

Feedback oscillators

The oscillation occurs when an amplifier is provided with a feedback path that satisfies two conditions at the frequency of oscillation, the amplitude (gain and loss through the amplifier and feedback network) must be greater than unity; and the phase condition in the feedback loop shifts totals 360° (or 0°).

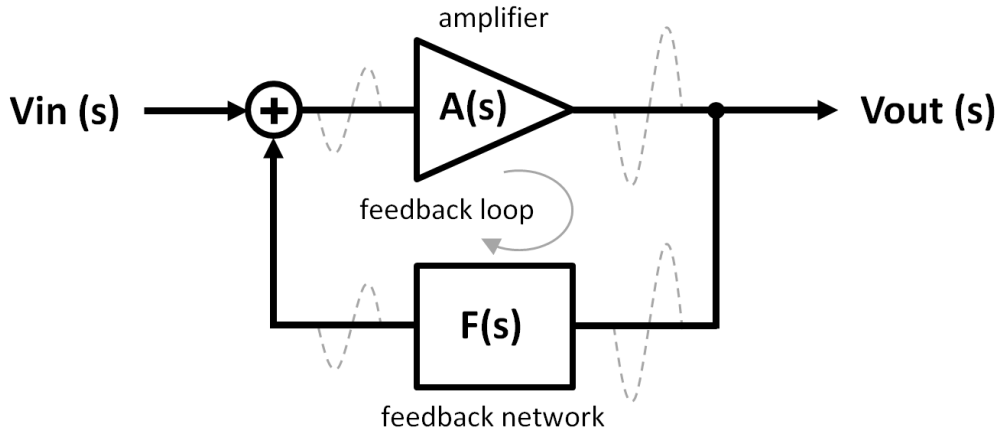


Figure 5.1-1 Block diagram of a feedback oscillator.

The output signal (V_{out}) in Figure 5.1-1 can be expressed according the following equation:

$$V_{out}(s) = V_{in}(s) \frac{A(s)}{1 - A(s)F(s)} \quad 4.52$$

The Barkhausen criterion, a necessary condition for the oscillation, states that if $A(s)$ is the gain of the amplifier in the circuit and $F(s)$ is the transfer function of the feedback path (the resonator), so the product $F(s) \cdot A(s)$ as the loop gain, the circuit will sustain steady-state oscillation only at frequencies when the following conditions are fulfilled:

$$|A(s)F(s)| = 1 \quad 4.53$$

$$\angle A(s)F(s) = n360^\circ \quad 4.54$$

As can be seen, in 4.53 the loop gain is greater than unity in absolute magnitude and in 4.54 the phase shift around the loop is zero or an integer multiple of 2π .

Negative resistance oscillators

The oscillation corresponds to the overall single-port impedance or admittance being equal to zero. This relies on S_{11} of an amplifier in a circuit being greater than unity at the frequency of oscillation. The amplifying active part is described as one-port negative resistance $A(s)$ connected to a transfer function $R(s)$ (the resonator).

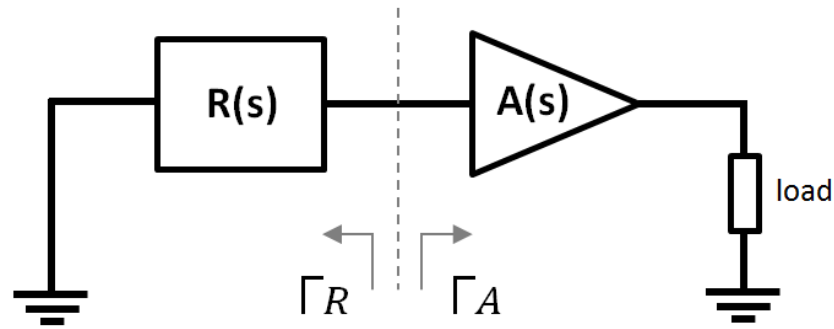


Figure 5.1-2 Block diagram of a negative resistance (one-port) oscillator.

In Figure 5.1-2, $A(s)$ represents the active device and $R(s)$ the frequency response of the resonator, illustrated in Figure 5.1-2. The circuit will sustain steady-state oscillation only at frequencies when the following conditions are fulfilled:

$$|\Gamma_R \Gamma_A| = 1 \quad 4.55$$

$$\angle \Gamma_R \Gamma_A = n360^\circ \quad 4.56$$

In 4.55, the product between the reflection coefficients of the resonator and amplifier, respectively Γ_R and Γ_A , must be greater than unity and in 4.56 the phase shift product must be zero or an integer multiple of 2π .

Resonators

The resonator is a passive device whose impedance changes rapidly with the frequency over a narrow frequency bandwidth as it acts as the frequency selective part determining the frequency of oscillation. The resonator can be represented as the core of the feedback network in a feedback oscillator or a single port impedance tank circuit in a negative resistance oscillator. The frequency response (transfer function) of the resonator determines the noise around the carrier and suppresses noise of unwanted frequencies by allowing the transmission of wanted signal in the feedback path.

This thesis presents a novel concept of high frequency and very low loss resonators based on the HiRes™ Silicon wafer material that is an interesting alternative to the traditional passive resonators employing metal cavity having their Q-factor limited by the resistive losses in the metal. This type of resonator based on dielectric material overcomes the problem of limited Q-factor.

The resonator can be used either as a two-port device in the case of feedback oscillators or one-port device with negative resistance oscillators.

The Q-factor, according to general definition, is covered in the equation 4.46 to 4.52; however, there are other relations between the phase slope and the parallel or series resonator.

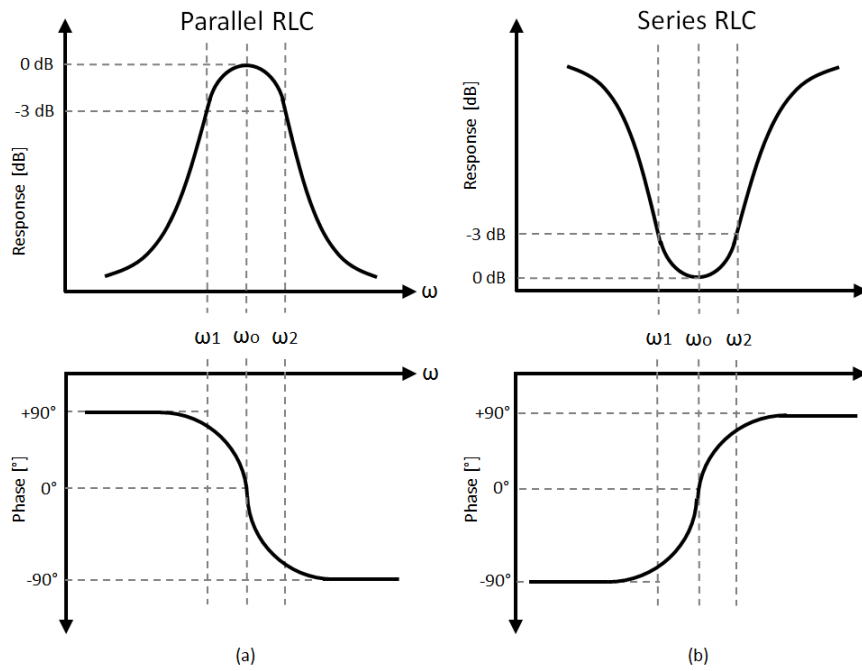


Figure 5.1-3 Diagrams for frequency response and phase slope of (a) parallel and (b) series RLC circuits.

If the equivalent electrical circuit representation of the resonator is known, the Q-factor of the resonator can be calculated directly from the component values. The EBG resonator can be represented as a parallel (two-port device) or series (one-port device) equivalent circuit as can be seen in Figure 5.1-4. The assumption is only valid to frequencies close to the resonance.

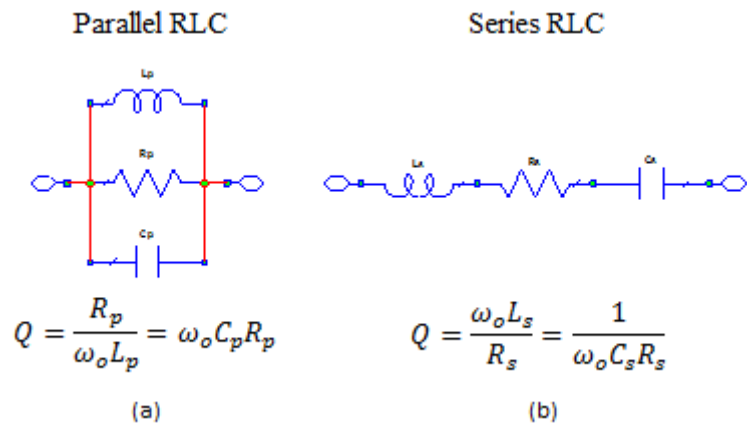


Figure 5.1-4 Equivalent electrical circuit representation for (a) parallel RLC and (b) series RLC resonator and their respective Q-factor.

The Q-factor is a measure of loss in resonant circuits. Usually it is desirable to achieve high Q-factors in resonant (RLC) circuits as it will ensure lower losses and phase noise in oscillators. As per definition, in 4.36, Q-factor is 2π times the ratio of the total energy stored divided by the energy lost in a single cycle or equivalently the ratio of the stored energy to the energy dissipated over one radian of the oscillation. Higher Q-factor indicates a lower rate of energy loss relative to the stored energy of the resonator.

A definition of unloaded Q-factor for the parallel and series resonances are shown in the relations 4.57 and 4.58 respectively. In the parallel RLC, the Q-factor increases as R increases. Contrary to the parallel RLC, the Q-factor of a RLC decreases as R increases.

In Figure 5.1-3 the frequency response in decibels and the respective phase slope in degrees are show for each RLC cases.

$$Q = \frac{R_p}{\omega_o L_p} = \omega_o C_p R_p \quad 4.57$$

$$Q = \frac{\omega_o L_s}{R_s} = \frac{1}{\omega_o C_s R_s} \quad 4.58$$

In oscillator applications, the Q-factor of the resonant network is proportional to the slope of the phase transfer function illustrated in Figure 5.1-3 for both cases of parallel and series RLC circuits. The different noise sources in the circuit introduces temporary phase lead or lag which needs to be compensated by change in frequency according the equations 4.67 and 4.68. In oscillators with large Q-factor, the required instantaneous change in frequency for given phase shift is smaller, thus leading to a better frequency stability.

The relationship between the phase slope of the input impedance (Z_p) for a parallel resonator can be defined in equation 4.59.

$$Q_p = -\frac{\omega_o}{2} \frac{\partial \phi(Z_p)}{\partial \omega} \Big|_{\omega = \omega_o} \quad 4.59$$

Otherwise, in the case of a series resonator the phase slope of the input impedance (Z_s) is defined according equation 4.60.

$$Q_s = \frac{\omega_o}{2} \frac{\partial \phi(Z_s)}{\partial \omega} \Big|_{\omega = \omega_o} \quad 4.60$$

Phase and Amplitude Noise

Phase noise is the frequency domain representation of rapid, short-term, random fluctuations in the phase and amplitude of a waveform, caused by the time domain instabilities of an oscillator circuit. Oscillators inherently produce high levels of phase noise, that increases at frequencies close to the oscillation frequency or its harmonics and cannot be filtered out.

An ideal oscillator would generate a sine wave at a given frequency with no deviation in amplitude or phase over time. However, in practice, the waveform of an oscillator varies both in amplitude and phase as a function of time and are referred to amplitude noise and phase noise produced by the non-ideal characteristics of the active circuit and passive resonator.

Figure 5.1-5 illustrates the effects of the amplitude and phase noise of an oscillator in the time domain. The analysis of the output waveform in a real case scenario is broken in two parts to

understand the individual contributions of phase and amplitude variations over the time. In the upper part (a) of the illustration the dashed line shows the case of an ideal oscillator where no amplitude noise is present, while the solid line shows the case of a real oscillator having the output waveform with a large amount of amplitude noise. The lower part (b) of the illustration shows the same behavior for a real oscillator but now with regards to the phase variations over the time. In the dashed line, the time between the zero crossings of the output waveform varies over the time when compare to a sine waveform of an ideal oscillator.

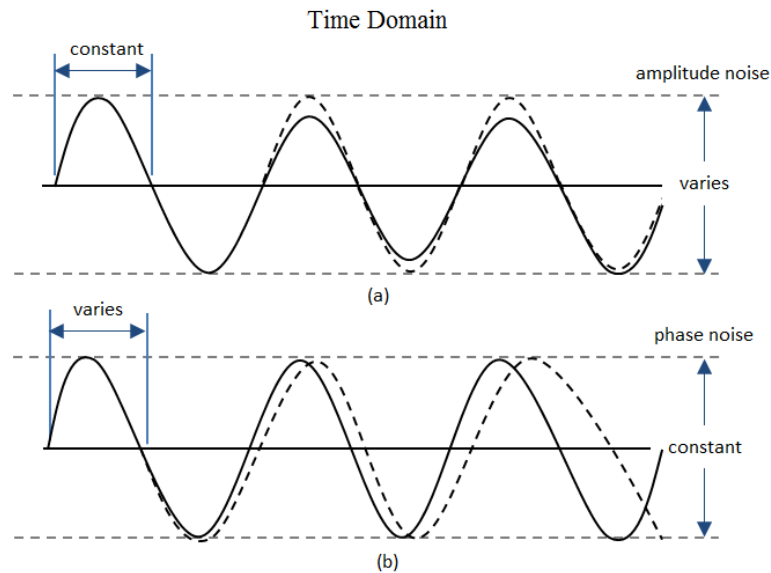


Figure 5.1-5 Amplitude and phase noise variation over time for the ideal versus real oscillator. The signal in (a) cover the analysis of amplitude variations while (b) covers the phase variations.

In the frequency domain, an ideal oscillator signal is represented by a spectral line with no phase noise present in the signal, while in a real oscillator the signal is no longer a discrete spectral line but represented by a spread of spectral lines in the form of modulation sidebands due to the random amplitude and phase fluctuations. This is illustrated in Figure 5.1-6 where (a) represents the ideal case and (b) the real case scenario for oscillator signals seen in the frequency domain.

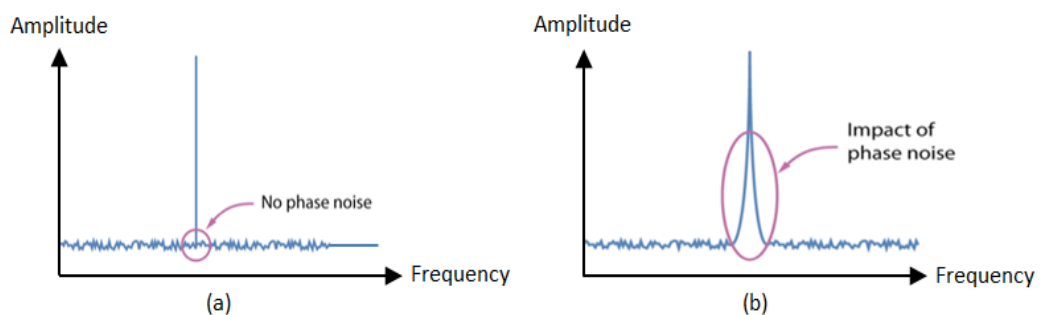


Figure 5.1-6 Amplitude and phase noise variation over frequency for the ideal (a) versus real oscillator (b).

In time domain, an ideal signal of an oscillator can be represented as following:

$$V_{(t)} = A_o \sin(\omega_o (t)) \quad 4.61$$

In a real world, the signal of an oscillator in time domain can be represented as following :

$$V_{(t)} = (A_o + E(t)) \sin(\omega_o(t) + \phi_o(t)) \quad 4.62$$

In order of importance, the amplitude noise is less important than phase noise. This occurs because most oscillators tend to produce less amplitude noise than phase noise due to the fact the active devices (transistors) operate in gain-saturated conditions. This is achieved when increasing the input to a device results in no further increase in the output, therefore if the device works in gain-saturated condition small changes in amplitude of the input signal (amplitude noise) produce no change in the output level. Then the amplitude noise can be easily counteracted adding a limiting amplifier stage at the output of the native oscillator core.

Over time different modelling equations for the phase noise prediction have been developed. They differ in complexity and rely on which noise sources are included in the model and how noise is processed in the simulation environment.

In the sub-chapter 5.5 “*Circuit Simulation and Optimization*”, Microwave Office™ circuit simulation software will be employed to automatically calculate the overall phase noise based on the different source contribution of the oscillator. First, a Harmonic Balance (HB) analysis is performed which does not include any noise analysis. The tone frequencies and their harmonics are pure sinusoidal signals without any noise sidebands. The noise analysis is performed after the HB solution. From the noise point of view, the oscillator works like a mixer device. Noise power at low frequencies gets converted to noise sidebands around the carrier and its harmonics.

Large signal oscillation drives the circuit into non-linear state and elements such as conductance and capacitance become time-dependent.

The conductance and capacitance are sampled and Fourier-transformed to get a conversion matrix. The conversion matrix describes how individual noise sources contribute to noise sidebands. The overall phase noise is then obtained summing the individual contributions of different sources.

Phase noise behavior in oscillators were described and quantified by D. B. Leeson [9]. Leeson’s model assumes several factors that predicts individual contributors to the phase noise and classified according to their respective curve slopes as shown in Figure 5.1-7 (a).

The resulting phase noise of an oscillator has many contributors given the noise factor and flicker noise of the active amplifier, loaded Q-factor and average power through the resonator as well as noise floor which is derived from recombination, thermal and shot noise; translating into a well prediction of the phase noise.

Figure 5.1-7 (a) below illustrates the different noise regions, in e.g. the case of high Q-factor oscillator, Lesson’s equation (b) for the single sideband (SSB) phase noise is specified in dBc/Hz.

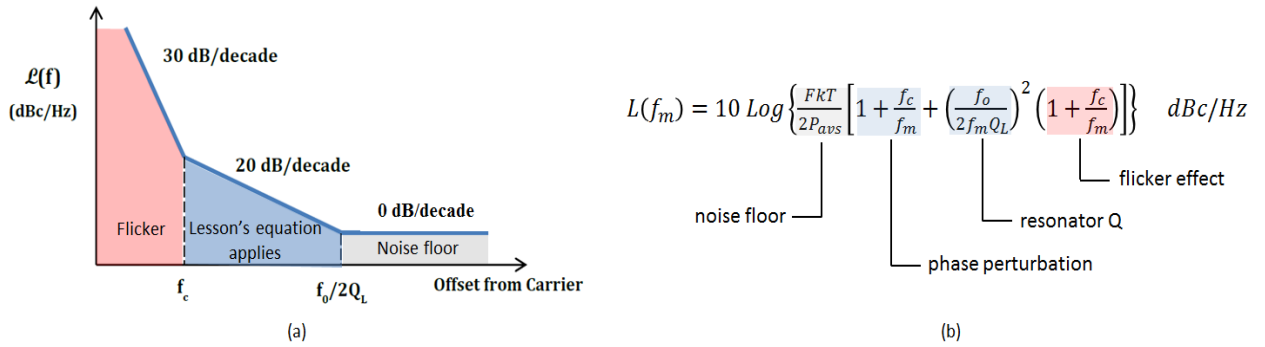


Figure 5.1-7 a) SSB phase noise in dBc/Hz versus frequency offset, b) Leeson's equation for SSB phase noise.

Phase noise is usually characterized in terms of single side band noise spectral density and defined accordingly:

$$L_{total}\{\Delta\omega\} = 10 \text{ Log} \left[\frac{P_{sideband}(\omega_o + \Delta\omega)}{P_{carrier}} \right] \quad 4.63$$

Where, $P_{sideband}(\omega_o + \Delta\omega)$ represents the single sideband power at the offset frequency ($\Delta\omega$) from the carrier ($P_{carrier}$) with a measurement bandwidth of 1 Hz and specified in dBc/Hz.

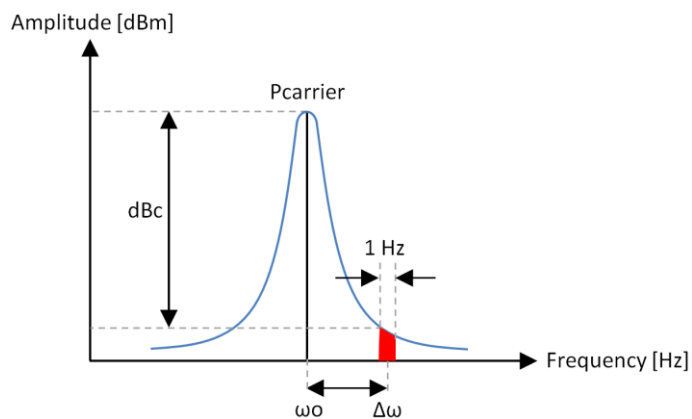


Fig. 5.1-8 Carrier portion of a sine wave and the definition of single sideband phase noise referred to a 1-Hz measurement bandwidth.

Leeson's phase noise equation is given by:

$$L_{(f_m)} = 10 \text{ Log} \left\{ \frac{FkT}{2P_{avs}} \left[1 + \frac{f_c}{f_m} + \left(\frac{f_0}{2f_m Q_L} \right)^2 \left(1 + \frac{f_c}{f_m} \right) \right] \right\} \quad 4.64$$

Where,

F = Noise factor of the active device [dimension-less]

K = Boltzmann constant [1.38×10^{-23} J/K]

T = Temperature [K]

P_{avs} = Average power through the resonator [W]

f_c = Flicker corner frequency of the active device [Hz]

f_m = Carrier offset frequency [Hz]

f_o = Carrier center frequency [Hz]

Q_L = Loaded Q-factor

It is important to mention that f_c representing the Flicker noise corner frequency is in fact derived from the fitting parameters (f_1/f_3) used for setting the noise level dependent of the active device noise as well non-linear conversion. It is normally defined between the slope of -30 dB/decade and -20 dB/decade. Outside $f_m=f_o/2Q_L$, the phase noise is inversely proportional to P_{avs} and independent of Q_L , however inside $f_m=f_o/2Q_L$ it is inversely proportional to the product $P_{avs}Q_L^2$.

It is seen that according the dependence between the Q_L of the resonator and Flicker noise corner (f_1/f_3), the phase noise ($\mathcal{L}(f_m)$) function can lead to two cases illustrated below in Figure 5.1-9.

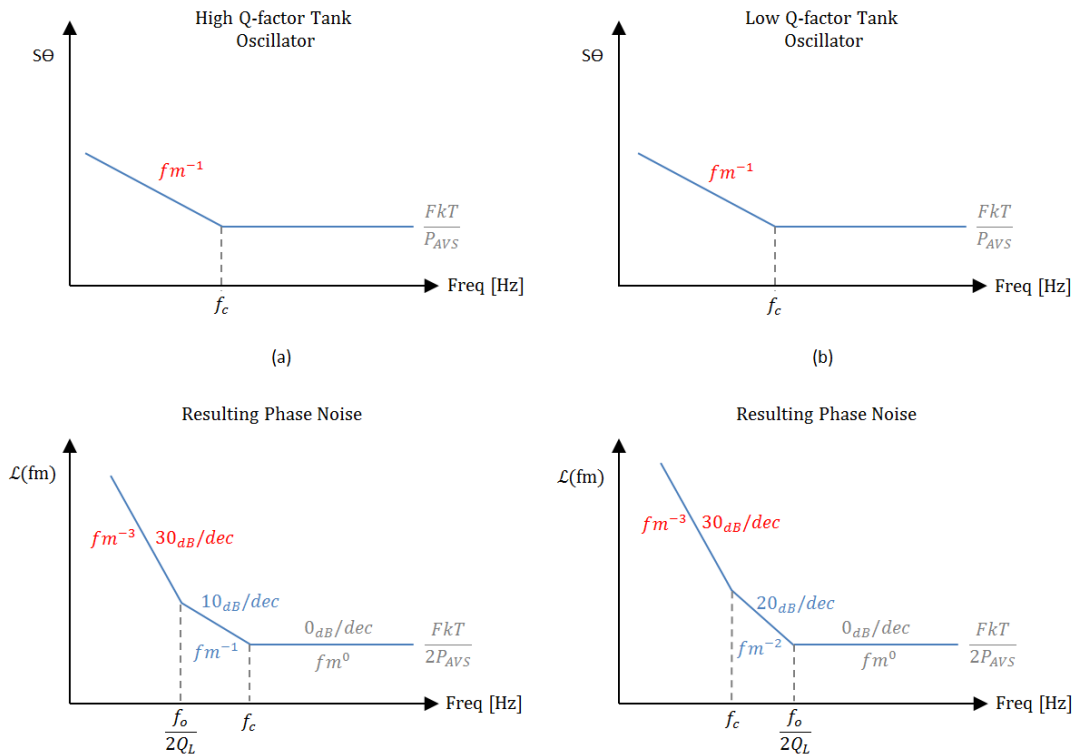


Figure 5.1-9 Typical representation of oscillator spectral density and phase noise plots for high (a) and low (b) Q -factor resonator oscillators.

For the low Q-factor case, the spectral phase noise is unaffected by the Q-factor of the resonator, however the $(\mathcal{L}_{(fm)})$ spectral density shows a $1/f^3$ and $1/f^2$ dependence near to the carrier. For high Q-factor case, a slope of $1/f^3$ and $1/f$ is observed near to carrier.

The contribution of low frequency noise components such as flicker noise near to carrier is not well defined in the Lesson's model. The model assumes a slope of 30 dB/decade with a corner frequency exactly as the corner frequency of the active device (amplifier), but measurements [10] do not offer such correlation and match. This is due to the fact Lesson's equation models the phase noise in oscillator as time-invariant system. Several authors like Lee and Hajimiri [28] have addressed this issue showing that the flicker corner frequency can be lower than the active device flicker corner frequency. Figure 5.1-10 shows how the noise spectral density ($S_n(\omega)$) actually contribute to the phase noise ($\mathcal{L}_{(fm)}$). The noise components from the harmonics frequencies are converted to the carrier phase noise. Leeson's equation fails to address those contributions, however the calculation provided by the Microwave Office™ circuit simulator calculates the spectral density of phase fluctuations of the output voltage of a noisy oscillator using the following computational details:

$$\mathcal{L}_{(fm)} = \frac{\langle V_{-k}V_{-k}^* \rangle + \langle V_kV_k^* \rangle}{2 \langle V_{0,k}V_{0,k} \rangle} \quad 4.65$$

Where V_{-k} and V_k are the lower and upper noise sidebands, respectively, and $V_{0,k}$ is the harmonic component of the steady state solution.

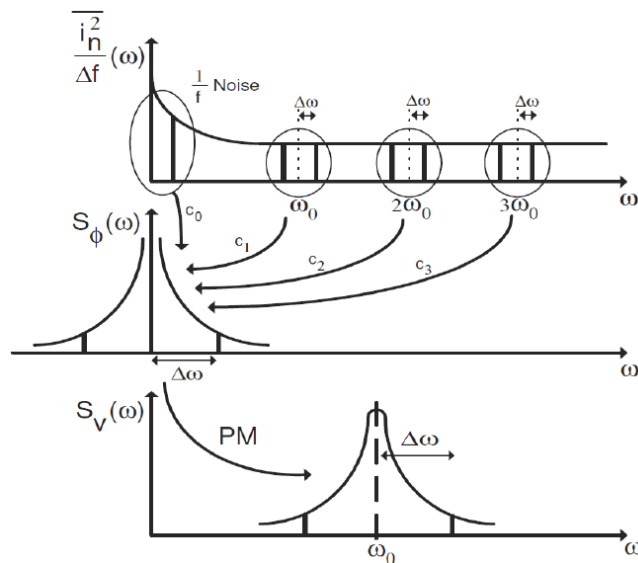


Figure 5.1-10 Conversion process of all noise at distance $\Delta\omega$ around the harmonics including DC component contributes to the phase noise.

Thermal and Noise Floor

Thermal noise (or Johnson noise) is the noise power per Hertz that arises from the thermal agitation of the charge carriers inside an electrical conductor at equilibrium and regardless of any applied voltage. It is effectively a white noise type, flat response (0 dB/dec) and extends over a very wide spectrum. The thermal noise can be calculated from the following formula:

$$N = kTB \quad 4.66$$

Where,

k = Boltzmann constant [1.38×10^{-23} J/K]

T = Room temperature in Kelvin [290 K]

B = Bandwidth in Hertz [1 Hz]

In decibels, the thermal noise becomes:

$$N_{dB} = 10 \text{Log} \left(\frac{kTB}{1mW} \right) = -173.98 \left[\frac{dBm}{Hz} \right] \quad 4.67$$

Thermal noise can limit the phase noise measurements for low-level signals. Since phase and amplitude noise contributes equally to the product kTB, the phase noise portion is equal to -176.98 dBm/Hz which is 3 dB below the total kTB power.

The noise floor is the noise created from the sum of all the noise sources and unwanted signals with a flat response limiting the measurement of an instrument since any measured amplitude cannot on average be less than the noise floor. In oscillators, noise floor is in function of the power capability of the oscillator (DC power consumption) and unloaded Q-factor. The following equation defines the noise floor and on which limits the phase noise performance for a given technology:

$$\mathcal{L}_{min}(f_m) = -173.98 - 10 \text{Log}(P_{DC}) - 20 \text{Log}(Q_o) + 20 \text{Log} \left(\frac{f_o}{f_m} \right) \quad 4.68$$

Where,

P_{dc} = DC power consumption of the oscillator [W]

Q_o = Unloaded Q-factor of the resonator [dimensionless]

f_o = Oscillator center frequency [Hz]

f_m = Offset frequency from the oscillator center frequency [Hz]

Figure of Merit

The figure of merit (FOM) parameter [12] can be employed to evaluate the performance of different type of oscillators and is defined according the following equation:

$$FOM = \mathcal{L}_{(f_m)} - 20 \text{Log} \left(\frac{f_o}{f_m} \right) + 10 \text{Log} \left(\frac{P_{DC}}{1mW} \right) \quad 4.69$$

5.2. OSCILLATOR CONFIGURATIONS

Two different types of oscillators are proposed to evaluate the performance in terms of phase noise, power level, spurious and figure of merit. The oscillator performance is mainly driven by how the resonator is connected to the circuit. In a simplified fashion, the one-port resonator can be represented as a series RLC equivalent electrical circuit having one terminal connected to the circuit and the other grounded, while the two-port resonator can be represented as a parallel RLC equivalent electrical circuit with both terminals connected to the circuit. In reality, the modelling of the measured EBG resonator is represented by a complex equivalent electrical circuit displayed in Figure 4.7-8.

The first type is a feedback oscillator. It uses transistor amplifiers connected in a feedback loop with its output fed back into its input through a frequency selective RLC equivalent circuit formed by C_0 , L_0 and R_0 to provide positive feedback. In the feedback oscillator, the EBG resonator is the frequency selective circuit acting like a sharp filter, therefore only a small amount of noise is generated so the amplifier will produce a sinusoidal signal. If the amount of positive feedback is large enough, the result is oscillation. The frequency of oscillation can be determined by the simple formula:

$$F_r = \frac{1}{2\pi\sqrt{L_0 C_0}} \quad 4.70$$

A typical feedback oscillator is depicted in Figure 5.2-1.

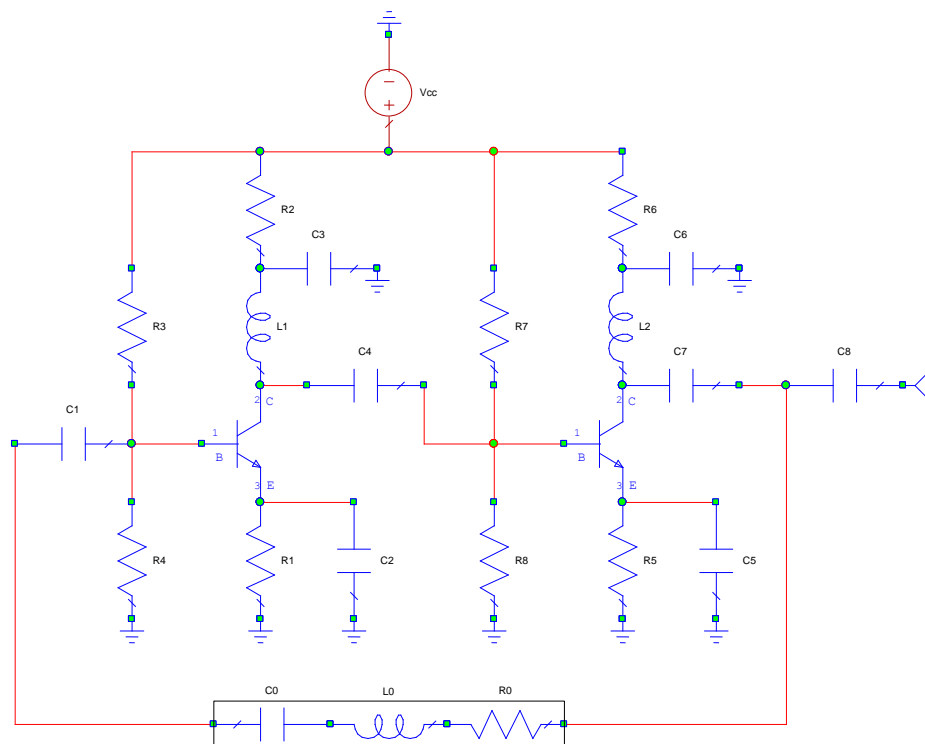


Figure 5.2-1 Simplified schematic of feedback (feed-forward type) oscillator.

The second type of oscillator is known as Clapp (modified) type composed by a single inductor (L_0) and three capacitors (C_0 , C_1 and C_2). The capacitors C_1 and C_2 form a voltage divider that determines the amount of feedback voltage applied to the transistor.

The Clapp oscillator is derived from a Colpitts version producing the feedback signal, however with the addition of the capacitor C_0 in series with the inductor L_0 . As any other oscillator, the Clapp requires a total gain of one and phase shift of zero degrees from the input to the output terminals. The frequency of oscillation can be calculated in the same way as any resonant circuit through the following formula:

$$F_r = \frac{1}{2\pi\sqrt{L_0 C_T}} \quad 4.71$$

Ignoring the capacitive effect between the transistor base and collector, the resonant frequency may be calculated using the total equivalent capacitance (C_{TOT}) given by:

$$C_T = \frac{1}{\frac{1}{C_0} + \frac{1}{C_1} + \frac{1}{C_2}} \quad 4.72$$

Figure 5.2-2 shows a typical Clapp oscillator. The frequency determining series resonant tuned circuit is formed by L_0 and C_T and is used as the collector load impedance of the common emitter amplifier. A large inductance, L_1 , provides a DC path for the collector current while presenting a high impedance at the resonant frequency. This gives the amplifier a high gain only at the resonant frequency.

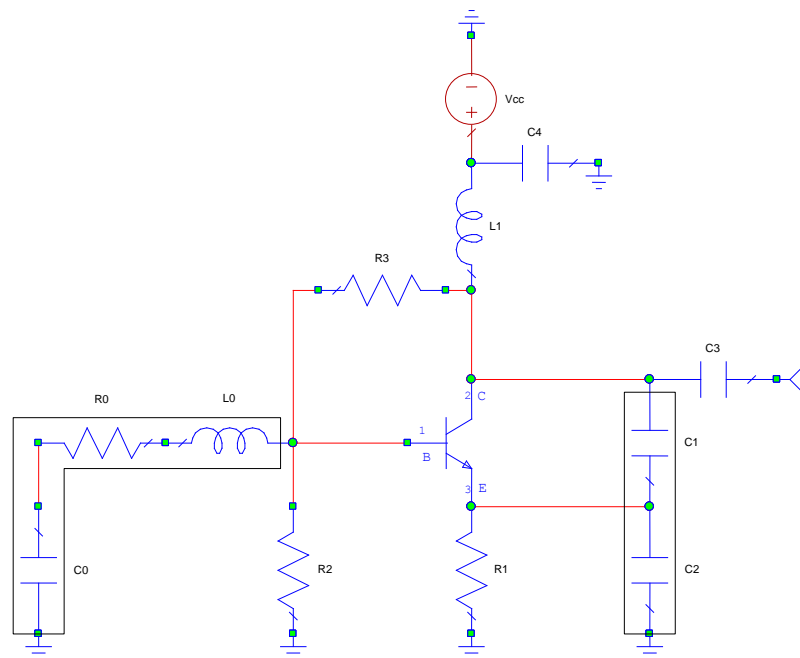


Figure 5.2-2 Simplified schematic of negative resistance (Clapp modified type) oscillator.

5.3. PROCESS DESIGN KIT (MMIC)

This chapter encompasses a description of the process design kit (PDK) library used within the simulation environment employed in the design of the oscillator at monolithic microwave integrated circuit (MMIC) level. The analog/mixed signal PDK used to design the oscillator in this thesis is the 0.13 μm BiCMOS process from IHP – Innovation for High Performance Microelectronics company. The process was chosen because it is one of the few worldwide offering the modelling of flicker (1/f) noise in addition to other parameters as it is a type of electronic noise that generates and recombines noise in a transistor due to the base current contributing considerably to the overall phase noise in any oscillator. The circuit simulation software (Microwave Office™ and Advanced Design System™) employed in this work fully supports the complete IHP SG13S PDK library at circuit and layout levels.

IHP offers research partners and customers access to its powerful SiGe:C BiCMOS technologies and special integrated RF modules. These technologies are especially suited for applications in the higher GHz bands (e.g. for wireless, broadband, radar). They provide integrated HBTs with cut-off frequencies of up to 500 GHz.

The oscillator circuit is designed using models from a high performance SiGe BiCMOS technology with 0.13 μm CMOS foundry process (SG13S) from IHP Microelectronics. It contains devices based on SiGe:C npn-HBT's with up to 250 GHz transient frequency and 340 GHz oscillation frequency. IHP Microelectronics offers a design kit based on the SG13S process known as PDK (Process Design Kit) and available for the ADS (Advanced Design Systems™) and MWO (Microwave Office™) simulation software used in the investigation and characterization of the oscillator. The kit contains accurate equivalent circuit modelling for the R-L-C elements including substrate layer file as well noise modelling for the semiconductors devices based on real data and curve fitting.

The main electrical characteristics of the SiGe BiCMOS technology for the SG13S process are the following:

Bipolar Section

SG13S	nnp13P	nnp13V
AE	0.12 x 0.48 μm^2	0.18 x 1.02 μm^2
Peak f_{max}	340 GHz	165 GHz
Peak f_t	250 GHz	45 GHz
BVCEO	1.7 V	3.7
BVCBO	5.0 V	15 V
β	900	900

CMOS Section

SG13S			
Core Supply Voltage*		3.3 V	1.2 V
nMOS	VTH	0.71 V	0.50 V
	IOUT	280 $\mu\text{A}/\mu\text{m}$	480 $\mu\text{A}/\mu\text{m}$
	IOFF	10 pA/ μm	500 pA/ μm
pMOS	VTH	-0.61 V	-0.47 V
	IOUT	-220 $\mu\text{A}/\mu\text{m}$	-200 $\mu\text{A}/\mu\text{m}$
	IOFF	-3 $\mu\text{A}/\mu\text{m}$	-500 $\mu\text{A}/\mu\text{m}$

Note : 0.13 μm BiCMOS with npn-HBT up to $f_T/f_{\text{max}} = 250/340$ GHz, with 3.3 V I/O and 1.2 V logic CMOS

Passive Section

SG13S	
MIM Capacitor	1.5 fF/ μm^2
N+ Poly Resistor	-
P+ Poly Resistor	250 $\Omega/$
High Ploy Resistor	1300 $\Omega/$
Varactor Cmax/Cmin	tbd.
Inductor Q @ 5 GHz	18 (1 nH)
Inductor Q @ 10 GHz	20 (1 nH)
Inductor Q @ 15 GHz	37 (1 nH)

The PDK offers a complete ADS/MWO software based flow in a silicon based technology listed below:

- Schematic entry
- Simulation
- Momentum/Axiem EM solvers
- Layout including Pcells
- DRC check
- Microstrip lines
- GDS export
- LVS check
- Si toolbar for easy design

The stack-up process cross section for the SG13S process is shown below in Figure 5.3-1.

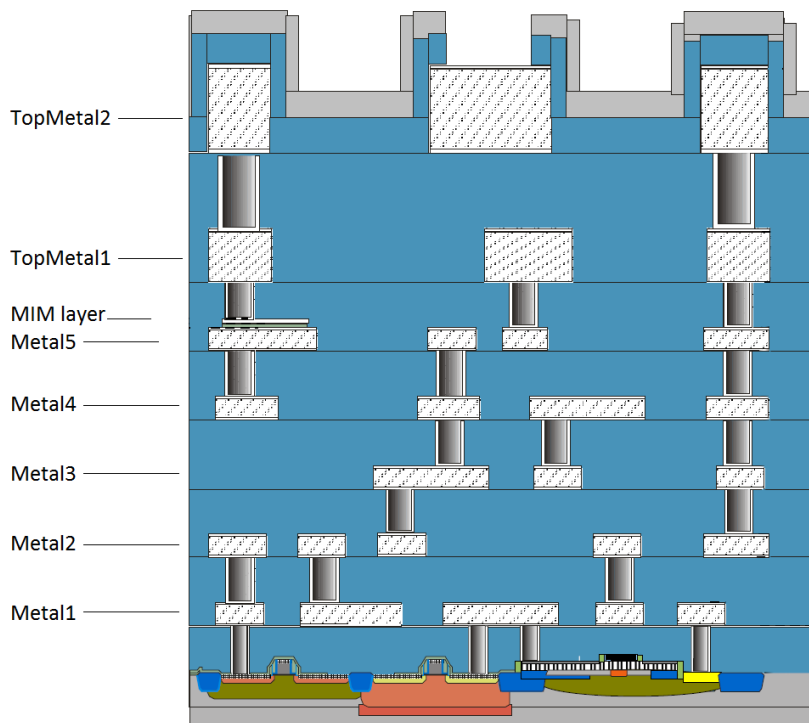


Figure 5.3-1 IHP SG13S stack-up process cross-section

The IHP SG13S PDK library versions used within Microwave Office™ is the rev. 1.0.0.3 and Advanced Design System™ rev. 1.3.1. The SG13S PDK is composed by active and passive parts.

The active part used is the bipolar npn transistor (npn13p12), a high performance device with transition frequency of 250 GHz. The device current for maximum transition frequency is valid for $V_{CE} = 1.2$ V with emitter length from 1 to 2 μm and number of fingers from 1 to 8.

The passive elements are the MIM capacitors (c_{mim}) located MIM layer between Metal5 and TopMetal1 metal layers. Its length and width are scalable in size from 1.14 μm to 1mm.

The passive element inductor (Inductor 2PI) is also scalable through the parameters diameter, trace width, number of turns and spacing between the turns.

The passive element resistors are divided in salicided poly-Si low ohmic resistor (r_{sil}), poly-Si medium resistance (r_{ppd}) and poly-Si high ohmic resistor (r_{high}). All other remaining elements in the PDK library are not going to be used in the design.

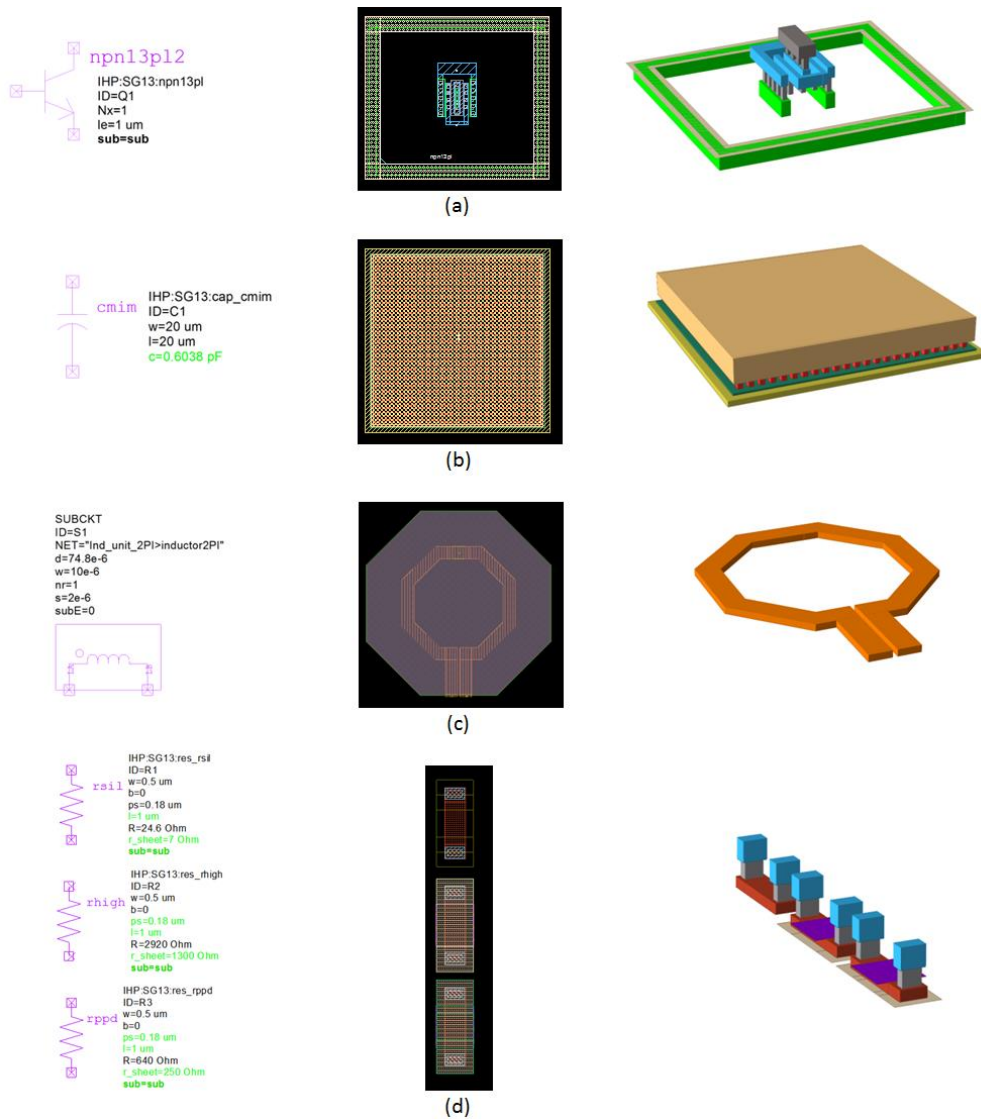


Figure 5.3-2 IHP SG13S active and passives components of the IHP SG13S PDK library. From the top to bottom : (a) the bipolar npn transistor, (b) the MIM capacitor, (c) the inductor and (d) the unsalicided and salicided resistors.

5.4. TRANSISTOR NOISE MODELLING

The modelling of IHP BiCMOS SiGe bipolar junction transistors (BJT's) is based on the HiCUM level 2 and VBIC models. The HiCUM level 2 is a semi-physical and truly charge-based model featuring accurate modelling of the linear and non-linear characteristics, defined by emitter size as well the number and location of base, emitter and collector fingers, scalable from a single set of technology specific electrical and technological data such as width and doping of the collection region, physical data like mobility, transistor dimension, operating point and temperature. The availability and modularity of the HiCUM model enables circuit optimization as well the process variations in the design.

According M. Schroter and A. Chacravorty [33], the main physical and electrical effects encompassed in the HiCUM level 2 are briefly summarized below:

- high-current effects (including quasi-saturation)
- distributed high-frequency model for the external base-collector region
- emitter periphery injection and associated charge storage
- emitter current crowding (through a bias dependent internal base resistance)
- two- and three-dimensional collector current spreading
- parasitic (bias independent) capacitances between base-emitter and base-collector terminal
- vertical non-quasi-static (NQS) effects for transfer current and minority charge
- temperature dependence and self-heating
- weak avalanche breakdown at the base-collector junction
- tunneling in the base-emitter junction
- parasitic substrate transistor
- bandgap differences (occurring in HBTs)
- lateral scalability

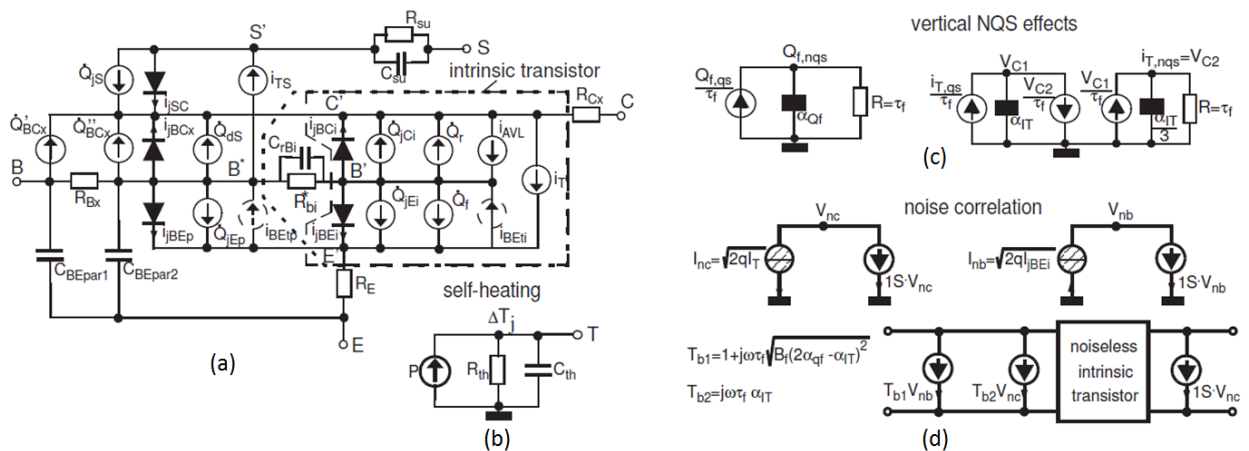


Figure 5.4-1 Large signal HiCUM equivalent circuit (a), thermal network used for self-heating calculation (b), vertical NQS effect (c) and correlated noise (d).

Besides the HiCUM model and its complexity involving the modelling of several parameters, the transistor noise modelling can be simplified to a bipolar junction transistor noise equivalent circuit on which the main parameters such as thermal noise, flicker noise and shot noise arises from the various physical sources illustrated in Figure 5.4-2. The analysis of noise sources in a HBT is very important since it will determine the noise floor and low frequency noise due to the up-conversion in the oscillation process create phase noise. The most important noise sources impacting in the oscillator phase noise from the active parts are thermal noise, shot noise, flicker noise and generation-recombination noise.

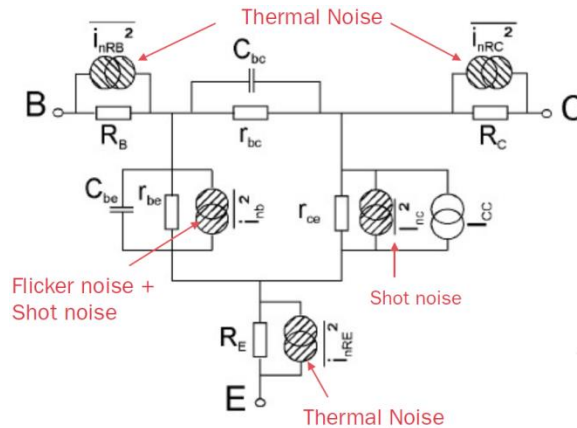


Figure 5.4-2 Bipolar transistor noise equivalent circuit

Thermal Noise

Thermal noise is the electronic noise generated by the thermal agitation of the charge carriers inside an electrical conductor which happens regardless of any applied voltage and has no bias dependence. It is determined by the resistance found in the circuit and its equivalent noise temperature. Thermal noise can be defined as:

$$\left\langle \frac{i_{n,th}^2}{\Delta f} \right\rangle = \frac{4kT}{R} \quad 4.73$$

where R is the circuit resistance and T the equivalent noise temperature (or equivalent noise temperature).

Shot Noise

Shot consists of random fluctuations of the electric current in a DC current which originate due to the fact that current actually consists of a flow of discrete emission of charges across a potential barrier. It is white and frequency independent noise increasing with the bias current. Shot noise can be defined as:

$$\left\langle \frac{i_{n,s}^2}{\Delta f} \right\rangle = 2qI_{DC} \quad 4.74$$

where I_{DC} is the current bias and q ($1.60 \cdot 10^{-19}$ C) the elementary charge.

Flicker Noise

Flicker (1/f) noise occurs in almost all electronic devices and can appear with a variety of other effects, such as impurities in a conductive channel, generation and recombination noise in a transistor due to base current and other factors. It is bias current and frequency dependent. It can be mathematically expressed as:

$$\left\langle \frac{i_{fl}^2}{\Delta f} \right\rangle = \frac{K_f I_{DC}^{A_f}}{f^{F_{fe}}} \quad 4.76$$

where f is the frequency and the flicker noise coefficients K_f , A_f and F_{fe} are used to curve fit measured data.

Generation-Recombination Noise

Generation-recombination (GR)- noise is caused by the fluctuation of number of carriers due to existence of the generation-recombination centers and may appear in transitions between the conduction band and other energy levels in the energy gap, in conduction band or valence band. This type of noise is a function of both temperature and biasing conditions. It can be defined as:

$$\left\langle \frac{i_{nl}^2}{\Delta f} \right\rangle = \frac{K_b I_{DC}^{A_b}}{1 + \left(\frac{f}{f_b}\right)^2} \quad 4.75$$

where I_{DC} is the bias current, K_b and A_b are fitting parameters. The frequency f is related to frequency f_b when GR-centers are activated [12]. This gives the characteristic frequency shape called Lorentzian.

In a bipolar transistor, the thermal noise appears due to the base resistance, shot noise appears due to the junction on the collector and base. Flicker and GR-noise have a dominant low frequency behavior.

According F. Sischka [15] and with respect to the Figure 5.4-2, associated with resistors R_b at base, R_c at the collector and R_e at the emitter, the thermal noise source can be described as following:

$$\overline{i_{R,i}^2} = 4kT \frac{1}{R_i} \Delta f, \quad i = b, c, e \quad 4.76$$

The base and collector currents are considered to be independent factors, thus the shot noise can be described by a source at the base terminal as:

$$\overline{i_{b,s}^2} = 2eI_b \Delta f \quad 4.77$$

and also at the collector terminal

$$\overline{i_{c,s}^2} = \overline{i_{nc}^2} = 2qI_c\Delta f \quad 4.78$$

The total flicker (1/f) noise of the transistor can be described by a noise source in parallel with the base-emitter area. A noise source seen at the base terminal can be described as:

$$\overline{i_{nb}^2} = 2qI_b\Delta f + K_f \frac{I_b^{Af}}{f} \Delta f \quad 4.79$$

The flicker noise, shot noise and GR-noise effects appears in the noise spectrum of the base terminal and can be described according the following equation:

$$\overline{i_{nb}^2} = 2qI_b\Delta f + K_f \frac{I_b^{Af}}{f} \Delta f + K_b \frac{I_b^{Ab}}{1 + \left(\frac{f}{f_b}\right)^2} \quad 4.80$$

5.5. CIRCUIT SIMULATION AND OPTIMIZATION

The circuit simulation and optimization of the oscillator circuits are necessary in order to evaluate the performance of each oscillator type foreseen in 5.2, execute trade-off analyses and afterwards perform circuit optimization in order to obtain the best combination of results. When designing oscillators several goals need to be met, therefore the main trade-offs involving the multidimensional dependencies are:

- Phase Noise
- Output Power
- Harmonics
- Power Consumption

In the case of oscillators employing EBG resonators, there is no tuning range involved, therefore the design is simplified aiming the isolation of the resonator device (when possible) from the rest of other elements in the circuit. This is to ensure the Q-factor achieved is high enough and is not decreased by additional series or parallel components such as capacitors or inductors possessing lower Q-factor. The first assessment to be performed is the trade-off involving the transistor (npn13pl) minimum noise figure (NF_{min}), the maximum available gain (MAG) versus the transistor base current (I_b) and number of emitter fingers (N). A sweep analysis involving those parameters is performed.

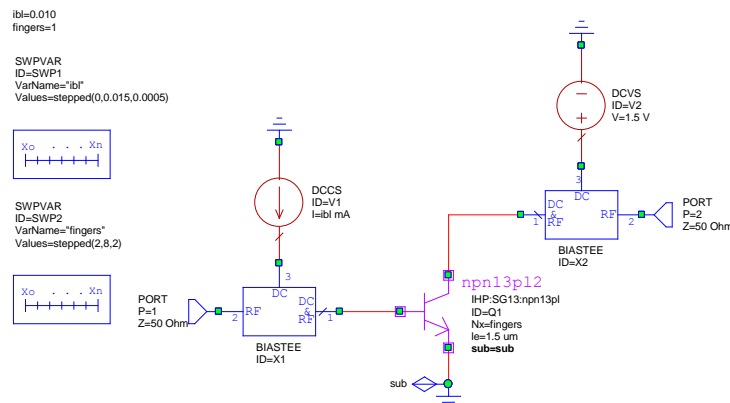


Figure 5.5-1 Sweep analysis of the SG13S npn13pl transistor to evaluate NF_{min} and MAG versus number of emitter fingers and I_b .

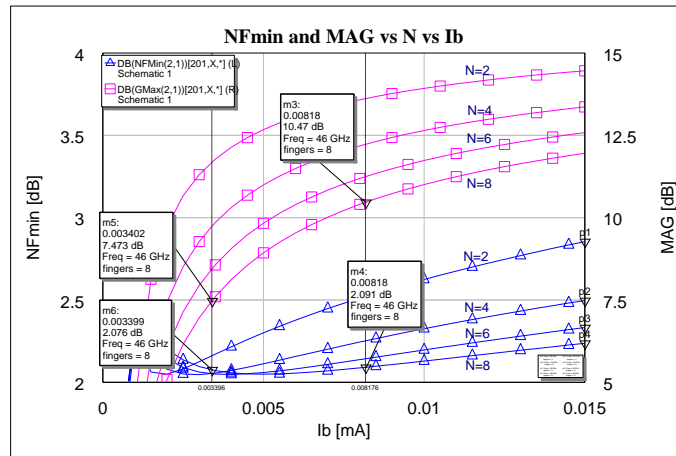


Figure 5.5-2 Plots of NF_{min} and MAG versus I_b and N , $V_{ce} = 1.2 V_{DC}$ and emitter length = $2 \mu m$.

The IHP SG13S process recommends a voltage drop in the junction collector-emitter (V_{ce}) equal to $1.2 V_{DC}$ to obtain best performance and results achieving also high F_T and F_{max} . The emitter length is kept to $2 \mu m$ and the frequency of analysis is 46 GHz. The Figure 5.5-1 shows a circuit composed of the transistor under analysis (npn13pl) connected to ideal bias-tees with a current and voltage sources in the base and collector respectively. The base current is swept from 0 to $15 \mu A$ and the number of emitter fingers swept from 2 to 8, while maintaining $N = 8$ and $V_{CE} = 1.2 V_{DC}$. From figure 5.5-2, it is perceived the minimum noise figure is obtained when increasing the number of emitter fingers operating at low base current. On the other hand, the maximum available gain is obtained when reducing the number of fingers and operating at high base current. Therefore, a trade-off between the minimum noise figure and maximum available gain is established. As starting point, the best compromise for the base current is obtained between 3.4 to $8.5 \mu A$ leading to collector currents between 2.20 mA to 5.51 mA with $N = 8$ and $V_{CE} = 1.2 V_{DC}$. Since the circuits require a higher gain than the resonator losses, a base current toward the high-end values can be adopted for biasing the transistor.

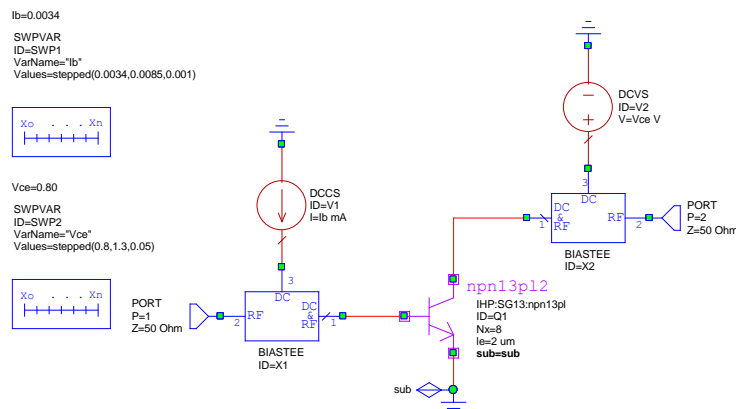


Figure 5.5-3 Sweep analysis of the SG13S npn13pl transistor to evaluate NF_{min} and MAG versus V_{CE} .

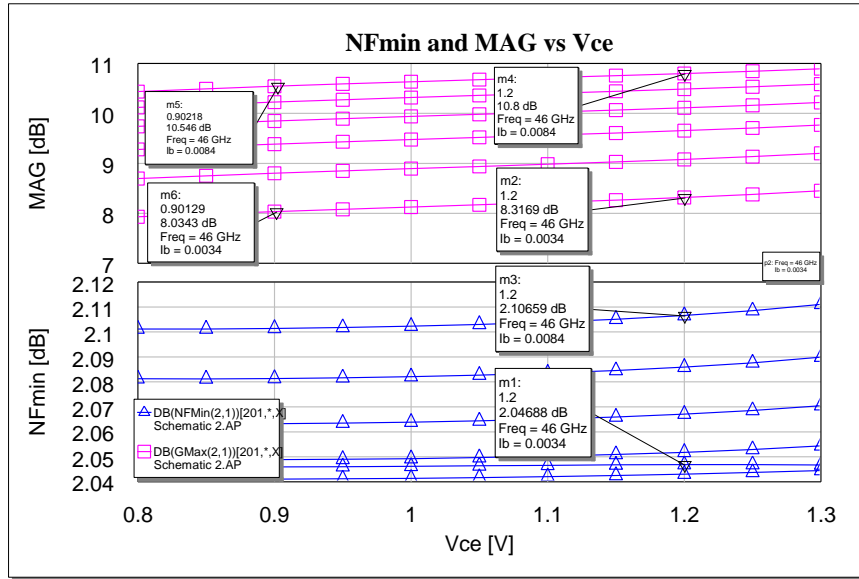


Figure 5.5-4 Plots of NF_{min} and MAG versus V_{CE} , $I_b = 8.2 \mu A$ and emitter length = $2 \mu m$.

In the second assessment, NF_{min} and MAG versus V_{BE} is swept. From figure 5.5-4, it is also perceived there is no expressive variation of NF_{min} versus a V_{CE} (0.8 to 1.3 V_{DC}) and I_b (3.4 to 8.4 μA) sweep, however MAG has increased 2.5 dB with a 5 μA base current increment while maintaining $N = 8$. At $V_{CE} = 1.2 V_{DC}$ and $I_b = 8.4 \mu A$, the minimum noise figure found is 2.10 dB and maximum available gain is 10.8 dB. This translates into the fact the noise figure is not considerably affected by variations in V_{CE} , however MAG increases noticeably with the I_b increment.

The third assessment regards to the compression point (P_{1dB}) of the transistor device, however this analysis is only valid for input power defined at 50 Ω impedance. The input power is swept from -20 dBm to 0 dBm and I_b swept from 3.4 to 10 μA , while maintaining $V_{ce} = 1.2 V_{DC}$ and $N = 8$. Reading the curve $I_b = 8.4 \mu A$, the output P_{1dB} obtained is +4.5 dBm for an input power of -6.5 dBm, thus the gain of the circuit shown in Figure 5.5-4 is 11 dB. This analysis concludes that doubling the base current, the output P_{1dB} increases 2.65 dB, therefore the base current contributes considerably to the compression point of the transistor.

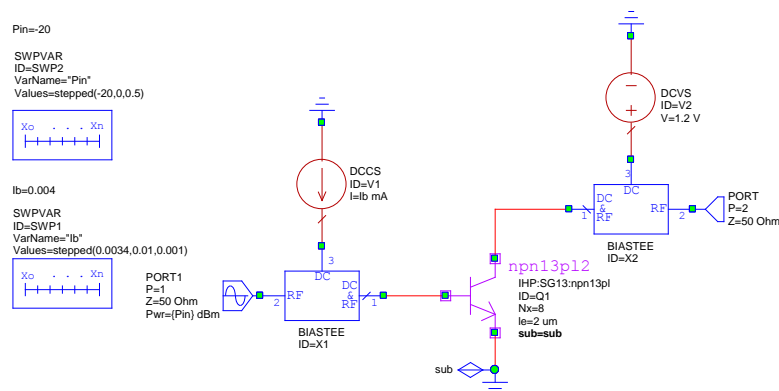


Figure 5.5-5 Sweep analysis of the SG13S $nnp13pl$ transistor to evaluate P_{1dB} versus I_b .

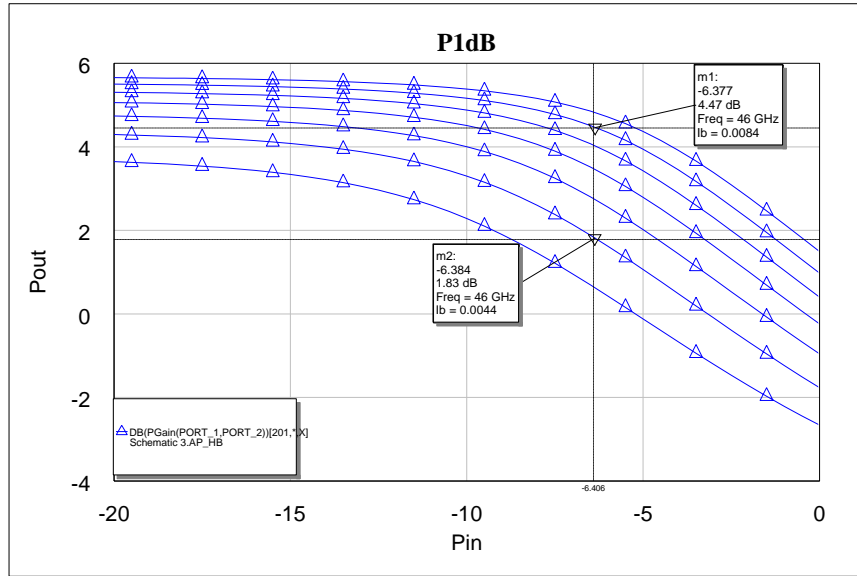


Figure 5.5-6 Plots of P_{1dB} versus I_b , $V_{CE} = 1.2 V_{DC}$ and emitter length = $2 \mu m$.

The fourth assessment relates to the harmonics level in dBc with the transistor amplifier working at compression level. The analysis is only valid for input power defined at 50Ω impedance. The input power is fixed to -6.3 dBm. This level takes the transistor to work in the compression point (P_{1dB}) as reported in Figure 5.5-6, I_b is then swept with two values of 4.4 and $8.4 \mu A$. Figure 5.5-6 show the fundamental signal and its harmonics. The $V_{ce}=1.2$ and $N=8$. With $I_b=4.4 \mu A$, the 2nd harmonic has a suppression level of 14.3 dBc with respect to the fundamental signal, while with $I_b=8.4 \mu A$ the 2nd harmonic level suppression is 20.15 dBc.

The opposite happens with the 3rd harmonic for the two different values of I_b , however the contribution and relevance is lower in this case. In conclusion, biasing the transistor amplifier with $I_b=8.4 \mu A$ seems to be more advantageous in terms of harmonic suppression.

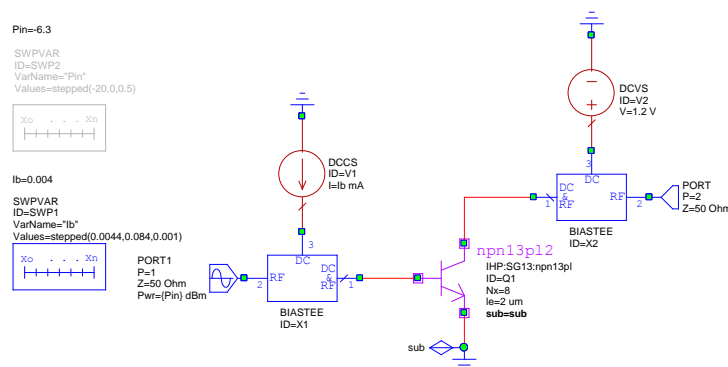


Figure 5.5-7 Sweep analysis of the SG13S npn13pl transistor to evaluate harmonics versus I_b .

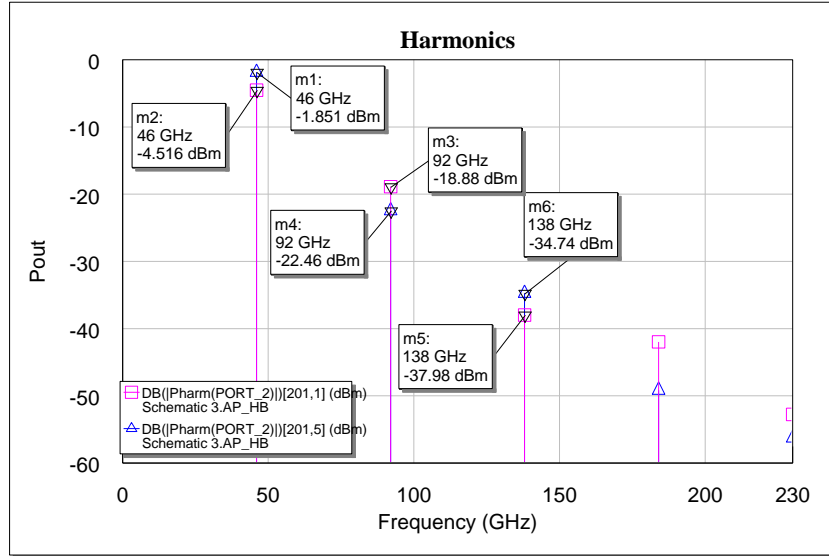


Figure 5.5-8 Plots of output power and harmonics versus I_b , $V_{CE} = 1.2 V_{DC}$ and emitter length = $2 \mu\text{m}$

Feedback Oscillator

It is composed by an amplifier modelled with an input resistance (R_{in}) and output resistance (R_{out}). A block diagram of a feedback oscillator is depicted in Figure 5.1-1 and a simplified schematic is shown in Figure 5.2-1. The resonator in this case is a two-port device that interconnects the output to the input of the amplifier. The tank circuit is ideally composed by a series RLC equivalent circuit with the R_0 represented as loss resistance. The unloaded Q-factor of the resonator is presented in Figure 5.1-4 (b) and equation 4.58. In the analysis of the feedback oscillator, the internal resistances R_{in} and R_{out} are simplified to be the same as the system impedance, Z_0 and the loaded Q-factor in the loop is defined as:

$$Q_L = \frac{\omega L}{R_0 + R_{in} + R_{out}} = \frac{\omega L}{R_0 + 2Z_0} \quad 4.81$$

The ratio between the unloaded and loaded Q-factor can be expressed in terms of coupling factor (β) and defined according:

$$\frac{Q_0}{Q_L} = \frac{R_{loss} + 2Z_0}{R_{loss}} = 1 + \frac{2Z_0}{R_{loss}} = 1 + \beta \quad 4.82$$

Therefore, the voltage drop across the tank circuit can also be defined as following:

$$V_r = V_s \frac{R_0}{R_0 + 2Z_0} = V_s \frac{Q_L}{Q_0} \quad 4.83$$

Assuming maximum available power from the amplifier to be

$$P_{avo} = \frac{V_s^2}{2 \cdot 2Z_0} \quad 4.84$$

The dissipated power inside the resonator will be

$$P_r = \frac{V_r^2}{R_0} = \frac{V_s^2 Q_L^2}{Q_0^2 R_0} = \frac{P_{avo} 4Z_0}{R_0} \left(\frac{Q_L}{Q_0}\right)^2 = 2P_{avo} \frac{Q_L}{Q_0} \left(1 - \frac{Q_L}{Q_0}\right) \quad 4.85$$

In order to achieve the best performance in terms of phase noise, the power in the resonator shall be minimized to create the best signal to noise ratio. The optimum ratio between unloaded and loaded Q-factor is:

$$\frac{Q_L}{Q_0} = \frac{1}{2} \quad 4.86$$

In the case of a feedback oscillator with $R_{in}=R_{out}$, the optimum phase noise can be expressed as following:

$$\mathcal{L}(f_m) = \frac{2FkT}{P_{avp} Q_0^2} \left(\frac{f_0}{f_m}\right)^2 \quad 4.87$$

The feedback oscillator is deployed in the circuit schematics of simulation software Microwave Office™ (MWO).

A first assessment using the active transistor from the PDK and lumped elements of MWO is performed with purpose to provide easy tuning and parameterization of the network.

Once the desired biasing condition and target results are established and consolidated, each of the lumped elements in the circuit is replaced by elements of the PDK.

The elements have their values adjusted and corrected aiming to achieve the same biasing conditions and results already achieved.

Obviously, due to the accuracy of the PDK elements which are modelled to retract imperfections, losses, couplings and self-resonant frequency, the results achieved are degraded compared to those ones obtained with lumped elements.

Figure 5.5-9 shows the schematic circuit for the feedback type oscillator.

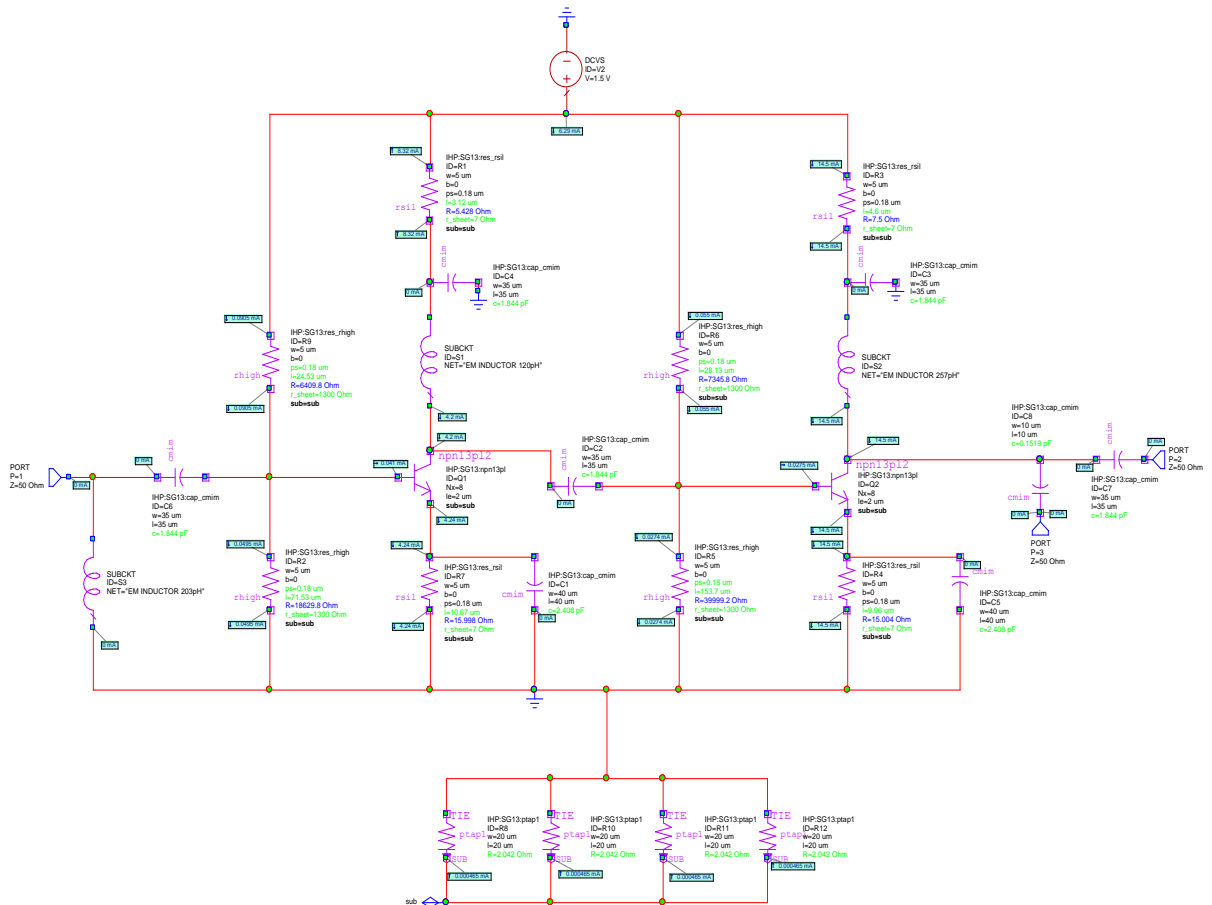


Figure 5.5-9 Schematic circuit of the feedback type oscillator using SG13S PDK elements.

In a real scenario, the resistors at the base terminal of the BJT transistors are replaced by current mirrors. This is to provide stability over temperature avoiding changes in the gain and other characteristics that could affect the performance of the oscillator.

Current mirrors, sometimes called current sinks, are an inverting current buffer in the sense it changes current sources of any impedance into current sinks of high impedance.

Because temperature is a factor in the PN junction of bipolar devices, the two junctions behave identically under all operating conditions.

In Figure 5.5-10 a current mirror circuit is shown, the circuit formed by R_1 and Q_1 elements is designed to copy a current through the active device Q_2 .

Therefore, the current i_1 is adjusted to be equal to $(V_1 - V_{be}) / R_1$. However, process-voltage-temperature (PVT) will not be assessed in this work but the importance of including current mirrors in the oscillator circuit is relevant since parameters such as phase noise are affected by the impedance seen at the base input of the transistor.

The schematic circuit of the feedback type oscillator is then updated with current mirror circuits, parameterized and optimized.

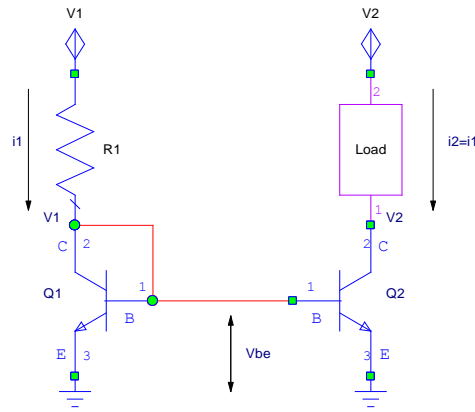


Figure 5.5-10 Current mirror circuit and its operation principle

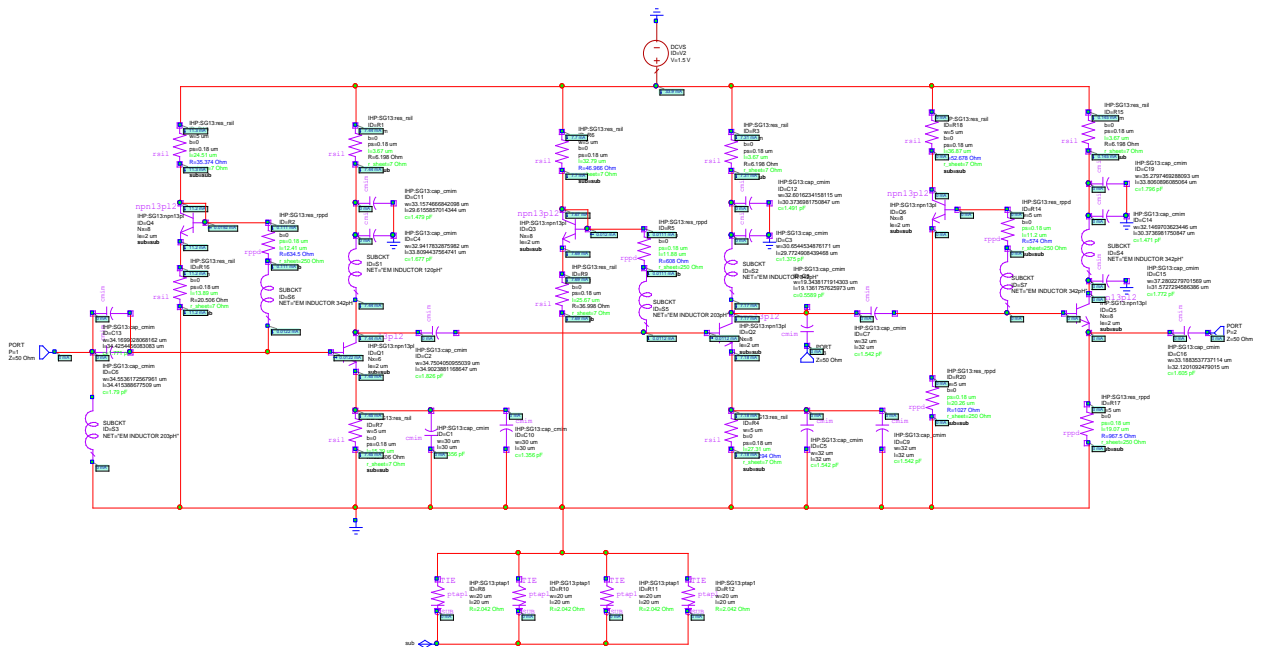


Figure 5.5-11 Schematic circuit of the feedback type oscillator updated with current mirrors.

A verification in the S-parameters of the feedback amplifier circuit shown in Figure 5.5-11 is performed in order to check if the gain (S_{21}) offered by the cascade is sufficiently high to overcome the overall losses in the system which are around -16 dB for the two-port version of the EBG resonator, waveguide filters and probes.

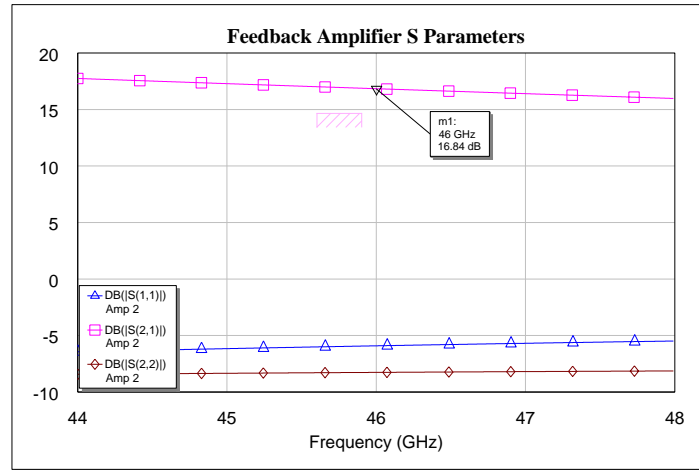


Figure 5.5-12 S-parameters of the feedback type amplifier (version with current mirrors).

Once the gain (S_{21}) of the feedback amplifier is verified the next step is to determine the loop gain in the oscillator design and break the feedback loop of the oscillator in the forward direction, at the fundamental frequency. This is done by using the element OSCTEST from MWO illustrated in Figure 5.5-13. When this is performed, a source signal at port 3 is used to replace the feedback signal and the feedback itself is measured at port 4. This allows to determine the open-loop gain of the circuit under large signal conditions.

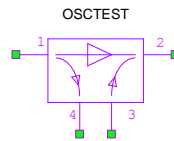


Figure 5.5-13 Element OSCTEST from MWO software used to determine the conditions for oscillation in a circuit.

The element OSCTEST is used to find the oscillation conditions (gain and phase) for any type of oscillator. A large signal is applied to port 1, and the large signal S_{21} , at the fundamental frequency is observed. When the excitation is small, $|S_{21}|$ must be greater than unity, or the circuit will not oscillate. As the excitation level is increased, $|S_{21}|$ decreases as the circuit enters saturation, and at some frequency and some excitation level, $|S_{21}| = 1$ and its phase is zero. This point corresponds to the oscillation frequency, and the output power under these conditions is the oscillator's output power.

The complete block diagram of the feedback amplifier connected to the EBG resonator network and OSCTEST element is depicted in Figure 5.5-14. The full S-parameters file from the measured EBG resonator and waveguide elements was used in combination with the circuit in the circuit simulator. This block diagram will allow to check for the oscillation conditions for the complete network.

The conditions for the oscillator are that the gain (S_{21}) must be higher than 0 dB and S_{21} phase crossing at zero degrees. The conditions are satisfied and shown in Figure 5.5-15.

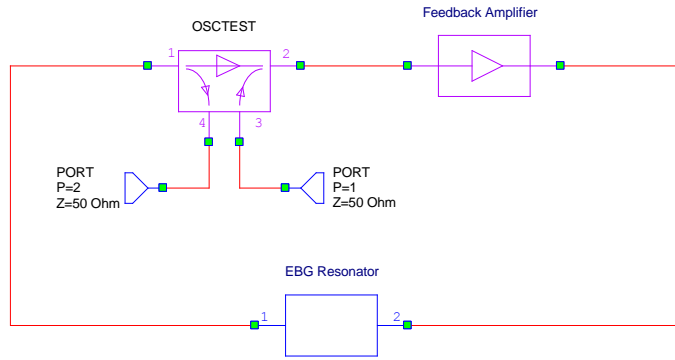


Figure 5.5-14 Element OSCTEST used to determine the conditions for oscillation in a circuit.

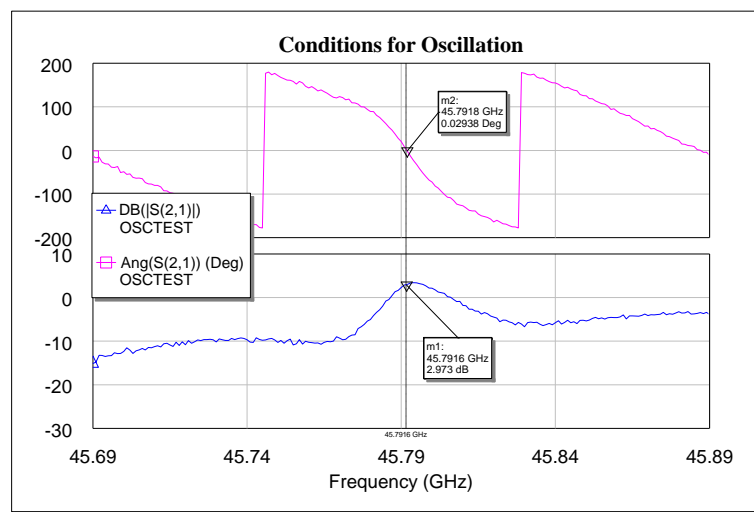


Figure 5.5-15 Conditions for oscillation, S_{21} gain > 0 dB and S_{21} phase at zero crossing.

The following step is to perform a non-linear analysis connecting an oscillator probe to determine the amplitude and frequency that results in zero current flow through the element. OSCAPROBE is an ideal source in series with an ideal impedance element. The impedance presents an open circuit at all frequencies other than the fundamental frequency of oscillation. The element OSCPROBE from MWO is illustrated in Figure 5.5-16.

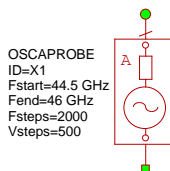


Figure 5.5-16 Element OSCAPROBE from MWO to find amplitude and frequency of oscillation.

Suppose a sinusoidal voltage source of amplitude V and frequency ω_p is applied to an oscillator in steady state at a node between the resonator and the amplifier circuit. The source impedance is given by:

$$Z(\omega) = \begin{cases} 0 & \text{for } \omega = \omega_p \\ \infty & \text{for } \omega \neq \omega_p \end{cases} \quad 4.88$$

The element OSCAPROBE acts as a short circuit at the specified frequency of oscillation and an open circuit at all other frequencies. The voltage amplitude and phase is adjusted until no current flows through the probe, under which conditions the correct oscillating amplitude is determined. The amplitude is then used in a non-linear simulation of the oscillator circuit. This allows output waveforms, harmonics and phase noise of the oscillator to be determined.

The criteria of solving for an oscillator steady-state operation are:

- Connecting the oscillator probe between the EBG resonator and feedback amplifier
- Finding the amplitude and frequency of the probe

In this way, the oscillator analysis is reduced to standard HB analysis running in the inner loop that attempts to locate the probe parameters (amplitude and frequency) that result in a zero-current flow through its terminals. Figure 5.5-17 shows how the element OSCAPROBE is connected between the EBG resonator network and feedback amplifier. The results of phase noise and frequency spectrum will be shown and detailed in Chapter 6.

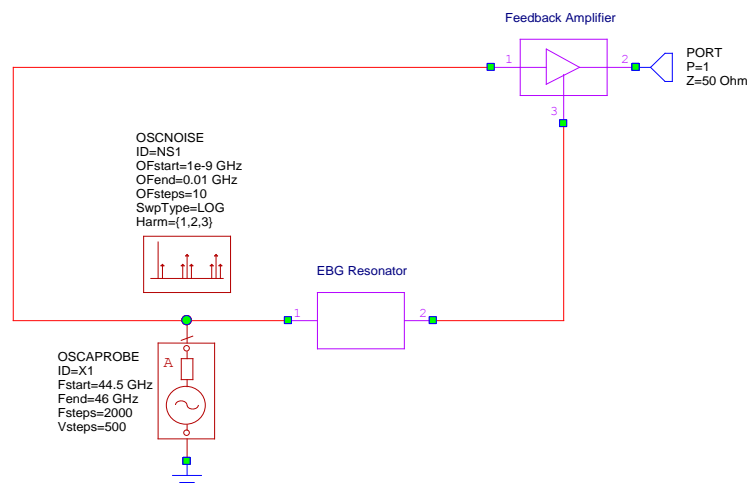


Figure 5.5-17 The element OSCAPROBE introduced between the EBG resonator network and the feedback amplifier.

Negative Resistance Oscillator

A block diagram of a negative resistance oscillator is depicted in Figure 5.1-2 and a simplified schematic is shown in Figure 5.2-2. The active device is a one-port device with a reflection coefficient $\Gamma_A > 1$. The resonator connected to the active device is also one-port device with a reflection coefficient Γ_R . The unloaded Q-factor of the resonator is presented in Figure 5.1-4 (b) and equation 4.58, and the loaded Q-factor as a function of the coupling factor defined as:

$$\frac{Q_0}{Q_L} = \frac{R_{loss} + 2Z_0}{R_{loss}} = 1 + \frac{2Z_0}{R_{loss}} = 1 + \beta \quad 4.89$$

According J. Everard [16], the single-side band noise spectrum for a negative resistance type oscillator can be expressed as:

$$\mathcal{L}(f_m) = \frac{FkT}{8(Q_0)^2 \left(\frac{Q_L}{Q_0}\right)^2 \left(1 - \frac{Q_L}{Q_0}\right)^2 P_{avo}} \left(\frac{f_0}{f_m}\right)^2 \quad 4.90$$

A general equation, written below, describes the three cases:

$$\mathcal{L}(f_m) = A \frac{FkT}{8(Q_0)^2 \left(\frac{Q_L}{Q_0}\right)^2 \left(1 - \frac{Q_L}{Q_0}\right)^n P} \left(\frac{f_0}{f_m}\right)^2 \quad 4.91$$

- 1) $N = 1$ and $A = 1$ if P is defined as P_{RF} and $R_{out} = 0$
- 2) $N = 1$ and $A = 2$ if P is defined as P_{RF} and $R_{out} = R_{in}$
- 3) $N = 2$ and $A = 1$ if P is defined as P_{avo} and $R_{out} = R_{in}$

Substituting the equation 4.90 in 4.91, the single-side band phase noise can be expressed as:

$$\mathcal{L}(f_m) = \frac{FkT}{8(Q_0)^2 \frac{\beta}{(1 + \beta)^3} P_{RF}} \left(\frac{f_0}{f_m}\right)^2 \quad 4.92$$

The minimum noise occurs when $Q_L/Q_0 = 2/3$ or $\beta = 1/2$. The power dissipated in the resonator $P_r = 2/3 P_{rf}$ and substituting it in 4.92, gives:

$$\mathcal{L}(f_m) = \frac{9FkT}{16P_r Q_0^2} \left(\frac{f_0}{f_m}\right)^2 \quad 4.93$$

Those results are easily demonstrated graphically as shown in Figure 5.5-18. The noise variation with ratio of Q_L/Q_0 is demonstrated through an oscillator where the power is defined as P_{rf} .

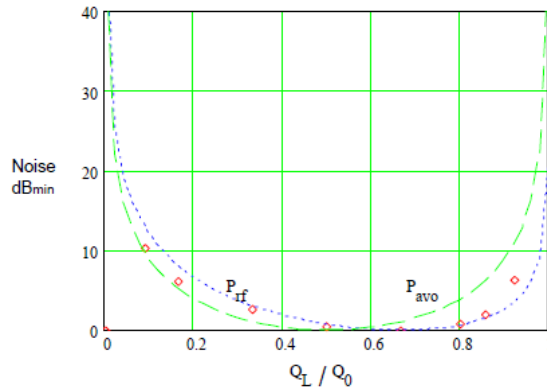


Figure 5.5-18 Phase noise versus Q_L/Q_0 for the two definitions of power

In the same manner as the previous design, the negative resistance oscillator is deployed in the circuit schematics of simulation software Microwave Office™ (MWO). A first assessment using the active transistor from the PDK and lumped elements of MWO is performed with purpose to provide easy tuning and parameterization of the network. Once the desired biasing condition and target results are established and consolidated, each of the lumped elements in the circuit is replaced by elements of the PDK. The elements have their values adjusted and corrected aiming to achieve the same biasing conditions and results already achieved. Obviously, due to the accuracy of the PDK elements which are modelled to retract imperfections, losses, couplings and self-resonant frequency, the results achieved are degraded compared to those ones obtained with lumped elements. Figure 5.5-19 shows the schematic circuit for the negative resistance type oscillator and Figure 5.5-20 the updated version with a current mirror implementation.

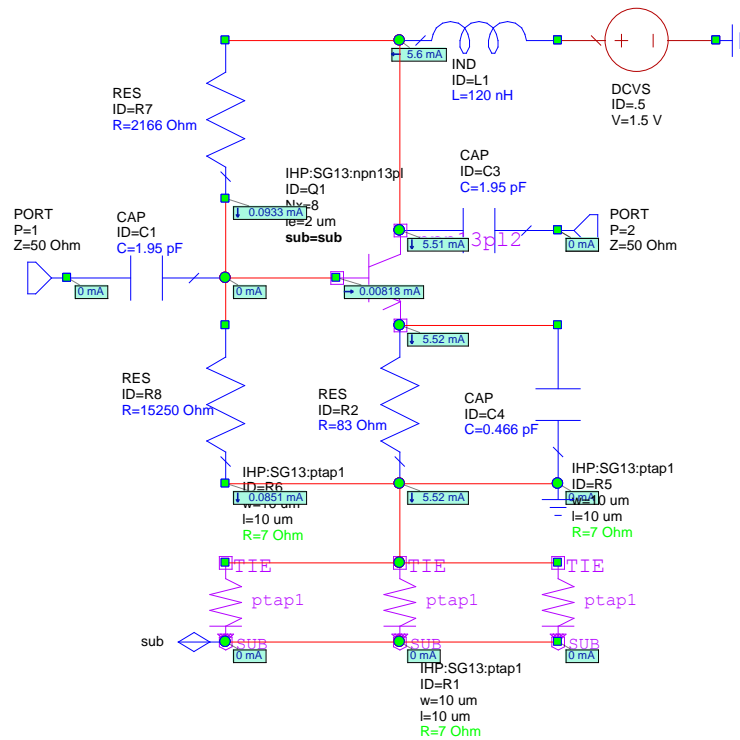


Figure 5.5-19 Schematic circuit of the negative resistance type oscillator using SG13S PDK elements.

The schematic circuit is updated, replacing the resistors at the base terminal of the transistor by a current mirror circuit. The circuit has been also parameterized and optimized as in the previous oscillator design, the current mirror aims to provide stability over temperature and in a real scenario it can change the impedance seen at the base of the transistor that can degrade the overall phase noise of the oscillator. Therefore adjustment in the components of the circuit are necessary to obtain the best results in terms of performances.

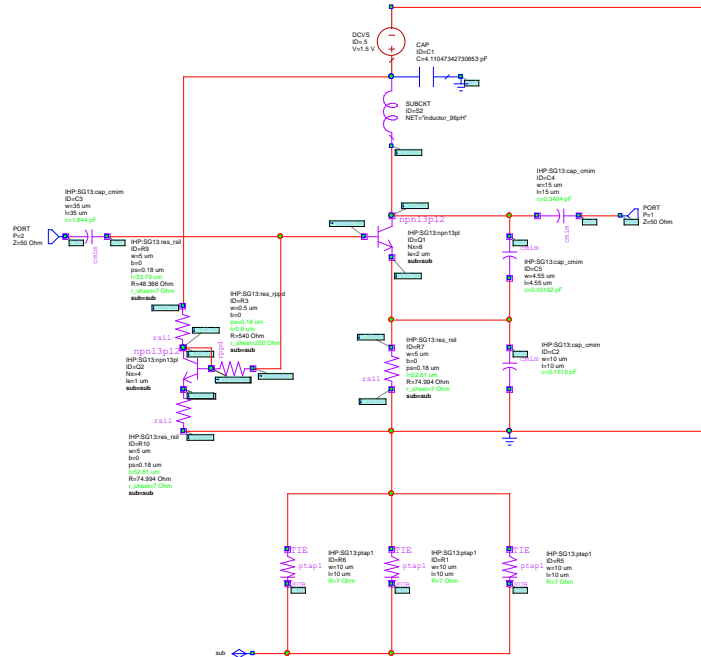


Figure 5.5-20 Schematic circuit of the negative resistance oscillator updated with a current mirror.

A verification in the S-parameters of the negative resistance amplifier circuit shown in Figure 5.5-21 is performed in order to confirm a positive gain (S_{21}). In this reflection oscillator configuration the gain shown does not represent a parameter that should overcome the losses of the resonator network; instead the product between the reflection coefficients of the resonator and amplifier must be greater than the unity.

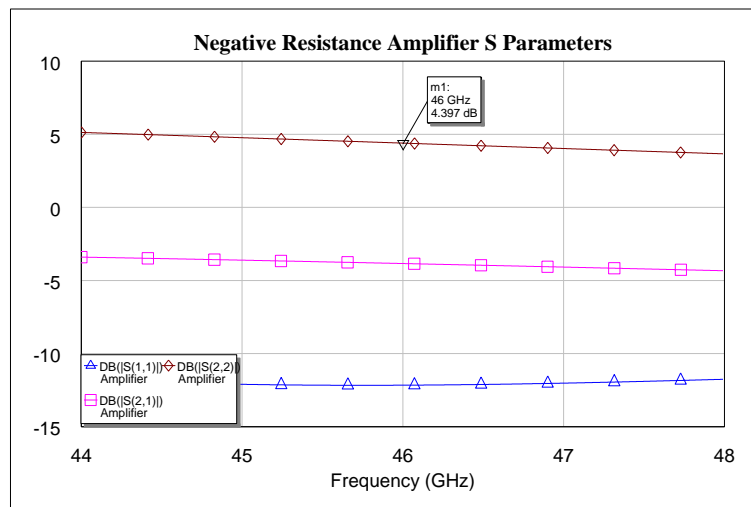


Figure 5.5-21 S-parameters of the negative resistance oscillator (version with current mirror).

After the gain (S_{21}) of the negative resistance amplifier is verified, the same conditions for the oscillation criteria using the element OSCTEST described before are applied. The full S-parameters file from the measured EBG resonator and waveguide elements was used in combination with the circuit in the circuit simulator.

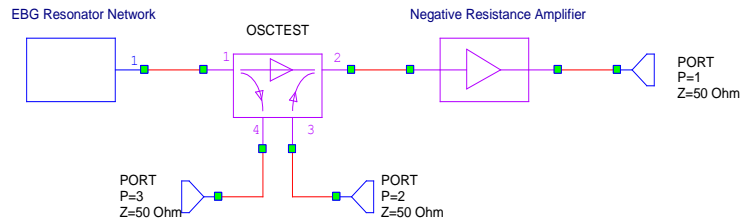


Figure 5.5-22 Element OSCTEST used to determine the conditions for oscillation in a circuit.

Figure 5.5-23 shows the conditions for the oscillation in the negative resistance oscillator.

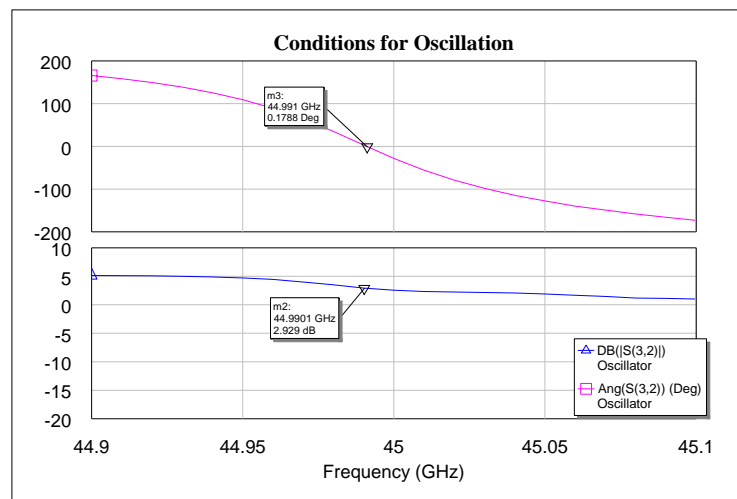


Figure 5.5-23 Conditions for oscillation, S_{21} gain > 0 dB and S_{21} phase at zero crossing.

The following step is to perform a non-linear analysis connecting an oscillator probe OSCAPROBE already detailed before to determine the amplitude and frequency that results in zero current flow through the element. The results of phase noise and frequency spectrum will be shown and detailed in Chapter 6.

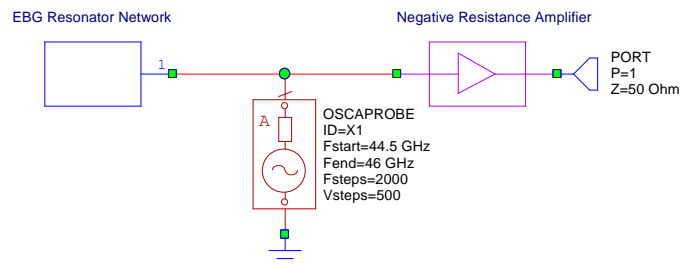


Figure 5.5-24 The element OSCAPROBE introduced between the EBG resonator network and the negative resistance amplifier.

Both oscillator circuits were parameterized and optimized after the replacement of passive lumped elements from the AWR software library by the ones from the SG13S PDK, as well the replacement of the resistors at the base terminal of the transistor(s) by current mirror(s).

The parameterization consists into establishing lower and upper limits as well the step size for the components values. This includes resistors, capacitors, inductors and transistor number of emitter fingers and emitter length. Figure 5-5.25 shows an example of the properties of a transistor and resistor from the SG13S PDK. As it can be seen, the options of Tune (parameterization) and Opt (optimization) are enabled with their respective lower and upper limits as well the step size. By creating target parameters and goals for optimization, for example, those elements will be automatically adjusted to find the best combination of results for the desired targeted parameters.

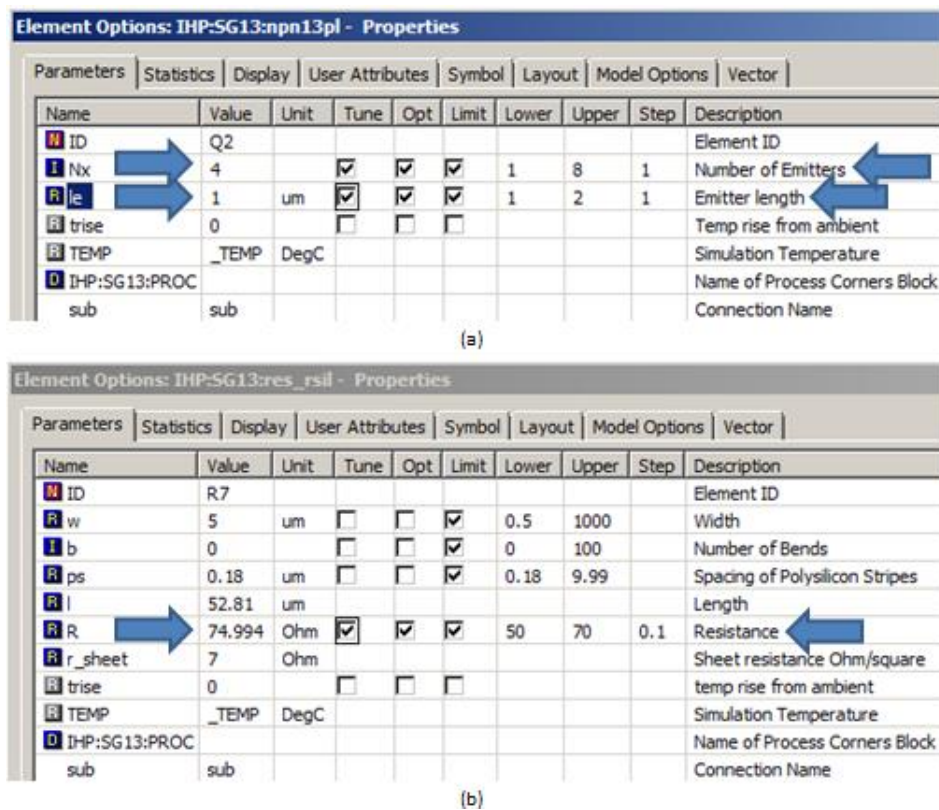


Figure 5.5-25 SG13S element properties and their respective adjustable parameters. In (a) the properties of the transistor npn13pl such as number of emitters and emitter length, in (b) the properties of the resistor rsil like the resistance.

In the same manner, the target parameters and goals are defined by the user with a range of frequency and values to be optimized. Figure 5.5-26 shows an example of optimization goal for the SSB phase noise, the respective frequency range and desired goal.

During optimization, the circuit is analyzed at each frequency in the project frequency list, so minimizing the number of analysis frequencies makes the optimization proceed very rapidly. In a narrowband circuit, it is often adequate to use only the band-edge frequencies, and even in broader circuits it is rarely necessary to use more than a few frequency points.

The optimization function consists of several algorithm methods depending on the number of variables and complexity of the circuit.

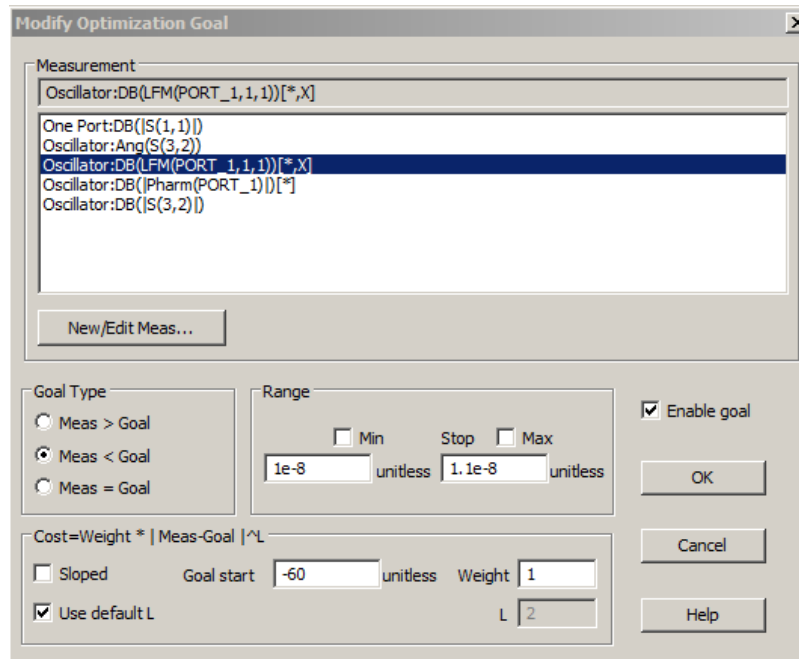


Figure 5.5-26 Window of optimization goals showing the goal parameter list and their respective range of frequency and goal start.

The main parameters under optimization are the SSB phase noise and amplitude of the fundamental signal. The SSB phase noise have goals defined to obey 30 dB/Decade from 10 Hz until the flicker corner, and then 20 or 10 dB/Decade from the flicker corner until it reaches the noise floor. At the same time, the amplitude of the fundamental signal is optimized targeting high levels in dBm. Last, the optimizer method is chosen with option to specify the maximum number of iterations while windows of relative cost and history are displayed. In addition, the user can also control which are the variables under constrain that eventually can be extended to achieve the goals.

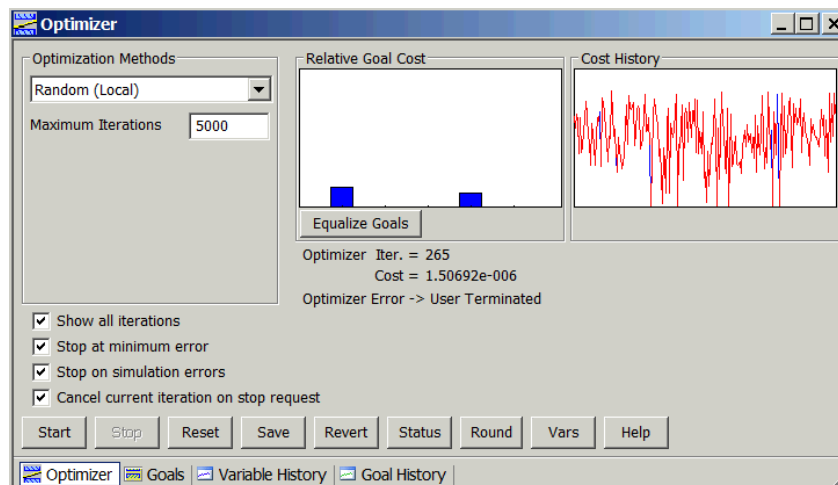


Figure 5.5-27 Window of the optimizer feature showing relative cost and history of the goals.

5.6. LAYOUT (MMIC) AND ELECTROMAGNETIC ANALYSIS

The MMIC layout for the feedback and negative resistance type oscillators are displayed in Figures 5.6-1 and 5.6-2. The chip sizes are 1200 x 600 μm and 640 x 640 μm respectively.

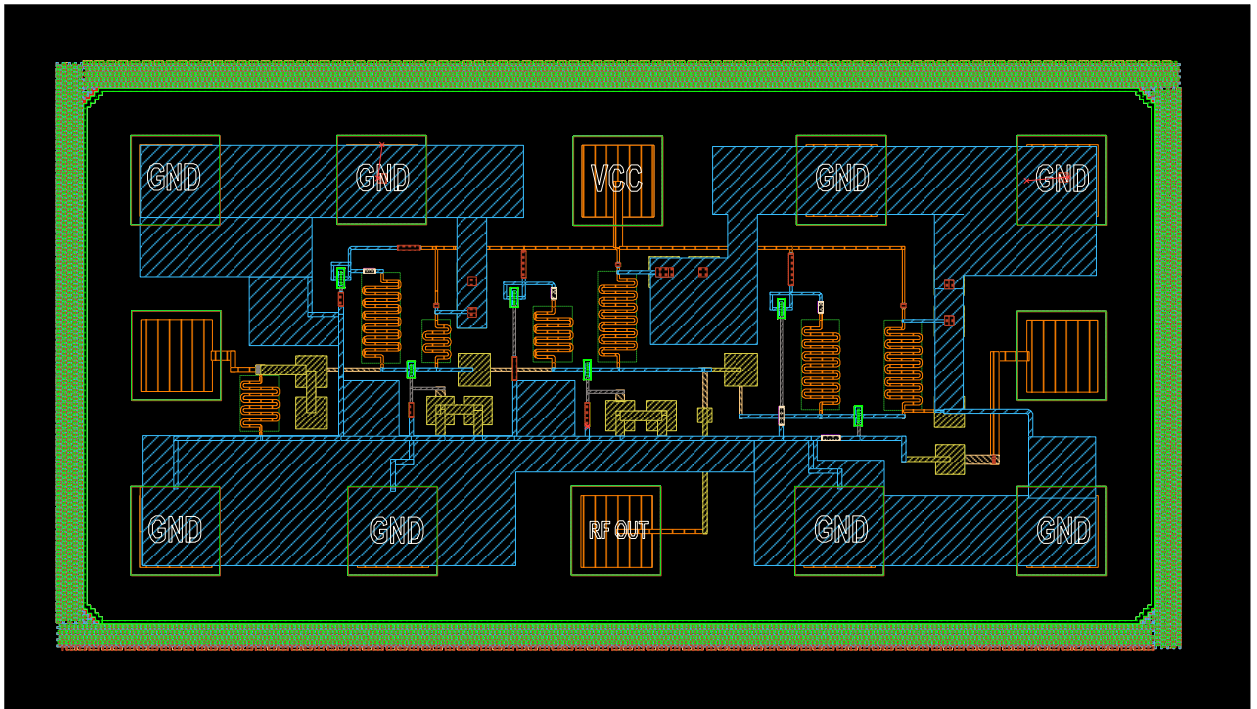


Figure 5.6-1 MMIC Layout of the feedback type oscillator (chip size 1200 x 600 μm).

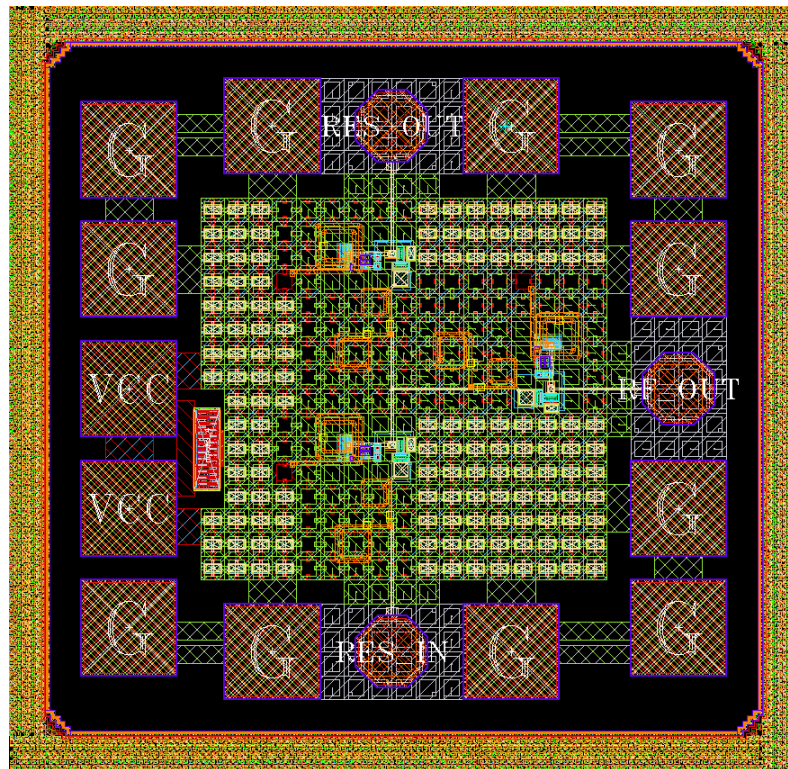


Figure 5.6-2 MMIC Layout of the negative resistance type oscillator (chip size 640 x 640 μm).

5.7. WAVEGUIDE PROBE AND BAND-PASS FILTER

This chapter discusses the necessary lossy transmission lines, probes and filter blocks that interconnect the resonator structure to the oscillator circuit.

The objective of aiming good results in terms of phase noise is to minimize the overall losses in the system by employing proper technique and selecting low loss conducting materials, avoid excessive electrical length of transmission line as well as minimizing impedance transitions.

In order to obtain a realist result in terms of phase noise, all the losses in the systems are accounted for and computed such as the oscillator at layout level and its respective bond-pads, bond-wires, waveguide probes, waveguide filters and the resonator itself.

All structures modelled under the simulation environment are composed of lossy and dispersive material. In Figures 5.7-1 and 5.7-2 the complete block diagrams of the two-port oscillator and one-port oscillator are presented.

The complete oscillator system is based on a MMIC oscillator circuit which is connected to the waveguide E-probes via bond wires. The E-probes are back-shorted and located at optimum distance inside of the rectangular WR-19 waveguide. The energy travels from and to the waveguide passing through the waveguide band-pass filters and finally connected to the EBG resonator tapers. The complete system is embedded inside of the metallic test-fixture structure.

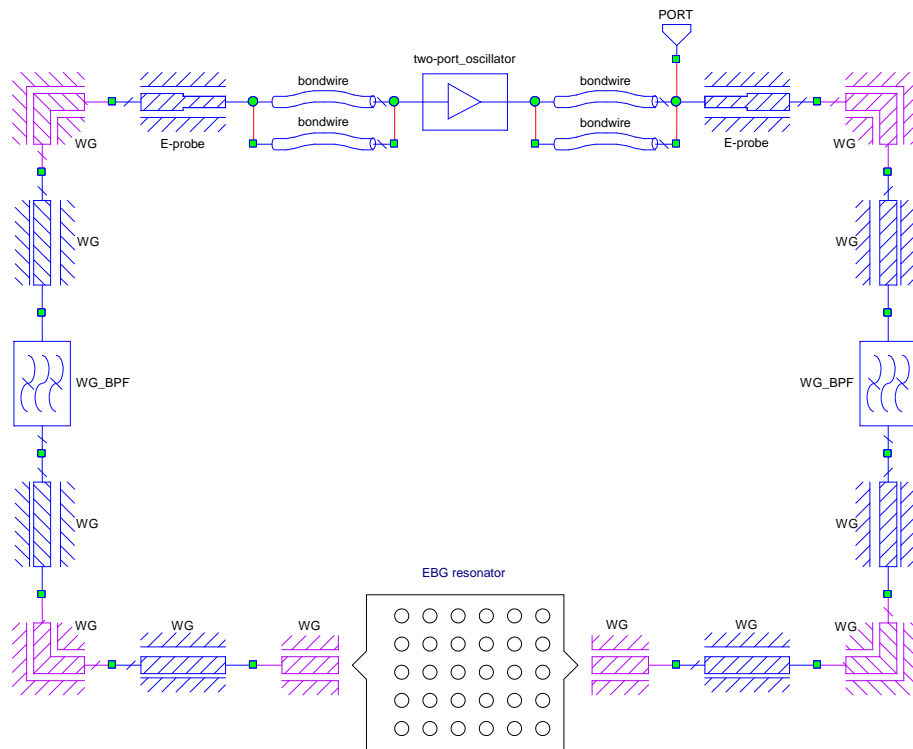


Figure 5.7-1 Complete block diagram of the two-port oscillator system embedded in the test-fixture.

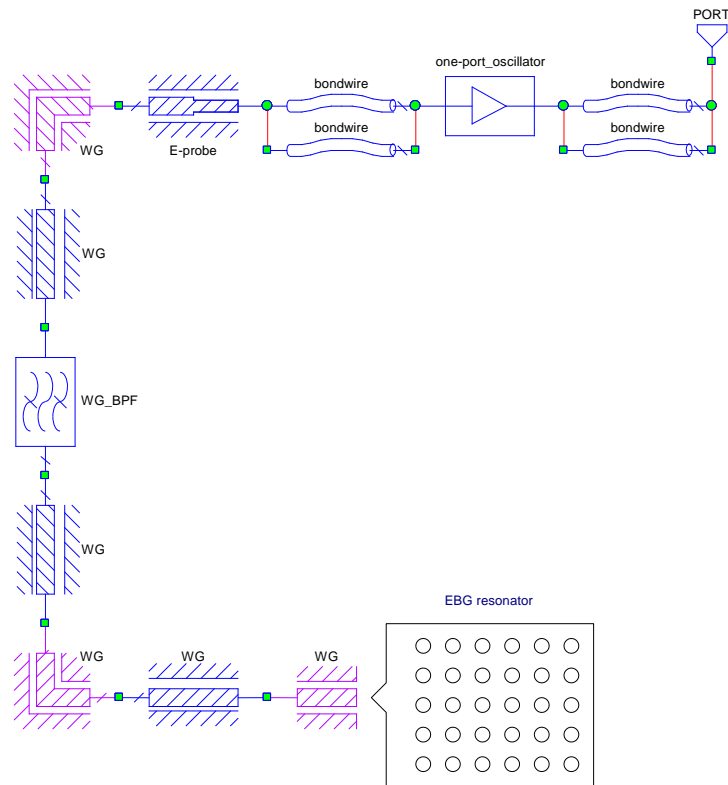


Figure 5.7-2 Complete block diagram of the one-port oscillator system embedded in the test-fixture.

The following analyses are composed by a break-down of the individual pieces of transmission lines followed by an assessment and evaluation of the overall losses and filtering capabilities in the system.

Waveguide E-Probe

Waveguides are usually fed using coaxial lines or through quasi-TEM modes such as microstrip co-planar transmission lines. When a sensing probe is inserted in the waveguide and excited with energy it acts like a quarter-wave antenna.

The current flows in the probe and sets up an E-field as shown in Figure 5.7-3. The E-field lines flow out from the probe and couple to the waveguide.

The purpose of the E-field field probe is convert TEM mode of MMIC circuit input and output pads into TE mode of the waveguide and vice-versa in order to couple energy within the EBG resonator.

The waveguide E-field probe is inserted into the WR-19 waveguide and located in the center of “a” and parallel to “b” waveguide wall dimensions and a quarter-wave (back-shorted) from the end of the waveguide wall as shown in Figure 5.7-3. This is the location where the E-field is maximum in the dominant mode.

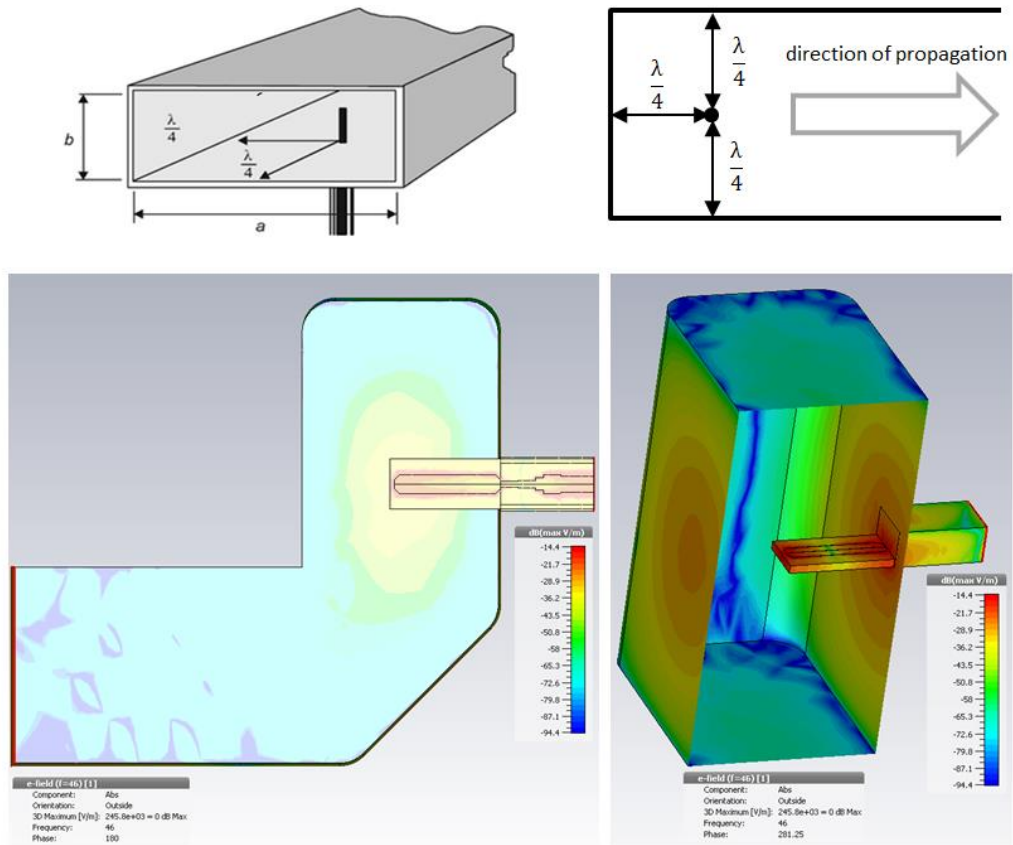


Figure 5.7-3 Above the concept of waveguide probe and its optimum distances for maximum E-field in the dominant mode. Below the cut-plane views of electric-field flowing through the probe and waveguide.

In Figure 5.7-5, the left upper corner shows the E-field probe inserted in the WR-19 waveguide and the tetrahedral meshing used in the frequency domain solver. The right upper corner shows the E-field probe back-shorted at a quarter-wave distance from the waveguide wall as well the parameters used during the optimization process. In the left and right down corners the optimized results of input return loss (S_{11}) at probe input and forward transmission coefficient (S_{21}) from the probe to the end of waveguide.

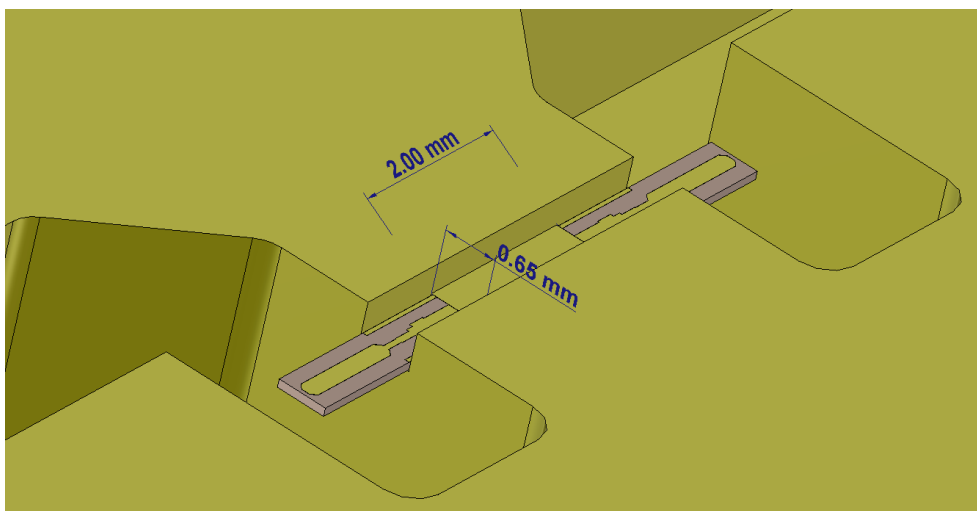


Figure 5.7-4 Details of the waveguide E-probes inside the test-fixture

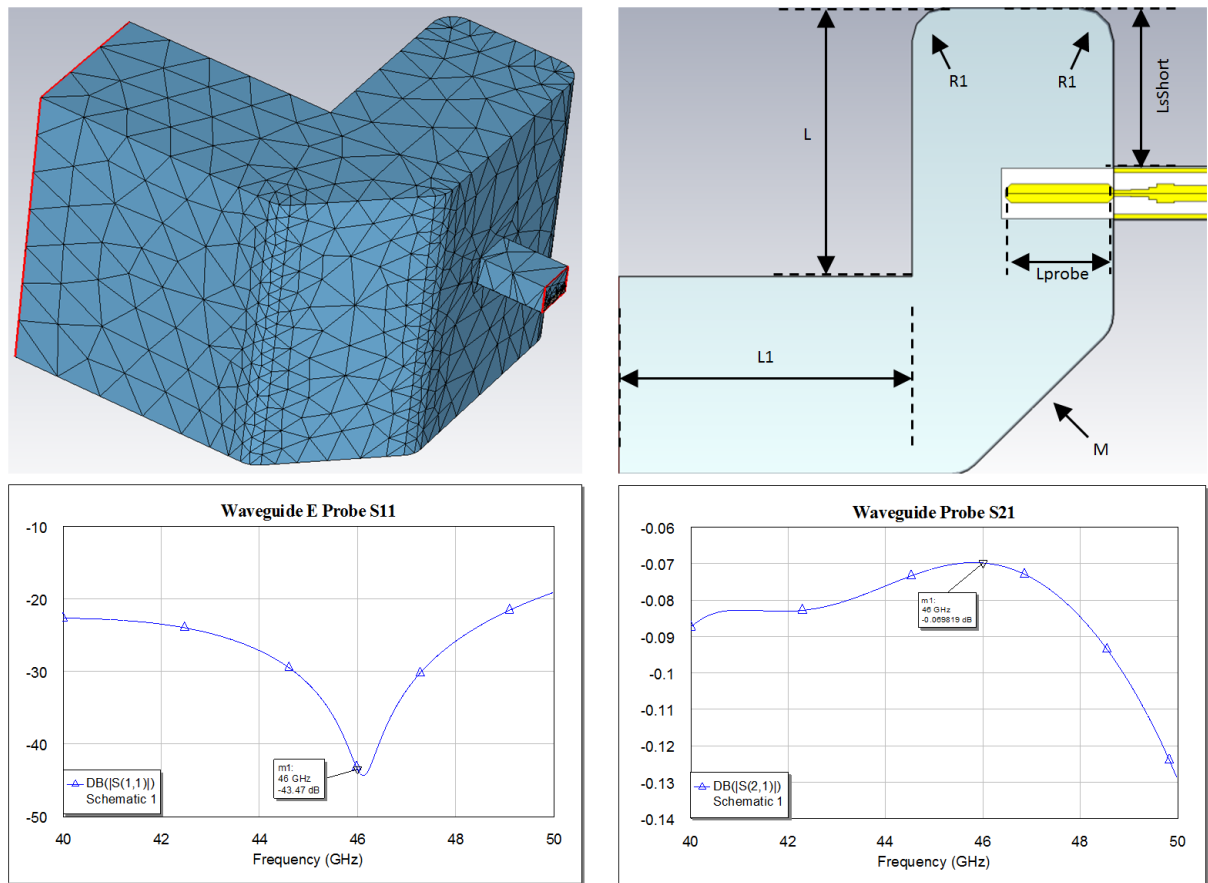


Figure 5.7-5 Waveguide E-field probe back-shorted at quarter-wave distance from the waveguide wall and its parameters used in the optimization process. Below the optimized results of input return loss (S_{11}) and forward transmission coefficient (S_{21}).

Table 5.7-1 below retracts all parameters investigated in the parameterization and optimization process of the E-field probe.

The probe horizontal and vertical lengths, waveguide curve chamfers and edges as well the distance from the probe to the waveguide wall were parameterized and then optimized to provide low loss centered at 46 GHz.

The waveguide probe is composed by a quarter-wave microstrip line followed by a transformer to match the port to 50Ω impedance system at 46 GHz center frequency. The material used to predicting the electrical performance of the waveguide probe is a lossy gold microstrip line with electric conductivity of 4.561×10^7 [S/m] seated over a low loss quartz substrate with electric permittivity of 3.75 and tangent loss equal to 1×10^{-4} .

The background properties for the waveguide walls are composed by a lossy metal (gold) with electric conductivity of 4.561×10^7 [S/m] and filled with vacuum at the interior.

The rounded corners of the internal waveguide walls were designed and optimized foreseeing its fabrication ready for milling machine process instead of mitered corners.

Name	Expression	Value	Description	Type
Center	= 0	0	Probe center	Length
R1	= .4	.4	Curve edges	Length
L	= 1	1	Probe vertical length	Length
Lprobe	= 1.27854	1.27854	Probe length	Length
M	= 1.762952477788	1.762952477788	Probe chanfer	Length
Lshort	= 1.9157472768783	1.9157472768783	Probe LsShort	Length
L1	= 5.884	5.884	Probe horizontal length	Length
Fmin	= 40	40	Minimum start frequency	Frequency
Fmax	= 50	50	Maximum stop frequency	Frequency

Table 5.7-1 The parameter list of variables used in the optimization process of the E-probe size and distance to the waveguide walls.

Band-Pass Filters

Waveguide band-pass filters were designed to be included afterwards within the test-fixture and resonator structure. The purpose is to attenuate the transmission peaks outside the desired resonance which eventually could cause the circuit to fail in find the correct solution in terms of oscillation due to multiple resonances, therefore assuming a chaotic behavior.

The design includes two identical waveguide band-pass filters with five sections each, however with frequency response characteristics slight differently from one another in order to improve the overall out-of-band attenuation. They are named low-band filter and high-band filter and their aspect are displayed in Figure 5.7-6. In the initial simulations, the background properties for the waveguide filters walls are composed by a lossy metal (gold) with electric conductivity of 4.561×10^7 [S/m] and filled with vacuum at the interior. The rounded corners of the internal waveguide walls were designed and optimized foreseen its fabrication ready for milling machine process, instead of mitered corners.

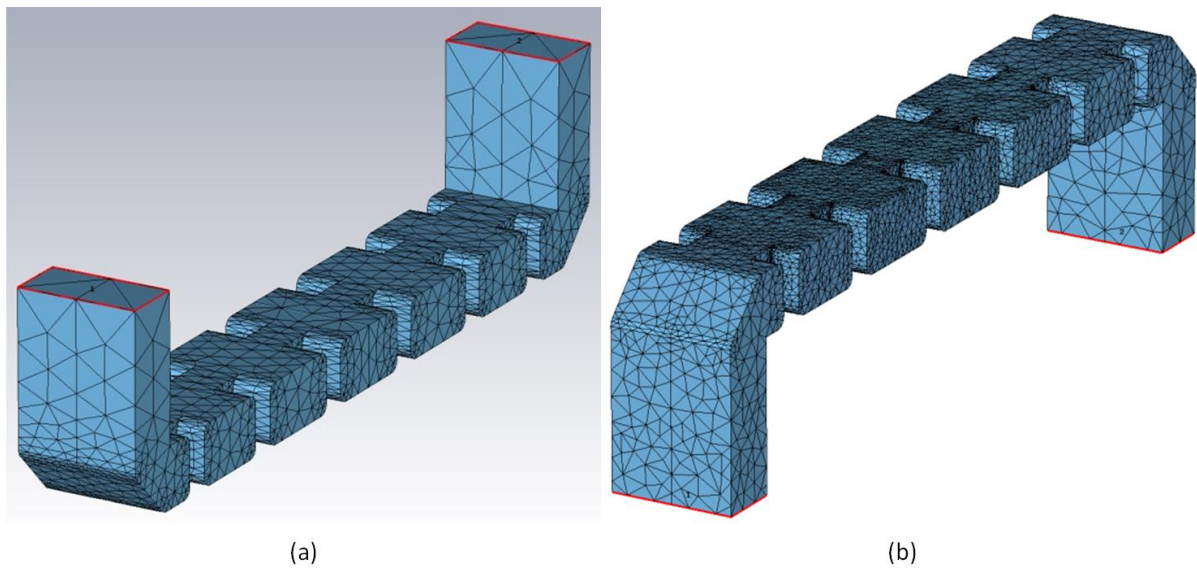


Figure 5.7-6 Waveguide band-pass filters. In (a) the low-band filter and (b) the high-band filter with frequency response slightly different from one another.

The response of the waveguide band-pass filters is depicted in Figure 5.7-7. In the blue and red curves, the forward transmission coefficient (S_{21}) of the low-band and high-band filters respectively.

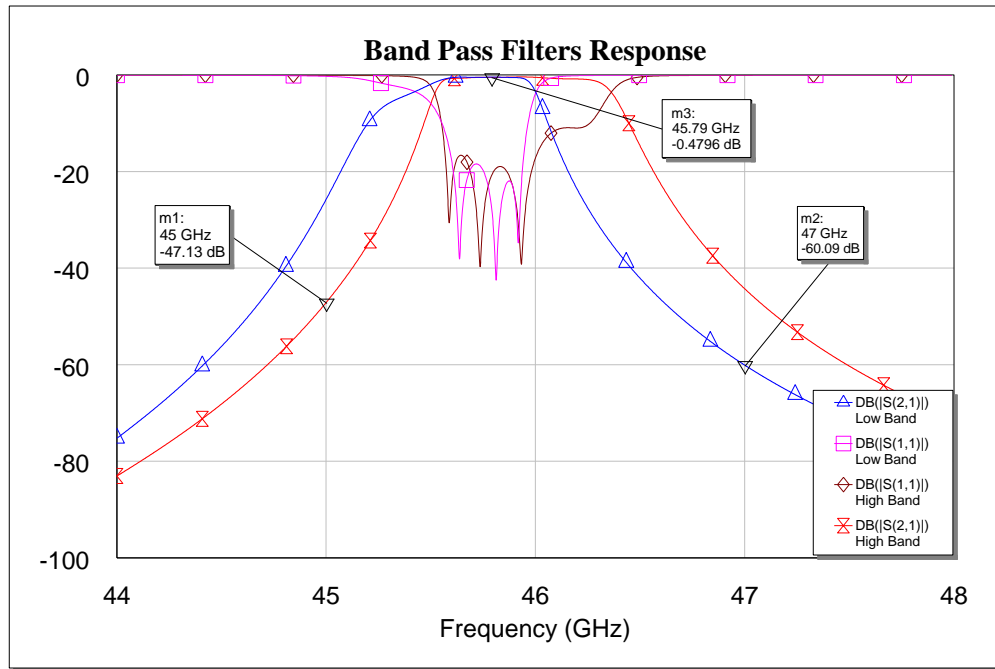


Figure 5.7-7 Waveguide band-pass filters full s-parameters response.

The Table 5.7-2 below retracts all parameters investigated in the parameterization and optimization of both low-band and high-band filters.

Name	Expression	Value	Description	Type
R	$= (H \cdot 3 - 2 \cdot L_2 - 2 \cdot L_1 - 6 \cdot w) / 2$	1.36572748204	Dimension R	Length
R1	$= .4$.4	Dimension R1	Length
w	$= 1$	1	Dimension w	Length
a3	$= 1.6190$	1.6190	Dimension a3	Length
a2	$= 1.7722$	1.7722	Dimension a2	Length
M	$= 1.94$	1.94	Dimension M	Length
b	$= 2.3872$	2.3872	Dimension b	Length
a1	$= 2.5708$	2.5708	Dimension a1	Length
L1	$= 3.5741 + (46 - F_0) \cdot 1.742e-1$	3.612424	Dimension L1	Length
a	$= 4.7752$	4.7752	Dimension a	Length
C	$= 5.8064$	5.8064	Dimension C	Length
H	$= 28.2$	28.2	Dimension H	Length
Fmin	$= 45$	45	Minimum start frequency	Frequency
F0	$= 45.78$	45.78	Center frequency	Frequency
Fmax	$= 47$	47	Maximum stop frequency	Frequency
L3	$= L1 \cdot 1.14026$	4.11910259024	Dimension L3	Length
L2	$= L1 \cdot 1.124535$	4.06229722284	Dimension L2	Length

Table 5.7-2 The parameter list of variables used in the optimization process of the waveguide filters.

Figure 5.7-8 shows the complete two-port network embedded in the test-fixture ready for connecting with the feedback oscillator. The insertion loss of a single branch is lower than 0.8 dB after the parameterization and optimization processes.

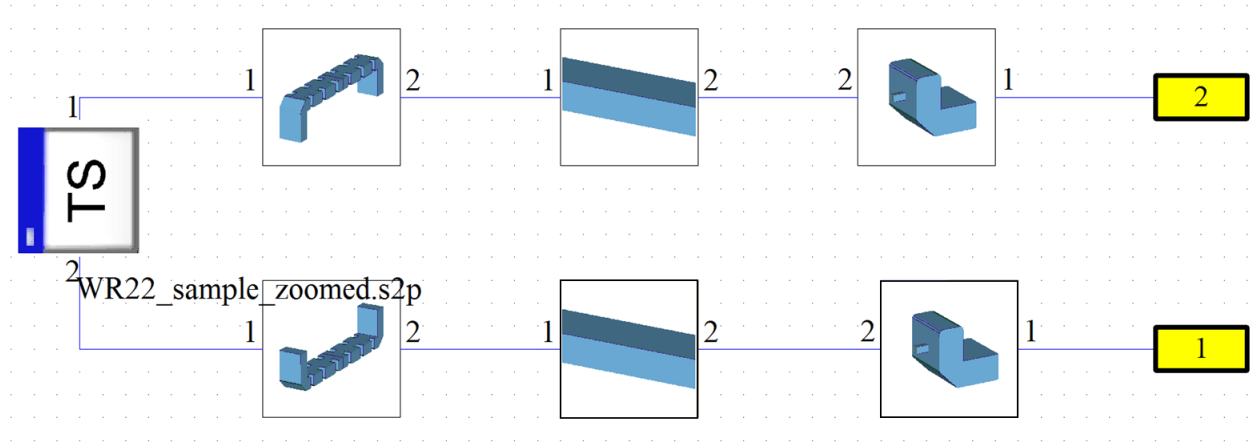


Figure 5.7-8 Complete system block diagram (resonator, waveguide filters, E-probes and transmission lines) ready for connection to the two-port version feedback oscillator.

The final assembly of the oscillator system is depicted below in Figure 5.7-9. A half part of the test-fixture is shown (top side is hidden) including the resonator and waveguide elements such as filters and E-probes as well the MMIC oscillator.

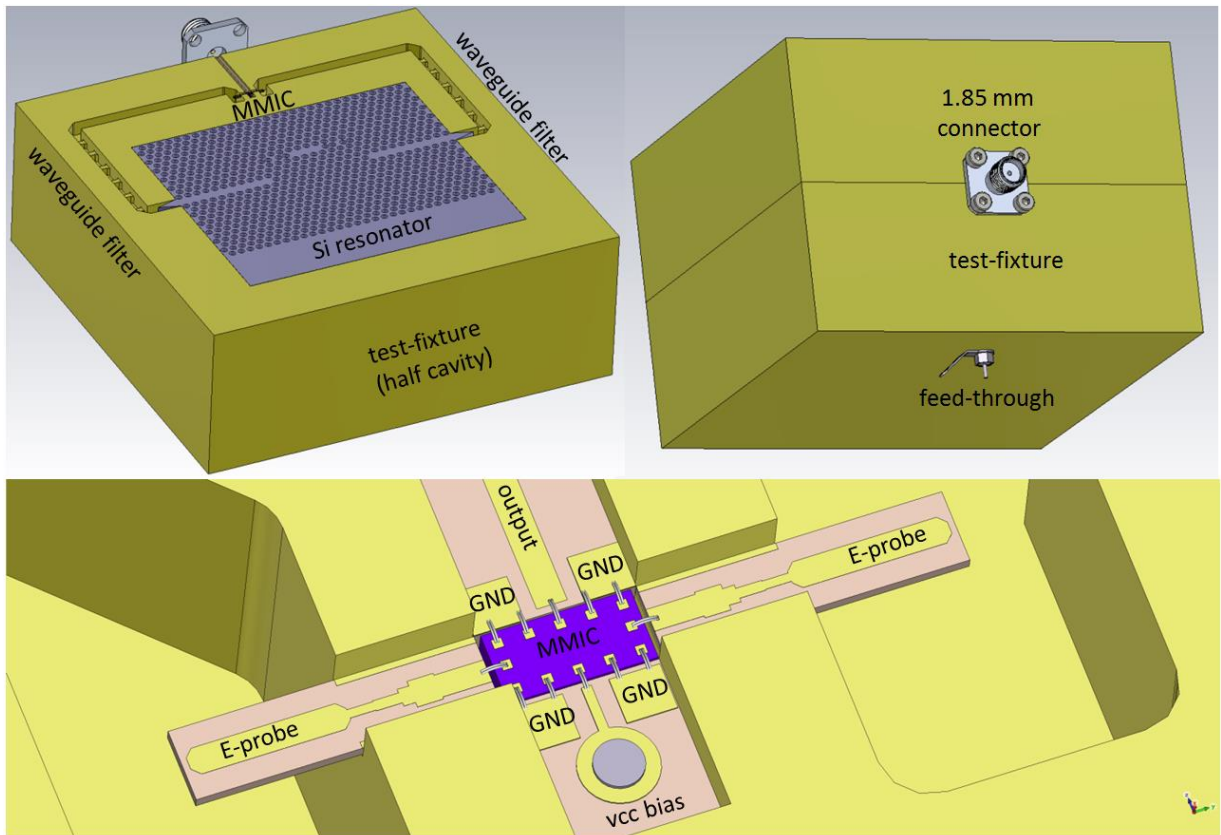


Figure 5.7-9 Final assembly of the oscillator system in the test-fixture with the respective waveguide elements (filters, E-probes, MMIC oscillator).

6. OSCILLATOR PERFORMANCE

6.1. INTRODUCTION

The oscillators performance can be assessed by obtaining plots of phase noise, output frequency and spurious. Those are the essential parameters that dictate how performant an oscillator is.

In communication systems, the more complex the modulation scheme, the more sensitive the system is to imperfections in the radio transport.

The impact of the phase noise to the available capacity, as function of constellation type and channel bandwidth [18,19] is illustrated below in Figure 6.1-1.

In high data-rate communication employed in carrier recovery systems, usually a PLL (Phase-Locked Loop) is used to track the carrier. Part of the side band noise close to carrier is attenuated and filtered out by PLL low-pass filter and usually designed with bandwidth in the order of hundreds of kilohertz. In this case, the offset range for the phase noise integration is determined from the cut-off frequency of the PLL low-pass filter up to the symbol rate in the main lobe signal.

Figure 6.1-1 shows the phase noise requirement and data rates as a function of the channel bandwidth and modulation scheme for a fixed signal-to-noise ratio. Therefore, as the capacity increases in function of modulation complexity, the more stringent are the phase noise requirements.

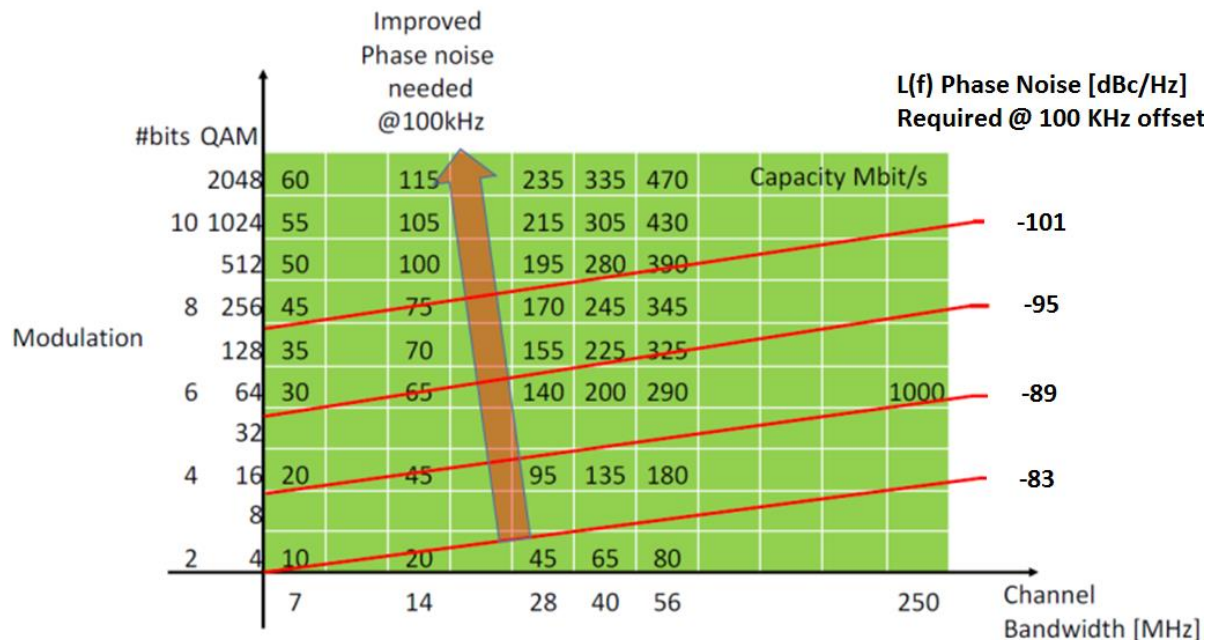


Figure 6.1-1 Phase noise requirements and data rates as functions of channel bandwidth and modulation scheme for a fixed signal-to-noise-ratio

It demonstrates the importance of the phase noise requirements for different type of modulation schemes based on constellation type (e.g. M-QAM, M-PSK) and channel bandwidth. The more dense and high order is the modulation scheme, more it is sensible to the effects of the phase noise.

6.2. PHASE NOISE PERFORMANCE

The simulated plots of single-side band (SSB) phase noise from the MMIC feedback and negative resistance type oscillators are shown in Figures 5.5-9 and 5.5-18 were obtained considering the respective layouts displayed in Figures 5.6-1 and 5.6-2. The results of phase noise are a combination of the circuit simulation using the IHP PDK elements and the EM simulation of the layout that considers the effects of coupling and loss of the substrate which as part of the design.

The SSB phase noise of the feedback and negative type oscillators are displayed below in Figure 6.2-1 and 6.2-2 respectively.

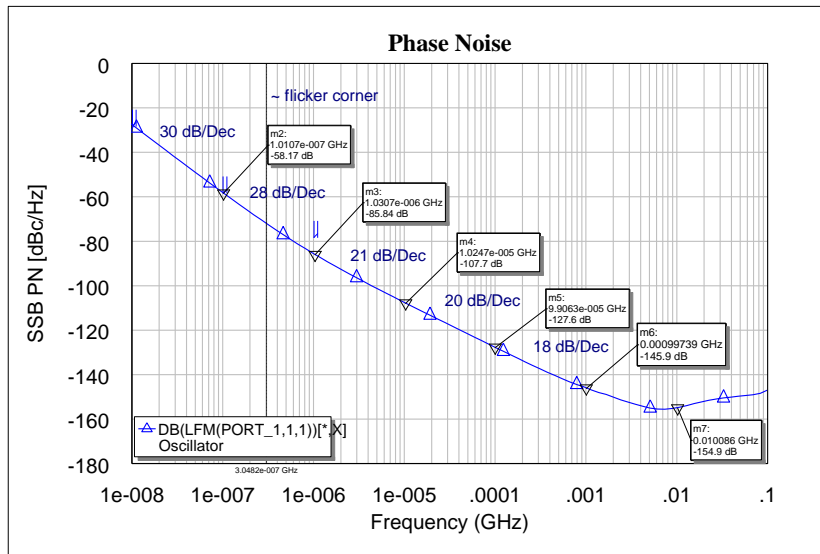


Figure 6.2-1 SSB phase noise of the feedback type oscillator

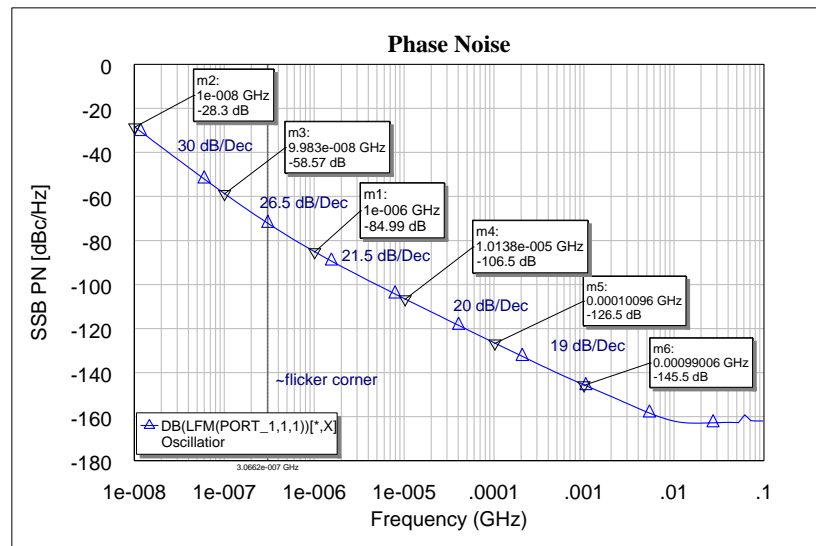


Figure 6.2-2 SSB phase noise of the negative resistance type oscillator

6.3. OUTPUT POWER PERFORMANCE

The simulated plots of output power from the MMIC feedback oscillator and negative resistance type oscillators are shown in Figures 6.3-1 and 6.3-2. The plots were also obtained considering the layouts displayed in Figure 5.6-1 and 5.6-2.

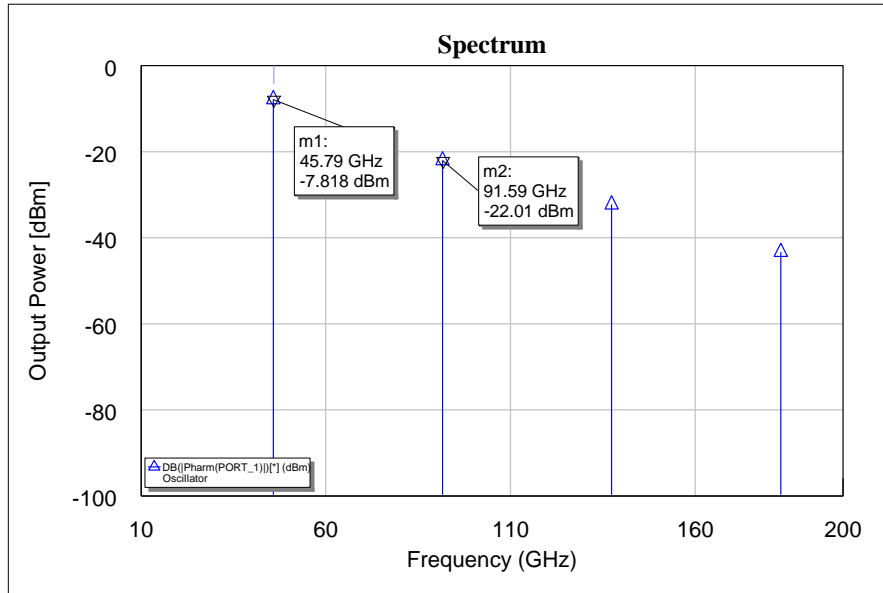


Figure 6.3-1 SSB phase noise of the feedback type oscillator

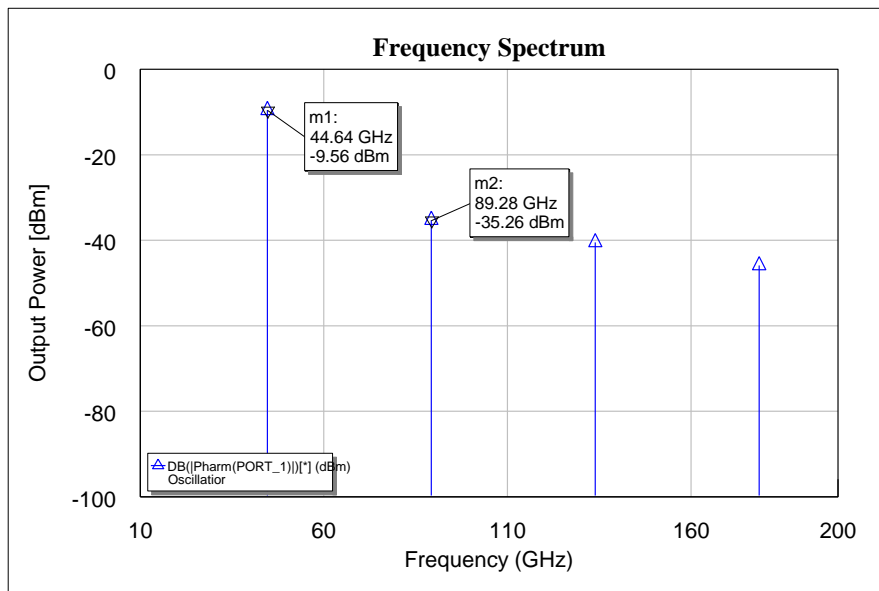


Figure 6.3-2 SSB phase noise of the negative resistance type oscillator

6.4. SPURIOUS PERFORMANCE

The spurious response is taken from the plots of output power versus frequency. Besides the feedback type oscillator has a better performance in terms of phase noise, the opposite happens with the level of harmonics with a suppression of 14 dBc (from the carrier signal). On the contrary, the oscillator based on negative resistance shows better suppression with a level of 26 dBc.

The suppression of the harmonics can be improved controlling the bias of the active devices in the circuit, however with a trade-off in phase noise. The harmonics can be further attenuated with the implementation of a low-pass filter placed at the output of the circuit or through a shunt capacitor.

7. CONCLUSIONS

7.1. ACHIEVED RESULTS

This chapter reviews the challenges, findings and limitations as well the achieved results within this work. Finally, a performance benchmark analysis of the state-of-art oscillators and the one developed within this work is presented.

The thesis focused on the investigation and characterisation of ultra-high Q-factor low loss Silicon resonators with transverse electric (TE)-like electromagnetic band-gap suitable for millimetre-wave communications such as used in low phase noise oscillator application and band pass filters.

A number of challenges within this work have been carefully faced and solved, since the engineering of high Q-factor photonic crystals in the millimetre-wave band had yet to be proven. Another challenging aspect is the fact that, being the crystal resonator intended for oscillator applications, it would need to be placed inside of a metallic cavity in order to be isolated from external disturbance sources. This could result in the resonance and coupling of high order electromagnetic propagation modes with the structure itself. However with proper adjustment in the dimensions (height) of the cavity and the introduction of absorbing coating material it had been effectively demonstrated through simulation that a combination of both factors resulted in no loss of performance for what concerns the main parameter (Q-factor) of the resonator. The results of the etching process in the resonator have also brought some concern and in fact it was one of the limitations in the work associated to the scale of the economy of the project. As the coupling within the defect cavity is determined by a small displacement between the adjacent holes, the concern was that after and due to the etching process, the holes would have its effective diameter increased, therefore disturbing the coupling and causing a significant reduction in the Q-factor of the resonator. This was confirmed comparing the results of simulated and measured structures. The last challenging aspect concerns to the reduction of the Q-factor of the network when connecting the oscillator to the resonator. A low input and/or output impedance of the oscillator circuit could load the resonator causing a reduction in the Q-factor. However, this was not an issue since the best optimized results of Q-factor were achieved with relatively poor return loss and therefore a weak coupling would be established ultimately avoiding an excessive loading the resonator structure. The proper use of a buffer stage also helped in minimizing variations when the rest of oscillator circuit was coupled to the resonator.

The dielectric material chosen for the investigation and characterisation of the resonator is a high-resistivity silicon for GHz and THz application, showing extremely low loss in the critical band of interest.

There has been, throughout this study work, a constant reference to a theoretical and analytical design approach of the resonator main structure, and where needed of the surrounding active and passive circuitry, based on an intensive and smart use of the full 3D electromagnetics tool. Parameterization and optimization were frequently used for improving target performance results such as the oscillator Q-factor and its desired oscillating frequency. Two type of resonators have been conceived and simulated, one with a single defect cavity and the other with two symmetrical defect cavities demonstrating that a higher Q-factor can be obtained.

The resonator has been manufactured using three-step deep reactive-ion etching (DRIE) low cost process especially developed for microelectromechanical systems.

The effects caused by the etching process, confirmed through a microscopic inspection, were re-introduced in the simulation environment and the correlation of results was obtained. The reverse engineering simulations showed a very good correlation of results between simulation and measured prototype, therefore confirming and validating the final electrical and physical data base of the EBG resonator through the electromagnetic simulation tool for further investigation and study, eventually using, in a near future, more accurate and more expensive manufacturing process suitable for space application.

Two oscillator circuits were proposed, designed and optimized to test the performance of the experiment employing the process design kit for MMIC design. The process used contains a complete noise modelling for the simulation of active devices, important for the evaluation of the main aspect which is the phase noise.

Special techniques employing low loss were used to connect the resonator to the MMIC oscillators in the waveguide domain under the simulation environment. A metallic cavity would suffer additional assembling impairment caused by the inclusion of the waveguide filters and E-probes necessary for connecting the resonator with the surrounding circuitry. The full S-parameters file from the measured EBG resonator and waveguide elements were used in combination with the circuit during the final circuit simulations.

Full simulations of the complete oscillator system were performed with success. The overall phase noise achieved is notable.

The overall results of this work clearly show that electromagnetic band-gap structures (EBG's) can be utilized for application in high frequency oscillators directly in fundamental mode with great benefits in obtaining ultra-high Q-factor and therefore low phase noise; and with better performance than alternative state-of-the-art technologies such as crystal oscillators in combination with frequency multiplication or frequency synthesis causing an increase in the overall phase noise by 20 log rule.

This novel technique has been successfully demonstrated and is a great contribution towards to the problem of high phase noise affecting high frequency oscillators operating at millimetre-wave band.

A benchmark of state-of-art oscillators are shown below, demonstrating the oscillator developed within this work has an excellent performance.

Benchmark

A benchmark analysis of this current study work with respect to the the state-of-the-art oscillators (commercial of-the-shelf and research papers) is reported. The oscillator developed in this work and chosen as reference for this benchmark is the feedback type.

Ref.	Process	Frequency [GHz]	Tuning [%], ppm	Pout [dBm]	PN @ 1 KHz [dBc/Hz]	PN @ 10 KHz [dBc/Hz]	PN @ 100 KHz [dBc/Hz]
RK 407 Rakon	OCXO	0.045	1.2 ppm	+6	-85*	-92*	-98*
LNO 1000 Rakon	OCVCSO SAW	1.00	3ppm	N/A	-97*	-125*	-136*

[37]	0.25 μm GaN HEMT + Al cavity	9.90	N/A	N/A	-66*	-99*	-132*
[38]	DRO (x4) + cavity	40.00	N/A	30	-104*	-127*	-134*
[39]	GaAs pHEMT + cavity	9.20	N/A	N/A	N/A	-101*	-132*
[40]	GaN 0.25 μm	7.90	0	+21	N/A	-78*	-97*
This work	SiGe HBT 0.13 μm + cavity	45.79	0	-9.5	-86	-108	-128

* Phase noise normalized to 45.79 GHz according 20 Log (N).

Table 7.1-1 Benchmark analysis of different type of oscillators

7.2. FUTURE DEVELOPMENTS

In terms of future developments, a number of aspects have been highlighted and critically discussed in the present study work with the goal of addressing improvements and further investigation to the subject of ultra-high Q-factor materials for microwave and millimeter-wave application.

Among them, the most important aspect to mention about high frequency oscillators employing silicon resonators is the frequency stability. Frequency stability by definition is the degree to which variations of carrier frequency of an oscillator deviate from the mean frequency over a specified period of time. The main factor affecting the frequency stability of an oscillator is the temperature variations. As all components involved in the electronics of the oscillator, including the resonator itself, have their characteristics that vary with the temperature, stabilization techniques would need to be addressed for a mature high frequency and low noise oscillator product.

The effect of the temperature variations in the frequency stability of the output signal from the high frequency oscillator using ultra-high Q-factor resonator was not investigated in this work. This aspect can significantly contribute to convey maturity and enable next technology readiness levels in this new category of oscillators that can become ready to compete with proven and existing technologies already established and consolidated. Therefore, a number of aspects are preliminary discussed below identifying remaining tasks and suggestions for further improvement in terms of frequency stability.

Due to the fact of the silicon resonator being located inside of a metallic cavity, and in the same manner as done in oven-controlled crystal oscillators, the cavity itself can serve and act as a oven controlled by temperature with the goal of guaranteeing a good frequency stability over time. This could be implemented by first investigating the effects of temperature variation in the resonator. Cycling of the resonator over a specific range of temperature (e.g. -40°C to $+85^{\circ}\text{C}$) in vacuum while monitoring its main parameters such as frequency stability ($\Delta f/f$) is advised. The objective is to, through a graphic of temperature versus delta frequency (Δf), the turn-over temperature point where the variation in frequency is minimum. Once the turn-over temperature is known, the cavity must be stabilized at the same temperature as the turn-over point; through heat-sink ballast transistors attached in the outside part of the metallic cavity and controlled by a thermistor that reads the temperature. This technique can really bring huge improvements and maintain control of the frequency stability. Studies conducted by J. Krupka [36] show that the permittivity and dielectric loss tangent versus temperature of high-resistivity (HiRes) silicon

materials vary only 0.15 and 3E-3 respectively, measured at 4.98 GHz over a temperature range of -40°C to +85°C. Adding an oven-controlled circuit technique in the oscillator cavity could reduce those variations to a fraction compared to a non-controlled oscillator.

Another technique to maintain good frequency stability is the stabilization of the amplitude of the oscillator by using amplitude control circuits as the voltage amplitude variations can change the output frequency. Typically, a limiter amplifier is used to reduce the oscillator amplitude jitter. The resulting increase in harmonic components caused by the limiting amplifier can be easily filter out directly with the guiding structure of the RF signal itself.

Another interesting improvement as part of the future activities could be the investigation of oscillator performance sensitivity to the process-voltage-temperature (PVT) variation of the electronic components. The variations over temperature are intrinsic to some of the transistor model parameters while the variation related to the process are strictly tied to the manufacturing tolerance in the value of each component in the circuit (i.e. the so-called yield analysis). The SG13S process design kit of IHP Microelectronics offers the possibility to work across a wide supply voltage, temperature and process parameter range. With help of Microwave Office™ software a PVT analysis can be carried out. A corner analysis can be performed to characterize the process, voltage and temperature variation impact in the design of the MMIC oscillator. In addition, a Monte Carlo simulation can also be performed in order to characterize the sensitivity of the design with respect to the components tolerance. In case the variations in the sensitivity analysis are found, it is possible to perform a yield optimization by changing the nominal value of the elements involved in the analysis.

Another relevant aspect is the improvement of the phase noise by the investigation of different categories of oscillators. It is known that configurations such as differential cross-coupled pair used in voltage-control oscillators (currently not investigated in this work) can introduce advantages in terms of phase noise by suppressing the common mode noise and ultimately provide a higher voltage excursion in the tank circuit maximizing the energy transfer into it. Second harmonic signals generated at the emitter of the transistors are significantly suppressed by a tuned filter connected to the common emitter connections. By reducing the second harmonic component, the phase noise can be improved. A low-pass filter in the output of the oscillator can also contribute for the suppression of high harmonics improving even more the overall phase noise of the oscillator.

Last, the limitation in the tuning capability of the oscillator could be carefully investigated by providing electronic tuning of the resonator in order to obtain a shift in the operating frequency. The suggested technique within this aspect could be carried out by adding two metallic plates between the internal top and bottom parts of the metallic cavity under the absorbing dielectric material (Eccosorb non-conductive) while providing a difference of potential in the plates. An electric field generated by the potential difference created between the metallic plates could in principle cause a small shift in the center frequency of the oscillator, sufficient to provide a disciplinary class of oscillators. However this technique has yet to be proven and its working principle cannot offer at the moment, without an additional specialized detailed electrical and physical design work, a degree of confidence. Tuning could also be achieved by adding parallel elements such as varactor diodes that could be controlled electronically, however at the price of the overall Q-factor of the network would be reduced and limited by the characteristics of the tuning elements such as varactor diodes.

All the techniques discussed here shall be able to empower the oscillator to a new level of technology readiness and establish a future category of oscillators.

8. ABBREVIATIONS

2D – Two Dimension

3D – Three Dimension

ABS – The absolute value of the electric or magnetic field derived from the two tangential and radial component

ADS – Advanced Design System

APSK – Amplitude and Phase Shift Keying

BiCMOS – Bipolar Junction Transistor Complementary Metal Oxide Semiconductor

BJT – Bipolar Junction Transistor

Cr – Chromium

CMOS – Complementary Metal Oxide Semiconductor

D – Electric Displacement Field

dB – Decibel

dBc – Decibels relative to the carrier

dBm – Decibels relative to one milliwatt

DC – Direct Current

DRC – Design Rule Check

DRO – Dielectric Resonator Oscillator

DRIE – Deep Reactive-Ion Etching

DVB-S2X – Extension of the Digital Video Broadcasting 2nd Generation

E – Electric Field

ESA – European Space Agency

EBG – Electronic Band-Gap

EIA – Electronic Industries Alliance

EM – Electro-Magnetic

FBZ – First Brillouin Zone

FOM – Figure of Merit

GDS – Graphic Database System

H – Magnetic Field

HB – Harmonic Balance

HBT – Hybrid Bipolar Transistor

HiCUM – High Current Model

HR – High Resistivity

IBZ – Irreducible Brillouin Zone

IEEE – Institute of Electrical and Electronics Engineers

k – Wave-Vector

Ka-band – Portion of the microwave part of the electromagnetic spectrum defined as frequencies ranging from 26.5 to 40 GHz

LVS – Layout Versus Schematic

MAG – Maximum Available Gain

Mbps – Mega-bits per second

MEMS – Micro-Electro-Mechanical Systems

MIM – Metal-Insulator-Metal

MMIC – Monolithic Microwave Integrated Circuit

MODCOD – Modulation and Coding

MWO – Microwave Office

N/A – Not Available

NQS – Non-Quasi-Static

O – Oxygen

P1dB – One dB Compression Point

PC – Photonic Crystal

PDK – Process Design Kit

PGB – Photonic Band-Gap

PLL – Phase Locked Loop

PSK – Phase Shift Keying

PVT – Process-Voltage-Temperature

PWE – Plane Wave Expansion

Q – Quality-factor

QAM – Quadrature Amplitude Modulation

Q-band – Portion of the microwave part of the electromagnetic spectrum defined as frequencies ranging from 33 to 50 GHz

RF – Radio Frequency

Si – Silicon

SiGe – Silicon-Germanium

SNR – Signal-to-Noise Ratio

SSB – Single Side Band

TE – Transversal Electric

TEM – Transversal Electromagnetic

TIR – Total Internal Reflection

TRL – Thru, Reflect, Line calibration process

TSV – Through-Silicon Via-Holes

UPNA – Public University of Navarre

V-band – Portion of the microwave part of the electromagnetic spectrum defined as frequencies ranging from 40 to 75 GHz

VNA – Vector Network Analyser

WR – Waveguide Rectangular

9. REFERENCES

- [1] - J. Dai, J. Zhang, W. Zhang, and D. Grischkowsky, "Terahertz time-domain spectroscopy characterization of the far-infrared absorption and index of refraction of high-resistivity, float-zone silicon", J. Opt. Soc. Am. B 21, 1379, 2004.
- [2] - Europe 2020 Flagship Initiation, Innovative Union, SEC (2010) 1161, European Commission [online], retrieved 21st Feb 2011.
- [3] - J. Krupka, P. Kaminski, R. Kozłowski, B. Surma, A. Dierlamm, M. Kwęstarcz, "Dielectric Properties of semi-insulating silicon at microwave frequencies", Applied Physics Letter 107, 082105, August 2015.
- [4] - J. Krupka, J. Breeze, N. A. Centeno, N. Alford, L. Jensen and T. Claussen, "Measurements of Permittivity and Dielectric Loss Tangent of High Resistivity Float Zone Silicon at Microwave Frequencies", IEEE Transactions on Microwave Theory and Techniques, Vol 54, No. 11, November 2006.
- [5] - K. R. Williams, K. Gupta and M. Wasilik, "Etch rates for micromachining processing-Part II", Journal of Microelectromechanical Systems, vol. 12, no. 6, pp. 761-778, December 2003.
- [6] - J. W. Lamb, "Miscellaneous data on materials for millimetre and submillimetre optics", International Journal of Infrared and Millimeter Waves, December 1996.
- [7] - W. J. Otter, S. M. Hanham, N. M. Ridler, G. Marino, N. Klein, S. Lucyszyn, "100 GHz ultra-high Q-factor photonic crystal resonators", Sensors and Actuators A; Physical, Elsevier, July 2014.
- [8] - Y. Akahane, T. Asano, B.-S. Song & S. Noda, "High-Q photonic nanocavity in a two-dimensional photonic crystal", Nature, Vol. 425, October 2003.
- [9] - Leeson, D. B., "A Simple Model of Feedback Oscillator Noise Spectrum", Proceedings of the IEEE, 54 (2): pages 329-330, February 1966.
- [10] - A. Wagemans, P. Ballus, R. Dekker, A. Hoogstraate, H. Maas, A. Tombeur, et al., "A 3.5 mW 2.5 GHz diversity receiver and a 1.2 mW 3.6 GHz VCO in silicon-on-anything", IEEE Int. Solid-State Circuits Conf. Tech. Dig., pp. 250-251, December 1988.
- [11] - E. Hegazi, J. Rael, A. Abidi, "The Designer's Guide to High-Purity Oscillators", Kluwer Academic Publishers, August 2004.
- [12] - B. El-Karesh, L. N. Hutter, "Silicon Analog Components: Device Design, Process Integration, Characterisation and Reliability", Springer, 2015.
- [13] - M. Schroter and A. Chacravorty "A Geometry Scalable Physics-Based Compact Bipolar Transistor Model", Documentation of model level 2 v2.2, University of California, San Diego, November 2005.
- [14] - J. G. Tartarin, G. Soubercaze-Pun, L. Bary, C. Chambon, S. Gribaldo, O. Llopis et al., "Low Frequency and linear high frequency noise performances of AlGaIn/GaN grown on SiC substrate", AIP Conference Proceedings 780, August 2005.

- [15] - F. Sischka, “*Modelling Tool Kits – 1/f Noise Modelling for Semiconductors*”, NoiseDoc, April 2002.
- [16] - J. Everard, “*Fundamentals of RF Circuit Design with Low Noise Oscillators*”, Wiley-Blackwell, October 2002.
- [17] - L. Jensen, “*High Resistivity (HiRes™) Silicon for GHz & THz Technology*”, Application Notes, version 1.1, TopSil company, January 2014.
- [18] - M. Hörberg, “*Optimum GaN HEMT Oscillator Design Targeting Low Phase Noise*”, Thesis for the degree of licentiate of Engineering, Chalmers University of Technology, Gothenburg, Sweden, April 2005.
- [19] - T. Eriksson, “*Private conversation of phase noise limitations of the data capacity*”, Chalmers University of Technology, Gothenburg, Sweden, 2015.
- [20] - J. D. Joannopoulos, S. G. Johnson, “*Photonic Crystals : Modelling the Flow of Light*”, Princeton University Press, Princeton, NJ, 2008.
- [21] - Q. Gong, X. Hu, “*Photonic Crystals: Principles and Applications*”, Pan Stanford Publishing, February 2014.
- [22] - J.-M. Lourtioz, H. Benisty, V. Berger, J.-M. Gerard, D. Maystre, A. Tchebnokov, “*Photonic Crystals*”, Springer, 2006.
- [23] - S. Prorok, “*Nanophotonics and Integrated Optics, Photonic Crystal Cavities*”, Whitepaper, CST AG, 2013.
- [24] - J. Proakis, M. Salehi, “*Digital Communication*”, 5th edition, November 2007.
- [25] - P. H. Bolivar et al., “*Measurement of the Dielectric Constant and Loss Tangent of High Dielectric-Constant Materials at Terahertz Frequencies*”, IEEE Transactions on Microwave Theory and Techniques, Vol. 51, No. 4, April 2003.
- [26] - B. Razavi, “*Analysis, modelling and simulation of phase noise in monolithic voltage-controlled oscillators*”, Proc. IEEE Custom Integrated Circuits Conference, May 1995.
- [27] - A. Demir, A. Mehrotra, and J. Roychowdhury, “*Phase noise in oscillators: a unifying theory and numerical methods for characterization*”, IEEE Trans. Circuits Syst. I, vol. 47, no. 5, pp. 55 – 674, May 2000.
- [28] - A. Hajimiri, T. H. Lee, “*A general theory of phase noise in electrical oscillators*”, IEEE J. Solid-State Circuits, vol. 33, no. 2, pp. 179-194, February 1998.
- [29] - T. Sato, K. Okada, A. Matsuzawa, “*A New Figure of Merit of LC Oscillators Considering Frequency Tuning Range*”, IEEE International Conference on ASIC, October 2011.
- [30] - Er. K.K. Sharma, “*Fundamental of Microwave and Radar Engineering*”, S. Chand and Company Ltd., 2011.
- [31] - A. Pawlak et al., “*SiGe HBT modelling for mm-wave circuit design*”, IEEE Bipolar /BiCMOS Circuits and Technology Meeting – BCTM, October 2015.

- [32] - A. Pawlak, M. Schröter, J. Krause, D. Céli and N. Derrier, “*HICUM/2 v2.3 Parameter Extraction for Advanced SiGe-Heterojunction Bi-polar Transistors*”, Proc IEEE BCTM, pp. 195-198, 2011.
- [33] - M. Schroter and A. Chacravorty, “*Advanced compact bipolar transistor models - HICUM*”, Silicon heterostructure Handbook, J. Cressler, CRC Press NY, 2005.
- [34] - J. Dobrowolski, “*Introduction to Computer Methods for Microwave Circuit Analysis and Design*”, Artech House, 1991.
- [35] - V. Rizzoli, E. Mastri, D. Massoti, “*General noise analysis of nonlinear circuits by the piecewise harmonic-balance technique*”, IEEE Trans. MTT, May 1994, pp 807-819.
- [36] - J. Krupka, “*Resistivity and Surface Resistance Measurements of Semiconductors and Conductors*”, EMINDA Project and EMMA-club meeting, Warsaw, December 2012.
- [37] - M. Hörberg et al., “*Phase-Noise Analysis of an X-Band Ultra-Low Phase-Noise GaN HEMT Based Cavity Oscillator*”, IEEE Transactions on Microwave Theory and Techniques, Vol. 63, N.8, August 2015.
- [38] - A. Hati, “*High Spectral Purity Oscillator at 40 GHz: Design Using Air-Dielectric Cavity*”, Frequency Control Symposium (FCS), 2010 IEEE International, June 2010.
- [39] - J. Maree, J. B. de Swardt, and P. W. van der Walt, “*Low phase noise cylindrical cavity oscillator*”, IEEE AFRICON, pp. 1–5, 2013.
- [40] – H. Liu et al., “*Design of Ultra-Low Phase Noise and High Power Integrated Oscillator in 0.25 μ m GaN-on-SiC HEMT Technology*”, IEEE Microwave and Wireless Components Letters, Vol. 24, N.2, February 2014.